



**University of
Nottingham**

UK | CHINA | MALAYSIA

Smart window photovoltaic concentrator for energy generation and solar control

Submitted to the University of Nottingham for the degree of Doctor of
Philosophy.

Manlio Salas Castillo
Student ID 4164415

School of Engineering
University of Nottingham

Nottingham, United Kingdom September 2019

Abstract

Central to the global mission on reducing societies carbon footprint is the commitment of governments and international institutions to set energy reduction targets. In this regard, buildings are responsible for large energy loads. Due to the necessity to create thermal and visual comfort, vast energy is consumed to satisfy internal cooling, heating, and lighting loads. The two main strategies to reduce buildings energy consumption are renewable energy technologies and energy efficient building planning. Building Integrated PV systems (BIPV) are devices capable to generate electricity while replacing building materials and reduce electricity costs, protect the building from weather acting as a building envelope and offering aesthetically pleasing features to the building. Windows play key role in the building energy consumption allowing for sunlight and heat to enter the building. Some commercial technologies offer solar control functions using reversible photochromic, thermochromic or electrochromic mechanisms. However, only few offer an automated system able to respond to dynamic changes of the environment while producing onsite energy.

The research presented in this thesis covers the details of the design and development of a novel lightweight solar concentrator for “smart window” applications. The smart window design was conceived to automatically control the solar radiation entering buildings and generate clean electricity at the same time, thus compensating artificial lighting, cooling, and heating loads.

To achieve the dual functionality of the smart window two novel thermotropic membranes were developed and characterised using two gelling agents and 3 polymers. Transmittance levels of 95% in clear state and 40% when in light scattering state were achieved. A ray tracing model was validated against experimental indoor tests with 8% deviation. Indoor tests comparing between 2% wt. HPC & 1.5 % wt. GGF and 6% wt. HPC & 1.5 % wt. GGF membranes reported efficiency values of 3.7% and 5.1% and MPP values of 0.018W and 0.024W, respectively. Outdoor tests showed that the automated solar control function allows sunlight to pass through the smart window during the morning and the evening hours but block the sun when irradiation levels

surpass 600 W/m². The study concludes, however, that in order to produce a more efficient device the membrane reflectivity of the smart window should be close to 90%.

Acknowledgements

To my beloved family for the unconditional support across these years away from home. To my parents Eduardo and Flor for gave me the opportunity to accomplish another goal in life. To my son Lucas, my daughter Constanza and my love Yazmin for fuelling my dreams, to Eduardo and Cynthia my brothers for always supporting me.

I would like to express my infinite gratitude to Yupeng Wu my supervisor who taught me countless things from research to real life and proven me that everlasting patience exists. I found more than a supervisor in him, a friend a brother someone to feel protected and having this in life is just a blessing. A special mention to Xiao Liu, brother without your help this would not have been possible god bless you now and forever. Lastly but not least, an honour mention to my brother Jan thanks for everything! may the success and joy follow you the rest of your days, I can't extend anymore my gratitude for your help.

Also, I want to express my gratitude to Professor Hao Liu and Dr. Robin Wilson who help me a lot through this Ph.D. years always with their wise advice and Dr. Karen Connelly for helping me to start in the best possible way.

To all my research group friends each of you did something to help me finishing this work, you know who you are.

An especial mention to CONACYT to fund me to accomplish this through the Beca al Extranjero 2015 del estado de Durango.

Contents

Abstract.....	i
Acknowledgements.....	ii
Contents	iii
List of tables	vii
List of figures	viii
Nomenclature	xiv
Abbreviations	xv
Chapter 1 Introduction	
1.1 Building scenario.....	1
1.2 Problem statement and research motivation.....	3
1.3 Aim of the thesis.....	4
1.4 Objectives of the thesis.....	4
1.5 Thesis structure.....	5
Chapter 2 Literature review	
2.1 Building Integrated PV technologies.....	8
2.1.2 PV window simulation.....	13
2.1.3 Solar thermal PV windows	18
2.1.4. PV technology summary.....	20
2.2.1 Building Integrated Concentrated PV Window Systems.....	22
2.2.2 Parabolic concentrator technologies on windows.....	23

2.2.3 Luminescent solar concentrators.....	27
2.2.4 Building integrated PV concentrators summary.....	31
2.3.1 Smart windows.....	33
2.3.2 Thermotropic materials.....	33
2.3.3. Hydrogels.....	33
2.3.4 Relevant thermo-responsive materials.....	34
2.3.5 smart windows with thermotropic technologies.....	35
2.3.6 Smart window summary.....	41
2.4 Summary.....	42
 Chapter 3 Materials and methods	
3.1 Building Integrated Concentrating PV (BICPV) “smart window”	44
3.1.1 Material selection.....	46
3.2 Sample preparation and characterisation.....	48
3.3 Samples characterisation.....	48
3.3.1 Micro DSC Test.....	49
3.3.2 FTIRs test.....	51
3.3.3 Environmental electron scanning microscopy.....	53
3.3.4 Long lasting prototype window test.....	54
3.3.5 UV-VIS spectroscopy.....	55
3.4 Lab instruments and experimental settings characterisation.....	57
3.5 Smart window design and characterisation.....	62
3.5.1 Single PV cell characterisation.....	62

3.5.2. Smart window characterization.....	63
3.5.3. Smart window with reflective layer attached.....	64
3.6 Ray tracing modelling approach.....	65
3.6.1 Model description.....	65
3.7 smart window prototype indoor test settings.....	67
3.8 Outdoor experimental settings.....	68
3.9 Outdoor smart window prototype.....	70
3.10 Summary.....	71
 Chapter 4 Design and development of thermotropic membrane for novel smart window	
4.1 Characterisations of liquid and membrane samples.....	73
4.2 Differential scanning calorimetry test	74
4.3 FTIRs on liquid and membrane sample	77
4.4 ESEM in membrane samples	80
4.5 Smart window prototype long-lasting membrane test	81
4.6 UV-VIS spectroscopy.....	82
4.7 Conclusions.....	92
 Chapter 5 Indoor optical, electrical, and thermal characterization of smart window	
Prototype	
5.1 Single cell characterisation.....	95
5.2- Smart window concentration concept.....	98
5.2.1 Ray tracing modelling validation.....	100
5.2.2 Smart window optical performance modelling.....	101

5.3 Smart window prototypes with thermotropic membrane.....	102
5.3.1 2% wt. HPC & 1.5 % wt. GGF membrane.....	102
5.3.2 6% wt. HPC & 1.5 % wt. GGF membrane.....	107
5.4 Discussion.....	111
5.5 Conclusions.....	112
Chapter 6 Design, fabrication, and outdoor testing of smart window prototype for electricity generation and daylight control	
6.1 Smart window outdoor testing.....	114
6.2 Smart window with membrane vs reference window at 30° inclination.....	115
6.3 Smart window with membrane vs reference window at 60° inclination.....	118
6.4 Smart window with membrane vs reference window at 90° inclination.....	122
6.5 Discussion.....	125
6.6 Indoor vs outdoor.....	126
6.7 Summary.....	126
Chapter 7 Conclusions and further work	
7.1 Develop and thermal and optical characterisation of the membrane.....	128
7.2 Indoor characterisation of the smart window.....	130
7.3 Outdoor characterisation of the smart window.....	131
7.5 Further work.....	132
Appendix A.....	134

List of tables

Table 2.1. Depicts Si (amorphous and wafer), thin films (CuInGaS ₂ and CdTe), polymer and DSSC cells integrated into a building as a façade, window, and roof.....	12
Table. 2.2 Summary of relevant simulations performed on STPV featuring characteristics of STPV as WWR transmittance, efficiency and software used.....	16
Table 2.3. Summary of materials, applications, technologies, and benefits of BIPV.....	21
Table 2.4. CPV window relevant work summary.....	26
Table 2.5. Presents a summary of commercial dye characteristics.....	29
Table 2.6. Summary of relevant researches in CPV and LSC window integrated.....	32
Table 2.7. Highlights of smart window technologies and main features.....	42
Table 3.1 Polymer structure and features.....	47
Table 3.2 DSC test samples concentrations.....	51
Table 3.3 FTIRs test samples concentrations	53
Table 3.4 ESEM pictures membrane concentrations	54
Table 3.5. Long lasting test sample concentrations	54
Table 3.6. Temperature range for the selected polymers	55
Table 3.7. 7 Selected concentrations for liquid UV-VIS samples concentrations	57
Table 3.8. Selected concentrations for gelling agent comparison	57
Table 3.9 Calculated average values for the experimental rig plate	60
Table 3.10 Calculated average values for a smart window area.....	61
Table 3.11 Cosine corrector versus pyranometer.....	62
Table 4.1. Classification of IR bands according to ISO 20473 standard, which specifies the division of optical radiation into spectral bands.....	80

Table 5.1. Single PV cell characterisation.....	96
Table 5.2. Smart window electrical values comparison at 400 W/m ²	111
Table 5.3 Smart window electrical values comparison at 700 W/m ²	112

List of figures

Figure 2.1 PV technologies suitable for window integration. Wafers c-Si, GaAs, III-V and thin films	9
Figure 2.2. Different PV shading devices, (a) with a more aesthetical approach and (b) with louvers design	17
Figure 2.3. (a) Components comprising a stationary PV/T and (b) Schematic design of a parabolic trough collector with tracking system.....	18
Figure 2.4. Depiction of the hybrid solar window and full PV/T system.....	20
Figure 2.5. (a) The revolved CPC. (b) The Crossed CPC. (c) The Compound CPC. (d) The Lens-Walled CPC. (e) V-trough. (f) CPC. (g) Compound Hyperbolic Concentrator. (h) 3D square aperture V-trough. (i) Polygonal aperture CPC. (j) Hyperboloid with an elliptical entry aperture and square exit aperture.....	23
Figure 2.6. The LSC dye absorbs incoming light (E1) then luminescence is randomly emitted (E2). Light re-emitted light reaching the collector surface within the escape cone are lost, the rest are guided to the edges by total internal reflection.....	27
Figure 2.7. Three LSC samples of 5 cm × 5 cm × 0.5 cm size; Dye C LSC with 0.01 weight (wt.) % concentration, Dye B with 0.05 wt. % concentration, Dye A with 0.05 wt. % concentration representing blue, green and red colour respectively under UV light	27
Figure 2.8. The range of photoluminescence (PL) emission colour with size for CdSe QD from small to large, blue to red respectively, using a near-ultraviolet lamp with QD size from ~1 nm to ~10 nm	30
Figure 2.9. (a) light scattering state for electricity generation (b) transparent state for indoor passive heating	36
Figure 2.10. Smart window prototype with 0.5 mm silicon spacer, low iron glass and HPC membrane below the Ts (left) and above the Ts (right) showing clear and light scattering states respectively.....	37

Figure 3.1 Total internal reflection concept.....	45
Figure 3.2 BICPV working principle (a) Translucent state, (b) Clear State	45
Figure 3.3 DSC components and data collection flow	49
Figure 3.4. ΔH , T_m , T_s and T_L describe under the DSC endotherm curve.....	50
Figure 3. 5 FTIRs components diagram	52
Figure 3.6 ESEM components.....	53
Figure 3.7 (a) Illustrating the positions of the thermocouples at the window sample, (b) smart window prototype in clear state at room temperature at the hot plate (c) smart window prototype in light scattering state	56
Figure 3.8 Experimental rig for indoor testing.....	58
Figure 3.9 Uniformity of light source grid.....	59
Figure 3.10 Light distribution contour maps, (a) low irradiation 170 W/ m^2 , (b) mid irradiation 400 W/ m^2 , (c) high irradiation 700 W/ m^2	60
Figure 3.11 Smart window area contour maps. (a) low irradiation 170 W/ m^2 , mid irradiation 400 W/ m^2 , (c) high irradiation 700 W/ m^2	61
Figure 3.12 PV single cell indoor characterisation.....	62
Figure 3.13 Saturn PV cell ready to be attached to the smart window	63
Figure 3.14 Smart window prototype ready to be indoor characterised	64
Figure 3.15 Smart window prototype settings on the experimental rig.....	64
Figure 3.16 Ray tracing model design (a) and (b) light rays tracked by the simulation	66
Figure 3.17. Thermocouple distribution and cosine corrector positioning on the back the smart window prototype	67
Figure 3.18. Experimental board components and settings	68

Figure 3.19. Experimental board thermocouples locations diagram	69
Figure 3. 20 Experimental board at three different angles positions for outdoor testing	70
Figure 3.21. The Experimental board (a) smart window at clear state (b) at light scattering state	71
Figure 4.1 Liquid HPC 2 wt. % and HPC 6 wt. % micro-DSC test	75
Figure 4.2 HPC & GGF membranes micro DSC test	76
Figure 4.3 HPC & ethulose membranes micro-DSC test... ..	76
Figure 4.4 HPC & 6 wt. % GGF 1.5 wt. % VS. HPC & 6 wt. % ethulose 1.5 wt. %. Micro DSC test.	77
Figure 4.5 FTIR spectroscopy on 6 wt.% HPC and distilled water sample	78
Figure 4.6 FTIR spectroscopy of HPC 6 wt.% GGF 1.5 wt. % in green against HPC 6% ethulose 1.5 wt. % in pink	79
Figure 4.7 ESEM membranes photos (a)HPC & GGF membrane, (b) HPMC & GGF membrane, (c) PNIPAM & GGF membrane and (d) HPC & ethulose	81
Figure 4.8 Room temperature long lasting test of the smart window prototypes	82
Figure 4.9 Transmittance on HPC liquid samples	83
Figure 4.10 10 Transmittance on HPMC liquid samples	84
Figure 4.11. Transmittance on PNIPAM liquid samples	84
Figure 4.12. HPC and GGF membrane transmittance test	85
Figure 4.13 HPMC and GGF membrane transmittance test	86
Figure 4.14 PNIPAM and GGF membrane transmittance test	87
Figure 4.15 Ethulose and HPC membranes transmittance test	88
Figure 4.16 HPC & GGF membranes reflectance test	89

Figure 4.17. HPMC & GGF membranes reflectance test	89
Figure 4.18. PNIPAM & GGF membranes reflectance test	90
Figure 4.19. Ethulose and HPC membranes reflectance test.....	91
Figure 4.20. Comparison of HPC & GGF membrane against HPC & Ethulose membrane	92
Figure 5. PV cells I-V curve measurements	96
Figure 5.2 Low, mid, and high irradiance comparison	97
Figure 5.3 Temperature profile test on I-V curves at 700 W/m ²	97
Figure 5.4 Efficiency variation from 28 °C to 40 °C at 700 W/m ²	98
Figure 5.5 Fill factor from 28 °C to 40 °C at 700 W/m ²	98
Figure 5.6 Smart window VS. Single cell I-V curves at 700 w/m ²	99
Figure 5.7 Irradiance maps for absorbed flux	100
Figure 5.8 Predicted optical performance of the smart window	102
Figure 5.9 Smart window temperature profile using the 2% wt. HPC & 1.5 % wt. GGF membrane under 400 W/m ²	103
Figure 5.10 Smart window power curves using the 2% wt. HPC & 1.5 % wt. GGF membrane under 400 W/m ²	103
Figure 5.11 Light transmittance versus power output on smart window using the 2% wt. HPC & 1.5 % wt. GGF membrane under 400 W/m ²	104
Figure 5.12 Smart window prototype I-V curves using the 2% wt. HPC & 1.5 % wt. GGF membrane under 700 W/m ²	105
Figure 5.13 Smart window prototype Power curves using the 2% wt. HPC & 1.5 % wt. GGF membrane under 700 W/m ²	105
Figure 5. 14 Light transmittance versus power output on smart window prototype using the 2% wt. HPC & 1.5 % wt. GGF membrane under 700 W/m ²	105

Figure 5.15 5.15 Smart window prototype temperature profiles at 2% wt. HPC & 1.5 % wt. GGF under 400 W/m ²	106
Figure 5.16 I-V curves Smart window prototype with 6% wt. HPC & 1.5 % wt. GGF membrane under 400 W/m ²	107
Figure 5.17 Power curves Smart window prototype with 6% wt. HPC & 1.5 % wt. GGF membrane under 400 W/m ²	108
Figure 5.18 Light transmittance versus power output on smart window prototype using the 6% wt. HPC & 1.5 % wt. GGF membrane under 400 W/m ²	108
Figure 5.19 I-V curves Smart window prototype with 6% wt. HPC & 1.5 % wt. GGF membrane under 700 W/m ²	109
Figure 5.20 Power curves Smart window prototype with 6% wt. HPC & 1.5 % wt. GGF membrane under 700 W/m ²	109
Figure 5.21 Light transmittance versus power output on smart window prototype using the 6% wt. HPC & 1.5 % wt. GGF membrane under 700 W/m ²	110
Figure 5.22 Smart window prototype temperature profiles at 2% wt. HPC & 1.5 % wt. GGF under 400 W/m ²	111
Figure 6.1 Irradiance levels on experimental board pyranometers at 30°	116
Figure 6.2. Temperature profile for smart window and reference window glass covers and ambient temperature.....	116
Figure 6.3 Temperature vs. efficiency of experimental board components at 30°	117
Figure 6.4. Power output distribution across the irradiance levels at 30°	118
Figure 6.5. Irradiance levels on experimental board pyranometers at 60°	119
Figure 6.6 Temperature profile of experimental board components at 60°	120
Figure 6.7. Temperature vs. efficiency of experimental board components at 60°	121

Figure 6.8. Power output distribution across the irradiance levels at 60°122

Figure 6.9. Irradiance levels on experimental board pyranometers at 90°123

Figure 6.10. Temperature profile of experimental board components at 90°123

Figure 6.11. Temperature vs. efficiency of experimental board components at 90°124

Figure 6.12. Power output distribution across the irradiance levels at 90°125

Nomenclature

A	Collector aperture area
C	Specific heat capacity of the coolant
G	Incident solar irradiance
J_{sc}	Short circuit current
I_{mpp}	Electric current at maximum power operation
\dot{m}	mass flow rate
η_t	Thermal efficiency
η_e	Electrical efficiency
Θ_c	Nominal half acceptance angle
<i>MPP</i> or P_{max}	Maximum power point
T_{in}	Coolant temperature inlet
T_{out}	Coolant temperature outlet
V_{mpp}	Voltage at maximum power operation
V_{oc}	Open circuit voltage
n_1	Refractive index of the air
n_2	Refractive index of the glazing cover
ΔH	Enthalpy
T_m	Maximum heat capacity
T_S	Lower transition boundary
T_L	Upper transition boundary
C_e	Effective concentration ratio
C_g	Geometric concentration ratio
η_o	Optical efficiency
I	Absorbed flux in the selected surface
η	PV cell efficiency
A_{pv}	PV cell area

Abbreviations

BIPV Building Integrated photovoltaic

c-Si Crystalline silicon

DSSC Dye-sensitized solar cells

QD Quantum dots

STPV Semi-transparent photovoltaic

SHGC Solar heat gain coefficient

WWR Window to wall ratio

A:Si Amorphous silicon

HVAC Heating ventilation air condition

MIPVW Multifunctional integrated photovoltaic window

MPPT Maximum power point tracking

PV/T PV and thermal collector

CPV Concentrated Photovoltaic

CPC.... Compound Parabolic Concentrators

RACPC Rotationally Asymmetrical Compound Parabolic Concentrator

DIACPC Dielectric compound parabolic concentrator

PMMA Poly(methyl-methacrylate)

R^2 Square root

MBE Mean bias error

RMSE Root mean square error

RADTIRC Rotationally asymmetrical dielectric totally internally reflecting concentrator

PRIDE Photovoltaic Facades of Reduced Costs Incorporating Devices with Optically Concentrating Elements

LSC Luminescent solar concentrators

TIR Total internal reflection

LQE Luminescence quantum efficiency

OLED Organic light emission diode

ESS Energy Storage Smart Window

LCD Liquid crystal display

Si-TFSC Si thin-film solar cell

TMPD Tetramethyl-*p*-phenylenediamine

DC Direct current

AC Alternating current

BK7 Borosilicate glass Schott

HPC Hydroxypropyl cellulose

PNIPAM Poly(N-isopropylacrylamide)

HPMC Hydroxypropyl methyl cellulose

GGF Gellan gum type F

DSC Micro differential scanning calorimetry

ESEM environmental electron scanning microscopy

Pr Pyranometer reference window

Ps Pyranometer smart window

Pt Pyranometer on top of the board

Ts Smart window front cover temperature

Tr Reference window front cover temperature

Tb Board ambient temperature

Rw Reference window

Sw Smart window

η_{PVs} Smart window PV cell efficiency

η_{PVr} Reference window PV cell efficiency

TPVs Smart window PV cell temperature

TPVr Reference window PV cell temperature

Chapter 1

Introduction

1.1 Building scenario

In recent years, the search for innovative ways to improve energy consumption is becoming increasingly urgent. In countries such as the U.S. and China buildings currently account for over 41% and 28% of total energy consumption respectively Xia, Hong [1]. Energy usage in buildings is largely required for creating a thermally and visually comfortable environment for building occupants through the use of ventilation, heating, cooling and artificial lighting services which are typically responsible for over 70% of total energy demand in buildings [2, 3]. Additional factors like climate change, population growth and the increase in additional amenities building services can be taken into account to reach these new high levels of energy consumption. Predictions of recent studies indicate that this trend will continue rising in the near future [4, 5]. Even though building emission have reached in 2018 an all-time high of 3060 million tonnes of equivalent oil volume , and indirect building emissions represented 28% of global CO2 energy related emissions [6]. From this data it becomes evident that energy efficiency in buildings is one of the five most effective measures for decarbonisation in the energy sector, offering lower operation costs, and environmental and economic benefits[7].

Central to the transitioning towards net-zero energy buildings are solar photovoltaic technologies which have the potential to reach this goal. In this regard, a building aiming to attain zero emissions should be able to harness energy from the surroundings. PV technologies play a key role as building integrated photovoltaics (BIPV), where a PV cells become part of the building envelope, replacing other building materials as exterior walls, windows, facades or roofs,

providing heat insulation, weather protection and generating energy [8, 9]. With an estimated lifetime from 30 up to 50 years are feasible for building integration [8, 10, 11]. Additionally, the BIPVs provide the electric energy where the end user is located at, and with an appropriate energy storage system or connection to the grid electrical energy can be provided when needed [12]. On the contrary, the main drawbacks are higher costs, when compared to traditional PV modules. More labour costs than for usual PV installations and lower efficiencies of power generation are often quoted as the biggest disadvantage of BIPV systems when non-conventional PV panels like semi-transparent PVs are installed as building facade and window replacements.

Amongst the building components, windows have a considerable impact on energy consumption and indoor environment. It has been reported that optimum window design and glazing could reduce residential building energy consumption between 10 - 50% in most climates. Additionally, for commercial, institutional, and industrial buildings, a properly specified fenestration system could reduce lighting and air-conditioning costs between 10 – 40% [13-18]. Significant reductions in thermal transmittance, or U-value, of fenestration products have been achieved through the use of multiple glass panes enclosing air or inert gas to reduce conduction and convection, and low emissivity coatings on the glass surfaces to reduce long-wave heat exchange [19]. Strategies to manipulate glazing spectral response have also been developed. Examples of this approach are tinted glass panes, which help to absorb radiation, or the application of thin film coatings to reflect radiation [19].

Novel technologies applied to regular windows, like the afore mentioned, are called smart windows and have gained much attention in the efforts made to increase building efficiency. Smart windows fall in to the category of adaptive facade s responding in a smart way from the external environment using chemicals or physical properties to control light transmittance and solar irradiation like ultraviolet (UV), visible and near-infrared (NIR) [20].

Smart windows have a prominent role in buildings being designed to reduce overheating and glare issues and offset the effects of thermal bridges at building envelope interfaces associated with high thermal losses. Traditional windows are usually static building components, contrasting with unpredictable changes of temperature and solar radiation. Therefore, achieving the trade-off balance between desired solar heat gain, daylight and outside view, and at the same time preventing glare and overheating, is the main objective of these devices. [21]. Some smart windows can regulate the amount of transmitted solar and long-wave radiation in response to an applied stimulus, such as heat (thermochromism), electricity (electrochromism) and light (photochromism), having demonstrated significant potential for reducing energy consumption in buildings [15, 17, 22]. Moreover, smart windows can also be used for electricity generation when PV systems like thin PV films, semi-transparent PV or hybrid PV thermal systems among others have been integrated into them to produce clean onsite energy.

1.2 Problem statement and research motivation

The current demands of environmental comfort and the need to improve energy efficiency for both new and existing buildings has motivated research into finding solutions to control the incoming solar radiation, as well as ensuring occupant thermal and visual comfort whilst generating energy onsite. Windows as building components offer the opportunity of addressing these issues in buildings. Building integration of photovoltaics permits building components such as semi-transparent façade, skylights, and shading devices to be replaced with PV. The solar cells are commonly attached to the rear of a glass and some other have transparent cover with a diffuse reflective surface provided in the spaces between the cells. Thus, the reflector diffuses the incident solar radiation through total internal reflection to the solar cells within the front cover glass allowing capture solar direct and diffuse radiation. In this regard, progress has been made in photovoltaic material science, where smart window development has evolved in

areas such as semi-transparent PV, electrochromic and thermochromic materials, luminescent solar concentrator, and the integration of each of the latter technologies to buildings, specifically windows. However, the PV systems still dealing with size and weight issues, high labour/installation cost, overheating and handling after its life span is over. In addition, some other technologies require an external stimulus e.g., electrical making difficult its installation. The research gap presents the opportunity to develop a smart window capable to minimize the drawbacks of the current technologies being capable to automatically responds to climate by controlling the amount of solar light and heat entering to the building, and generating onsite energy, thus offering the potential to contribute with energy loads and control energy consumption within buildings.

1.3 Aim of the thesis

The aim of this research was to design and develop a novel static concentrating photovoltaic (PV) system, being suitable for building integration as window or glazing facade. The developed smart Concentrating PV (CPV) system should be lightweight, low cost, eco-friendly and able to generate electricity.

1.4 Objectives of the thesis

The objectives set for this research were the following:

- To expand the smart window membrane scope developing new thermotropic membranes.
- To validate the working principle of this novel device through ray tracing modelling.
- To characterise the smart window prototype components and the device itself under lab-controlled conditions.
- To evaluate the smart window performance under outdoor conditions.

All the latter leading to develop and build a prototype that can be thought of as an electricity-generating smart window designed to automatically control the solar radiation entering buildings while generating clean electricity.

1.5 Thesis structure

Chapter 1: Introduction

This chapter presents general background information about this research project, building scenario and net-zero energy buildings. The key role of windows in buildings is highlighted, and it is shown how the benefits of smart window's provide opportunity to help to mitigating energy consumptions in buildings, in alignment with the aims and objectives of the thesis.

Chapter 2: Literature review

In this chapter important topics regarding PV technologies are covered: materials, novel PV technologies, reviewing its applications, efficiencies, pros-cons, experimental research done through simulation and software availability are discussed in detail. The chapter also, provides an overview of the PV concentration concept and technologies, like luminescent and static solar concentrators. Lastly, the chapter reviews the smart window concept and its applications, material development and reports on experimental research done so far.

Chapter 3: Methods & materials

In chapter three details of the materials selection process are provided with a focus on the thermal and optical characterisation of the selected polymers and gelling agents in the thermotropic membrane. Details of the design and fabrication of the smart window prototype for indoor testing with optical and electrical characterisation of the device and its components are presented. Ray tracing modelling concept validation and indoor-outdoor experimental settings are presented as well.

Chapter 4: Design and development of a thermotropic membrane for novel smart window

Chapter four presents the selected polymers HPC, HPCM and PNIPAM tested in liquid state and membrane bound. The process of testing the suitability of the selected polymers for smart window application is described in detail in this chapter. Samples synthesised at different weight percentages were characterized optically and thermally using differential scanning calorimetry (DSC) and Fourier transform infrared spectroscopy (FTIRs). Moreover, environmental scanning electron microscopy (ESEM) pictures were taken to see deeper into the membrane structure.

Chapter 5: Indoor optical, electrical, and thermal characterization of smart window prototype

This chapter reports on the optical, thermal, and electrical characterization of the smart window prototype and its components. The characterisation process was carried out under controlled indoor conditions inside the laboratory using three irradiance levels: low 170 W/m², mid 400 W/m² and high 700 W/m². Additionally, a 97% reflectance layer was attached to the smart window to validate the device's concept comparing results against raytracing simulation.

Chapter 6: Design, fabrication, and outdoor testing of smart window prototype for electricity generation and daylight control

In chapter six the smart window outdoor performance is evaluated. The experimental setting for this experiment considered three different south facing angle inclinations 30°, 60° and 90°. Another single pane window was used as a reference to determine the smart window performance. Temperatures in both windows components such as light transmittance and power output were examined throughout each experimental test.

Chapter 7: Conclusions

This chapter summarises the main conclusions regarding the design and development of the smart window and the evaluation of its performance under indoor and outdoor conditions. The conclusion chapter closes with an outline of recommendations for future work.

Supplementary information necessary to understand this work in detail can be found in the Appendix A at page 141.

Chapter 2

Literature review

This chapter presents a review on intelligent window technologies that integrate renewable energy technologies with energy saving strategies contributing to potential solutions towards sustainable zero-energy buildings. Within this work a review is given on the current technology of windows for electricity generation. It includes building integration of PV systems for glazing facades, windows, and their components applications. The chapter further investigates the different types of solar cells suitable for these applications, e.g., Si, thin film, organic and dye sensitized solar cells. The thermal, optical, and electrical performance for building integrated PV systems along with their effects on building performance are discussed. In addition, complex systems such as solar thermal PV windows, building integrated Concentrating PV window including organic dyes and Quantum Dots based Luminescent solar concentrator (LSC) are also reviewed. Finally, the recent research in smart window integrated PV systems are introduced focussing on those suitable for electricity generation and dynamic control of solar radiation entering the indoor space through the window systems. Overall, this chapter aims to provide a comprehensive overview of the potential impact of the integration of smart window technologies in the energy efficiency of buildings. More specifically this chapter provides a comprehensive evaluation of intelligent windows focusing on state-of-the-art development in windows that can generate electricity and their electrical, thermal, and optical characteristics.

2.1 Building integrated PV technologies.

Traditionally, PV power plants needed to be situated on extensive areas of land and have therefore been located outside cities requiring large transmission lines

(cable) to reach load centres [23]. This can be avoided by integrating PV directly into, or mounting onto, buildings i.e., Building Integrated PV (BIPV). Aside from the inherent power generation function of BIPV systems, they can also provide material saving when they replace building components such as façades, windows or shading devices [24]. Hence, BIPVs may provide savings in materials and labour, as well as reducing electricity costs, therefore providing additional economic benefits for the building envelope [25]. It is also becoming increasingly popular to integrate PV into building windows or glazed façades to offer aesthetically pleasing features to buildings [26]. Most type of PV technologies illustrated in Figure 2.1 are adaptable to windows.

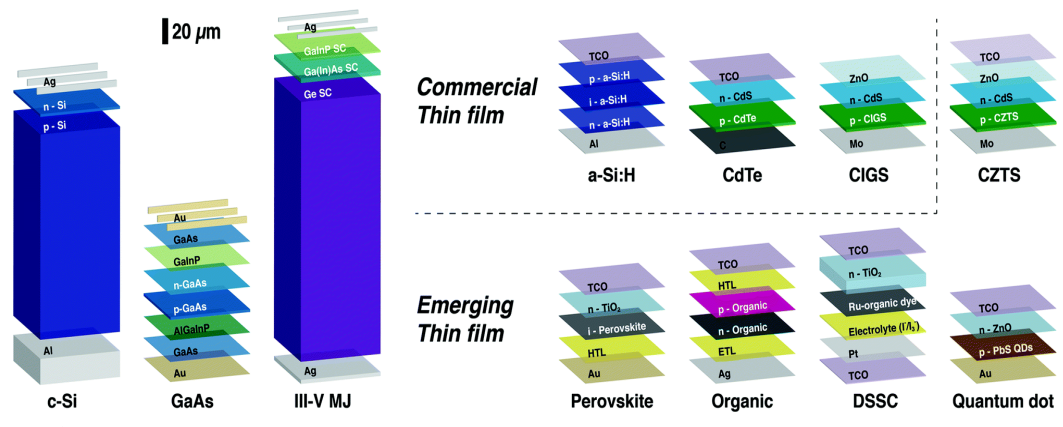


Figure 2.1 PV technologies suitable for window integration. Wafers c-Si, GaAs, III-V and thin films [27]

One of the most commonly materials used in solar cells is the crystalline silicon (c-Si) solar cells with an efficiency of approximately 22% [28], and the market share of the c-Si was around 90% in 2017 [29, 30]. Gallium arsenide (GaAs), another common material used for solar cells offers low non-radiative energy loss, high absorption, direct bandgap with the solar spectrum [28] and 24%-28% efficiency [31, 32]. However, high manufacturing costs limit GaAs technologies such as III (Al, Ga, In) - V (N, P, As, Sb) multi-junction solar cells despite achieving maximum efficiencies of 44.7% [27, 33]. Thin films on the other hand are constructed of thin semi-conductor layers with a solid backing material which reduce the quantity of







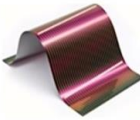


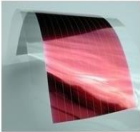
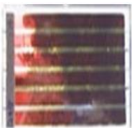

material required and therefore the production cost compared with regular Si cells [34, 35]. Thin film types include a-Si as the most commercially used film due to its abundance and non-toxicity with flexible module production and low substrate cost, giving efficiencies of 5–7%, but is susceptible to degradation [35, 36]. CdTe, another common material use for solar cells, is a stable compound with a direct band gap and large absorption coefficient producing cell efficiencies of 21 % [37] that can be synthesized via a wide variety of methods although showing high parameter variation in identical devices [38, 39]. Copper indium gallium diselenide (CIGS) shows maximum efficiency of 22.3% manufactured in lightweight building material products with further research currently investigating its use in flexible substrates for better efficiencies at low-cost and longer lasting devices [40, 41].

Emerging thin film technologies include $\text{Cu}_2\text{ZnSnS}_4$ (CZTS), similar to CIGS, although produced from non-abundant elements with Zn and Ga replaced by In and Sn respectively [42], achieving highest efficiencies at 12.6% [43]. Nevertheless, there are voltage losses observed in CZTS due to recombination at bulk material defects and charge extraction interfaces. Perovskite is a low cost manufacturing compound made from hybrid organic-inorganic lead or tin halide-based material with a light-harvesting active layer, reported to operate at a 22.7% record high efficiency [44-46]. On the other hand, organic semiconductors are a promising alternative with the advantage of combining cheap production cost and plastic properties, but some also alternate with inorganic semiconductors. These conjugated polymers can be processed by techniques not available to crystalline inorganic semiconductors. Unfortunately, conversion efficiencies are low within the range of 3%-11% [47-50]. Dye-sensitized solar cells (DSSC) are comprised of TiO_2 , a dye, an electrolyte, and a conductive glass. The working principle of DSSC starts with incident light upon the surface of the solar cell being absorbed by the dye molecules causing electron excitation. Electrons in the excited state of the dye are then transferred to the back contact with electrons then flowing through an external circuit to provide electrical charge. Electrolytes can be used as an electron

mediator between the TiO_2 and counter electrode [51, 52]. Another novel technology called Quantum dots (QDs) has been gaining researchers attention due to its ability to harness direct and diffuse radiation. QDs are semiconductor nanocrystals which have diameters of less than 10 nm and due to their size-dependent photoluminescence, chemical stability, broad excitation range, narrow emission peak, tuneable stocks shift and resistance to degradation [30], compared with traditional organic dyes, became a promising material for several research fields [53].

Conventional Si PV cells are now a well-established technology with an emerging trend in using them as semi-transparent PV (STPV) replacing glazing in buildings. This technology is comprised of common solar cells encapsulated between glass panes using EVA (ethylene vinyl acetate) film with variations of glazing transparency achieved via separation of the PV cells at different distance intervals [51]. Thin PV films have gained a lot of attention due to their low cost and high optical absorbance compared to Si cells, combining energy production with high transparency thus being suitable for building integration to get better indoor conditions. However, currently the low efficiencies still limit wider usage [34]. Table 2.1 shows examples of building integration, efficiencies, and transmittance for Si mono- and poly- crystalline, amorphous Si, thin films (CuInGaS_2 and CdTe), organic PV and DSSC.

Table 2.1. Depicts Si (amorphous and wafer), thin films (CuInGaS₂ and CdTe), polymer and DSSC cells integrated into a building as a façade, window, cladding panels, and roof.

PV technology	Building Integration	Efficiency	Transmittance
<p>Silicon</p> <div style="display: flex; justify-content: space-around;"> <div style="text-align: center;">  <p><i>Monocrystalline</i></p> </div> <div style="text-align: center;">  <p><i>Polycrystalline</i></p> </div> </div>		14-22% [14]	It may vary as the gap among cells
<p>Amorphous Si</p> <div style="display: flex; justify-content: space-around;"> <div style="text-align: center;">  <p><i>Amorphous Si</i></p> </div> <div style="text-align: center;">  <p><i>A-Si different colours</i></p> </div> </div>		5-10% [35]	8% [54]
<p>Thin films</p> <div style="display: flex; justify-content: space-around;"> <div style="text-align: center;">  <p><i>Copper Indium gallium diselenium</i></p> </div> <div style="text-align: center;">  <p><i>Cadmium telluride</i></p> </div> </div>		16%[55], 9%[56]	Up to 85% [57]
<p>Organic</p> <div style="display: flex; justify-content: space-around;"> <div style="text-align: center;">  <p><i>Polymer</i></p> </div> <div style="text-align: center;">  <p><i>Dye sensitized solar cell</i></p> </div> </div>		10% [58], 6%[59]	30% [54] 60% [60]

2.1.2 PV window simulation

Semi-transparent PV windows are an effective solution for providing simultaneously daylight illuminance and electricity generation with various degrees of solar radiation and natural light penetration [61]. However, it is important that these PV windows have suitable transparency levels and colour to satisfy visual needs and comfort. Hence, the two main goals for PV window performance optimization are: improve daylighting and energy production [62]. In addition, the interaction between the PV and buildings cannot be neglected.

There is a variety of simulation tools available for predicting the PV windows' performance and their effects on building performance. e.g., its electrical outputs, their effects on indoor daylighting, heating, and cooling energy demand. Such tools include Daysim, Energy Plus, Ecotect, Design Builder, ESP-r, PVsyst, COMFEN, PROMETHEE and StatSoft amongst others.

Characteristics of PV window systems to focus upon include the material type, the window to wall ratio (WWR), transmittance and efficiency. Each of these factors play an important role in device performance and will therefore have repercussions for building performance and simulation. Chen et al. [63] tested five STPV glazing units with different solar incident angles and connected electrical loads using a SERIS indoor calorimetric hot box and solar simulation. The findings showed that the solar heat gain coefficient (SHGC) is lower in a double-glazed STPV glazing compared with laminate STPV glazing due to its low-e coatings. Furthermore, power generation is significantly reduced upon increasing the angle of incident solar radiation from 20% for 45° to 70° and 5% for 0° to 45°. A global feasibility evaluation for STPVs (DSSC) was conducted by Lee et al. [64] in six representative cities with diverse climate zones. For the energy simulation ESP-r software was used in accordance with standard building envelope parameters from the American Society of Heating, Refrigerating and Air-Conditioning Engineers (ASHRAE). The cities and climate zones simulated were the following:

Miami (zone 1), Sao Paulo (zone 2), Sydney (zone 3), New York (zone 4), Seoul (zone 4), Berlin (zone 5) and Moscow (zone 6). The results from the simulation showed that power output was 12% for Miami, 20.5% for Sao Paulo, 18.9% for Sydney, 21.9% for New York and 15.9% for Seoul with each percentage related to the total building energy consumption. Thereby, in zones 1 to 4 (hot to mixed climates) results showed that STPV is suitable for these climates. Furthermore, the building performance can be optimized with WWR, orientation and visible transmittance. Chae et al. [65] evaluated energy conversion, electrical and optical effects on a mid-size commercial building with 3 different semi-transparent solar cells; a 120-nm-thick intrinsic a-Si:H absorber (PV1), a flat solar cell with a 180-nm-thick a-Si:H absorber (PV2) and a textured solar cell with a 180-nm a-Si:H absorber (PV3) in six different locations across the U.S. Significant differences in the total energy consumption were recorded by adjusting the thermo-optical characteristics of the BIPV window and achieving HVAC energy reductions at low latitude sites. Wong et al. [66] tested the interaction between different I-V regions in Japan from north to south, and from cold to warm climate, on two STPV with 20% and 50% radiance transmission with a 3kW capacity each. Thermal balance, power generation, daylighting, and indoor conditions in a south facing dwelling rooftop were modelled and validated against a prototype scale. STPV with 20% has a negligible energy saving effect due to the overheating against the low levels of energy saving: conversely, the STPV 50% radiance transmission achieved energy savings of 5.3% in heating and cooling loads. The maximum lighting saving was obtained in region of Kagoshima with 0.7% energy savings being negligible, indicating STPV is suitable for cold regions but not for warmer regions due to overheating. Poh Khai et al. [67] investigated six semi-transparent BIPV windows of an open market building in Singapore, testing the overall performance and effect of WWR. The study investigated the connection between the increase and decrease of cooling loads, artificial lighting and energy generation proving that such technologies are suitable for tropical south-east Asian weather.

When investigating the building integrated PV windows, the surrounding environment should be considered as well, e.g. urban environments can limit solar exposure, therefore a shadow projection study must be done to verify if the potential site is suitable or if the PV system must be customized [68]. Many numerical radiation algorithms have been developed to avoid the inherent risk of mismatching PV technologies with certain climatic conditions and localities. Traditional solar radiation models can only partially solve these problems as they are adequate only for terrains and rooftops, namely 2-D, whereas facades at the vertical point of view will require a 3-D approach [68, 69]. Empirical methods, transposition methods, diffuse radiation models and monthly mean radiation at sloping surfaces and for other vertical surfaces can be used to address this [70-74]. Complementary to this, in table 2.2 can be seen A summary of PV window simulations with principal characteristics, performance and the software used in these investigations.

Table. 2.2 Summary of relevant simulations performed on STPV featuring characteristics of STPV as WWR transmittance, efficiency and software used.

Type	Integration	Software	WWR	Transmittance	Efficiency	Ref.
Organic, A-Si	STPV window	Energyplus	<50%, >50%	30%,8%	3%,5%	[54]
Poli-Si	STPV roof	Energyplus	-	20%,50%	14.3%	[66]
A-si, μ c-Si	STPV windows	Energyplus	10%-100%	50%,80%	8%,5.9%,3.3%,4.4%,5%4.7%	[67]
A-Si, mono-Si, CuInSe	STPVs	-	-	20%	6%, 17%,11%	[75]
Si	STPV window	Energy plus	20%-70%	-	-	[76]
Si	Semi-transparent single-glazed	Energyplus	-	20%	-	[77]
A-Si	Double glazed module	TRNSYS	-	10%	7%	[78]
Poly-Si, A-Si, Organic	STPV window	Daysim, Energy Plus	40%,60%	10%-50%	15%,10%,10%	[79]
DSSC	Window	Ecotect	50%	25%,30%,38%,45%	7%	[80]
Multi-Si	Skylight	-	-	20.1%	10.8%	[81]
A-Si	STPV windows	Design Builder, energyPlus, PVsyst, and COMFEN	11%-88%	0%10%,20%,30%,40%	-	[82]
Mono-Si	shading PV device	PROMETHEE	-	-	-	[83]
Poli-Si	STPV glazing	-	-	92%,43%	-	[84]
A-si, μ c-Si	STPV windows	Energy Plus	43%	10.6%	6.3%	[85]
A-Si	STPV window	StatSoft	-	10%	7%	[86]

Additionally, to the use of BIPV as windows, BIPV can also be used as window associated components such as shading devices, exterior cladding panels etc. all of which generate energy onsite [87-90]. Figure 2.2 provides examples of BIPV integrated as shading devices.



Figure 2.2. Different PV shading devices, (a) with a more aesthetical approach [91] and (b) with louvers design [92].

Radut et al. [93] developed a multifunctional integrated photovoltaic window (MIPVW) consisting of photovoltaic blinds comprised of 36 PV cells with advanced maximum power point tracking (MPPT) powered by a stepper motor. The results showed that compared with a PV window with similar characteristics the MIPVW generates 20% more energy. Kang et al. [94] assessed the performance of a double-layer window façade design using PV modules attached to venetian blinds for energy generation. This PV blind used tilt angle, azimuth, PV area and frame distance from the window as variables and found that PV thickness and inclination angle affected energy generation. Additionally, ventilation effects on the blind were tested and concluded that efficiency was reduced by 4.3% without ventilation the PV module reached 78 °C whereas the ventilated reached 58.4 °C. Moreover, the energy production reached 509 Wh/m² on the daytime. Kim et al [95] tested motor controlled louvres coated with PV cells and measured the intensity of sunlight and daylight with motor motions controlled by climatic condition software. The results showed that the energy generated is dependent on the PV size and inclination angle. Sun et al [96] studied different angle positions for two different PV claddings in a building in Hong Kong finding that 20° is the

optimum tilt angle instead of local latitude for maximum electricity generation. Yoo et al. [97] assessed BIPV modules for shading purposes, with the aim to protect from solar radiation in summer whilst simultaneously allowing light to penetrate the internal space in both summer and winter. With one year of analysis the average efficiency of the sunshade panel was found to be 9.2%, with a maximum of 20.2% in winter and a minimum of 3.6% in summer.

2.1.3 Solar thermal PV windows

Combining PV and thermal collector (PV/T) technologies have gained significant attention since they solve the issue of inconvenient overheating of solar cells [98, 99] which causes decreased efficiency induced by an increase in resistance. PV/T systems are engineered to carry heat away from the PV cells thereby cooling the cells and thus improving their efficiency by lowering resistance [100-102]. Solar collectors are divided in two groups: non-concentrating (stationary) and concentrating (dynamic). Stationary collectors have a single area to absorb solar rays, whilst concentrating collectors have concave reflecting surfaces to focus solar rays into a smaller receiving area [103, 104]. Figure 2.3 shows a schematic representation of the stationary collector and parabolic-trough collector with tracking system.

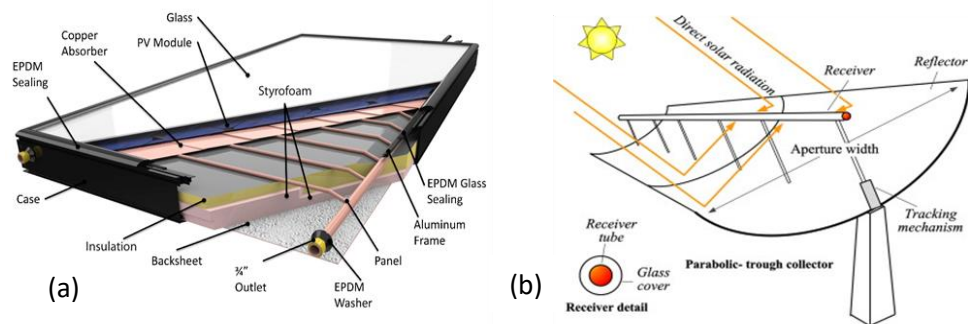


Figure 2.3. (a) Components comprising a stationary PV/T and (b) Schematic design of a parabolic-trough collector with tracking system [105].

PV/T collector technologies are comprised of crystalline or amorphous silicon PV, liquid or air collectors, a flat-plate or concentrating technologies with or without transparent cover [106]. Additionally, the absorber structure changes according to the needs of the system, being a flat plate tube, extruded heat exchanger, rectangular tunnel with or without fins, sheet-and-tube structure, roll-bond heat exchanger or a micro-channel heat pipe array/heat mat [107]. PV/T electrical efficiency can be measured using tools as I-V curve for its characterization, conversely the thermal part has its complications and requires the application of equations (1) and (2) to describe PV/T module efficiency:

$$\eta_t = \frac{\dot{m}C(T_{out}-T_{in})}{GA} \quad (1)$$

$$\eta_e = \frac{V_{mpp} I_{mpp}}{GA} \quad (2)$$

where \dot{m} is the mass flow rate, C the specific heat capacity of the coolant, T_{in} and T_{out} are the coolant temperatures at the inlet and outlet, A is the collector aperture area, G is the incident solar irradiance normal to surface and with V_{mpp} and I_{mpp} the voltage and electric current at maximum power point operation [108]. Davidsson et al. [109] developed and evaluated a hybrid solar window designed with laminated PV cells and tiltable reflectors used to focus incoming radiation and control the amount of daylight entering the building. The results of the simulations showed that electricity generation can be increased by 35% using this prototype in comparison with flat PV modules. In another project Davidsson et al. [110] tested the window performance of a system connected to a thermal storage tank of 620 Litres to assess the intricate relation between the PV/T window and the building, details are shown in Figure 2.4. The findings show that the auxiliary energy load for the building was 1000 kW h less using a solar collector on the roof compared against the building with the PV/T window. However, the study also showed that if the solar collector is removed from the building the auxiliary energy load is around 600 kW h which is higher than when the PV/T window is used.

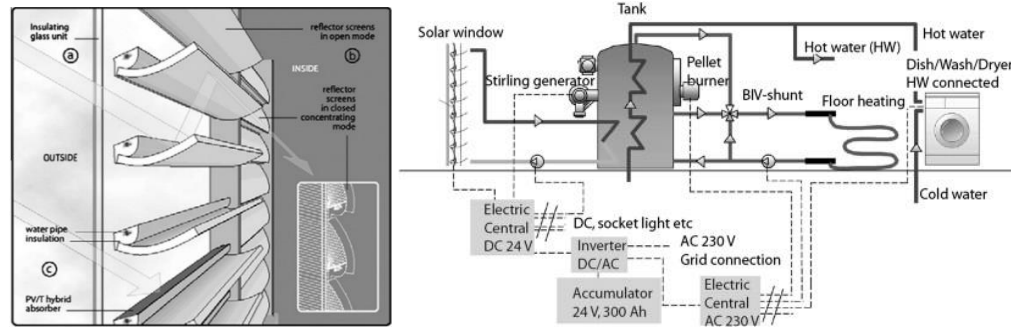


Figure 2.4. Depiction of the hybrid solar window and full PV/T system.

Ulavi et al. [111] presented a hybrid solar window with compound parabolic concentrator using a selective wavelength to divide the sun beam into daylighting and heating. This device was analysed as a window in a vertical position and as a skylight in a horizontal position. Thermal efficiency was found to be ranging from 18% - 24% for a south orientation with geometries from $-25^\circ \leq \text{Nominal half-acceptance angle } (\Theta_c) \leq 45^\circ$. Sabry et al [112] carried out numerical simulations of the performance of a multi paned smart window integrated with water-cooled high efficiency third generation GaAsP/InGaAs QWSC (~32% efficiency) solar cells which were illuminated by two-axis tracking solar concentrators at 500 \times in the inter pane space. Three different direct solar radiation intensities of 400, 600, and 800 W/m² were applied on the window's front pane with a set ambient temperature, water inlet temperature and water flow rate of respectively 273 K, 283 K and 0.01 kg/s. At an incoming solar radiation of 800 W/m² it was found that the water temperature was increased by 5 °C as it passed through the tube supporting the solar cells.

2.1.4 PV technologies summary

This section covered information regarding the materials used on BIPV as Si GaAs, Multi Junction, commercial thin films (CdTe, a-Si;H, etc), emerging materials (Perovskite, organic, DSSC, etc). As a result of this comprehensive review, a summary is added in the following to simplify the main findings and features that the different technologies systems presented here offer. Additionally, the building

integration of this technologies as they can replace building parts, be used as claddings o envelopes to bring cover to certain areas, shading devices, windows, facades, and the software used to simulate their performance has been discussed. Nevertheless, despite the research done on these technologies some drawbacks can mitigate the BIPV performance. One of these drawbacks is the overheating on the PV cell/device, thus other technologies like PV/Thermal gained attention because they can mitigate this issue and reutilize the heat to transform it into energy or be used to boil water. Table 2.3 presents the summary of relevant features and technologies in BIPV.

Table 2.3. Summary of materials, applications, technologies, and benefits of BIPV

BIPV	PV type	Application	Energy saving & generation	Benefits
PV window / facade	Thin films multi-junction, Organic PV cell, DSSC.	Office, residential, windows, facades	Energy generated comprised 12%-20% of building consumption in 5 different locations[64], can save 30% of the total HVAC system energy comparing against double-pane glass [65]	Thermal balance, daylight, and indoor controlled conditions
Shading / cladding PV/roof	c-Si, wafer, thin film, organic	Venetian blind, louvers, cladding, sunshade PV modules, roof-mounted PV	20% more energy generation than vertical glazing PV widow[93], power generation can achieve 509 Wh/m ² [94]	Daylight, environment, and indoor overheating protection
PV / thermal	c- Si, GaAsp/ InGaAs	PV sunshade module and thermal collector	35% more energy production per unit area of PV cells vs. flat PV module at 90° [109]	Overheating, daylight control, boiling water

2.2.1 Building integrated concentrated PV window systems

Concentrated Photovoltaic (CPV) is a combination of Photovoltaic (PV) cells or modules with an optical system. This system (Solar Concentrator) is used to increase solar flux hitting the PV area, working at higher irradiation levels than conventional PV arrays and obtaining a higher conversion efficiency [113, 114]. There are 3 leading types of CPV system: they are either refractive and reflective technique based which are the most commonly used, the other one is luminescent PV concentrating system [115]. An important characteristic of CPV is the concentration ratio, defined by the incoming irradiance ratio at the concentrator aperture which is usually expressed in Suns or x [116]. According to the classification of the geometric concentration ratio, a CPV with a concentration ratio below 10 suns is referred to as a low concentration system. Medium concentration systems have 10-100 suns, high concentration system have 100-200 suns and ultrahigh system have a concentration ratio of over 2000 suns [115]. High CPV require mechanical tracking systems with low tolerances of usually less than 0.2° and need more space for installation, making building integration complex. Medium CPVs are divided into two main types: parabolic troughs and Fresnel lenses or mirrors. Medium CPVs that fall in the range of 65-85x make building integration complex as they also require a tracking system. However, by decreasing the concentration ratio building integration can be achieved. Conversely, low (4x) CPV concentration systems do not depend on solar tracking as they can collect both direct and diffuse radiation, hence can remain static, and are therefore suitable for façade and window applications, although in lower concentrations [117-119]. Furthermore low CPV requires the widest acceptance angle possible, which is defined as the angle of incoming radiation when 90 % of the maximum power is generated [120]. This is achievable only using non-imaging optics which allow the collection of diffuse light as well as direct light [121, 122]. Tang et al. [123] tested concentrators with concentrating ratios <2 and >2 finding that exceeding 2 concentration ratio variations to the inclination can improve the

system performance. Li et al. [119] presented two CPV with 3.06 (3×) and 6.03 (6×) and half-acceptance angles of 10° and 3° respectively. Their results showed that it was unnecessary to adjust the CPC system with a concentration ratio of 3x tilt angle in a single day, but it must be adjusted throughout the year.

2.2.2 Parabolic concentrator technologies on windows

The integration of a PV system into a window requires analysis of which technology will best suit the buildings needs given that every scenario and location is different [115]. Once difficulties such as concentrator geometry design and elimination of tracking systems are resolved CPV windows are an excellent option to produce clean onsite energy [124]. CPV integrated to windows can also be used as a shading device or as blinds, therefore offering several ways to reduce energy consumption in buildings via PV integration. Technologies such as Compound Parabolic Concentrators (CPC) with non-imaging line axis optical systems and V-trough reflectors best suit building integration with good performance and a lower cost than regular PV panels or thermal collectors [125]. Novel designs of 2-D and 3-D CPC are acknowledged as the best stationary designs. Table 2.4 presents relevant work conducted on CPV windows and Figure 2.5 shows the variation in design of CPCs.

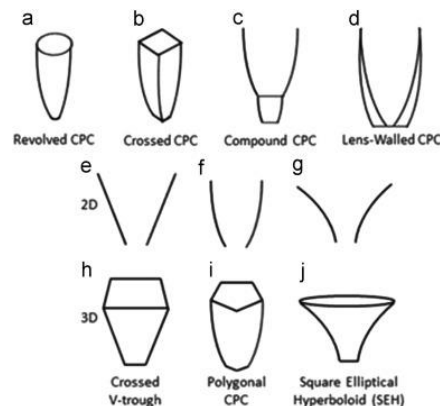

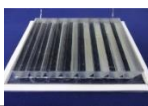
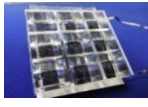






Figure 2.5. (a) The revolved CPC. (b) The Crossed CPC. (c) The Compound CPC. (d) The Lens-Walled CPC. (e) V-trough. (f) CPC. (g) Compound Hyperbolic Concentrator. (h) 3D square aperture V-trough. (i) Polygonal aperture CPC. (j) Hyperboloid with an elliptical entry aperture and square exit aperture[115, 126].

Experimental work done by Abu-Bakar et al. [127] assessed the performance of low CPV with a geometrical concentration ratio of 3.6× and integrated with a 1 x 1 cm monocrystalline laser grooved buried contact Si solar cell, named: Rotationally Asymmetrical Compound Parabolic Concentrator (RACPC). The I-V curve was tested indoors at standard conditions. Findings showed that RACPC increased the maximum power ratio system by up to 3.33× presenting a greater power output in comparison to non-concentrating cells within a half acceptance angle, with 84% optical efficiency at regular incidence. The outdoor characterisation of Dielectric compound parabolic concentrator (DiACPC) was presented by Sarmah et al. [128] featuring with 2 strings of 14 solar cells, 300 mm × 300 mm, in series with a concentration ratio of 2.8x and acceptance half angles of 0° & 55°. The device was tested in Edinburgh in different weather conditions and compared with a flat PV cell system in real time. The results showed that DiACPC has an efficiency with an average power output of 0.13 W and 5.88 W for a 943 W/m² radiation input, being 2.17 and 2.27 times higher than the flat-plate system for rainy and sunny days respectively. Bunthof [129] presented the impact on shading for a flat CPV system. This system comprised a Fresnel lens-based concentrator, a novel flat planar optic concentrator, and a 4 × 4 panel of these flat optics. The panel itself comprised of 10 cm × 10 cm Fresnel lens made of PMMA as a concentrating optic, a 4 cm × 4 cm planar focusing optic, a 1.3 mm × 1.3 mm TJ III/V cell, a bypass diode and a copper heat sink and integrated wiring. Findings showed a concentration efficiency in the range of 0.66–0.77, which is related to the same range as the Fresnel lens system. Moreover, this research showed that multi-receiver panel shading gives a loss in performance from 7 - 12% proportional to electrical interconnection, since individual receivers do not suffer from this loss. Fernandez et al. [130] had proposed an artificial neural network model to calculate the maximum power using direct irradiance, diffuse irradiance, module temperature and the transverse and longitudinal incidence angles. The findings demonstrated that the model can estimate the maximum power of a low CPV module for building integration with

an adequate margin of error. Conclusions from linear and statistical analyses showed a maximum power of the low CPV module with a margin of error: $R^2 = 0.99$, $MBE = -0.05\%$ and a $RMSE = 2.32\%$. High accurate performance was observed on clear days due to the maximum power provided by direct irradiance as well as on cloudy days when only diffuse irradiance was available. Relevant work conducted on CPV windows is summarized in Table 2.4 which presents a description of the CPV and window integration, concentration ratio, acceptance angle and type of building integration.

Table 2.4. CPV window relevant work summary.

Types	Prototypes	Concentration ratios	Building integration	Acceptance angles	Ref.
3-D static square elliptical hyperboloid		4x	Windows pane/glass	120° (-60°, +60°)	[122]
Linear asymmetric compound parabolic concentrator		2.8x	Windows	0-55°	[131]
Three-dimensional cross geometric compound concentrator		3.6x	Windows pane/glass	70°	[118]
Truncated dielectric asymmetric compound parabolic concentrator		2.8x	Windows	0-55°	[132]
RADTIRC (rotationally asymmetrical dielectric totally internally reflecting concentrator)		4.9x	Double glazing window	±40° along the x-axis and ±30° along the z-axis	[133]
RACPC (rotationally asymmetrical compound parabolic concentrator)		3.66x	Double-glazing window	0-60°	[134]
PRIDE (Photovoltaic Facades of Reduced Costs Incorporating Devices with Optically Concentrating Elements)		2.45x	building façade integration	0-66°	[135]
DiACPC (concentrating dielectric compound parabolic concentrator)		2.8x	building façade integration	half angles of 0° & 55°	[128]

2.2.3 Luminescent solar concentrators

In the 1970's and 1980's special attention was given to fluorescent concentrators [136, 137] with luminescent solar concentrators (LSC) gaining consideration as a PV substitute due to its lower cost and the ability to harness direct and diffuse solar rays, therefore avoiding expensive tracking systems [138]. LSC can be seen as a matrix of dye molecules which absorb light and then re-emit it at longer wavelengths, thus light is internally reflected via total internal reflection (TIR) and guided to the edges where solar cells are placed [139]. Figure 2.6 depicts how a LSC works [140] and Figure 2.7 shows samples of LSC in different colours under UV light.

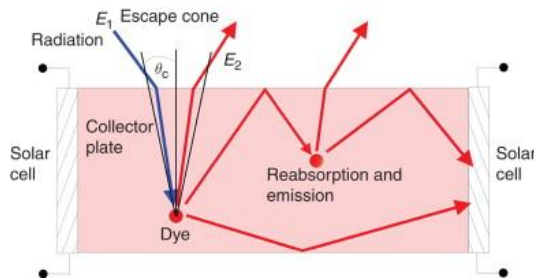


Figure 2.6. The LSC dye absorbs incoming light (E_1) then luminescence is randomly emitted (E_2). Light re-emitted light reaching the collector surface within the escape cone are lost, the rest are guided to the edges by total internal reflection.

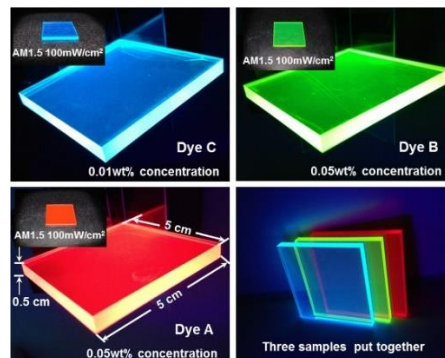


Figure 2.7. Three LSC samples of 5 cm × 5 cm × 0.5 cm size; Dye C LSC with 0.01 weight (wt.) % concentration, Dye B with 0.05 wt. % concentration, Dye A with 0.05 wt. % concentration representing blue, green and red colour respectively under UV light [141].

LSCs can also provide architectural features: Light weight, availability of various colours and degrees of transparency, and flexibility making them a versatile product for incorporation into buildings and suitable for either windows panes or glazed façades. Despite the ability of LSC to collect both direct and diffuse radiation potential downsides relate to the colouring, which links to the dyes and subsequent energy efficiency, affecting indoor visual comfort and lighting needs [142]. LSC efficiency is currently around 7%, affected mainly by factors such as: overall absorption of the dyes, fluorescence & trap efficiency, refractive index of the plate and Stoke efficiency. Future research is needed to solve the drawbacks like self-absorption of the luminescent dyes and escaping emissions beyond the critical angle [143].

Awareness should be raised that LCSs are commonly cast into a transparent plastic sheet doped with organic dye or Quantum dots (QD) [144]. Organic dyes are π -conjugated organic molecules, where the core is flat with all atoms of the conjugated chain lying on the same plane linked by σ -bonds. Absorption bands are the promotion of π -electrons above and below this plane along the conjugated chain moving from ground energy state to an excited higher energy state [145]. Organic dyes can provide high luminescence quantum efficiency (LQE) (near unity), a wide range of colours and improved re-absorption properties with UV stability in new molecular species. Table 2.5 summarizes commercial dyes describing absorption, emission, and quantum yield [145-147].

Table 2.5. Presents a summary of commercial dye characteristics.

Dye	Absorption λ_{\max} (nm)	Emission λ_{\max} (nm)	Quantum yield (%)
Lumogen F Blue 650	377	411	>80
Lumogen F Violet 570	378	413	94
Lumogen F Yellow 083	476	490	91
Lumogen F Yellow 170	505	528	>90
Lumogen F Orange 240	524	539	99
Lumogen F Red 305	578	613	98
Red G	520	600	87
CRS040 (CFS002 Yellow)	440	506	98

In comparison with LSC, Quantum dot crystalline semiconductors suffer less degradation than organic dyes [139], allow to control the red shift between absorption and luminescence and reduce re-absorption yielding, delivering better efficiencies and concentration ratios via dot's sizes [148]. An important aspect of Quantum dots is the quantum yield, described as the quantity of fluorescing photons to the materials incident photons [149]. Moreover, QD have different emission colours directly proportional to its size. Figure 2.8 [150] illustrates the variation of photoluminescence emission colours with sizes for CdSe QD. Additionally, QD stand out for having a large range of applications from bio-imaging, nanomedicine, PV cells, organic polymers, OLED technology and more [151-165].

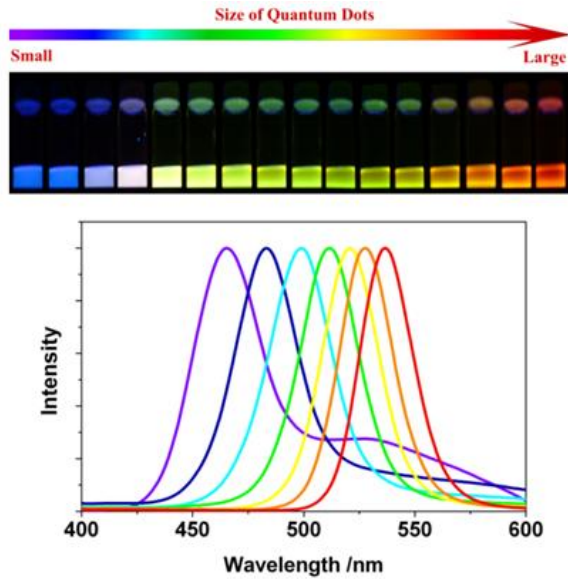


Figure 2.8. The range of photoluminescence (PL) emission colour with size for CdSe QD from small to large, blue to red respectively, using a near-ultraviolet lamp with QD size from ~ 1 nm to ~ 10 nm [150, 166].

Goldschmidt et al. [167] presented a LSC comprising four GaInP solar cells on the plates edges with two plates with different type of dye, showing an efficiency of 6.7% on a 4 cm^2 area with a concentration ratio of 0.8. In addition, it was suggested that 13.5% efficiency can be attained if the light spectrum falls within 650-1050 nm. Another investigation by Currie et al. [144] modelled a tandem LSC with 2 single concentrators made of an organic dye layer within glazing and a GaAs cell showing 6.8% efficiency. Moreover, switching the cell for CdTe or Cu (In,Ga) Se₂ efficiencies were projected to be 11.9% and 14.5% respectively. Slooff et al. [168] tested 0.003 wt. % CRS040 and 0.01 wt. % Red305 dyes on a $50 \times 50 \times 5 \text{ mm}^3$ PMMA plate then adding mc-Si, GaAs or InGaP with a 97% diffuse reflector on the backside and reported an efficiency of 7.1% using 4 GaAs cells in parallel. Bomm et al. [169] developed and characterized a CdSe core/multishell quantum dot LSC. The results showed that QD are well dispersed in a plastic matrix with a quantum yield of 45%. Besides, Si and GaAs cells were added to the LSC's edges to measure power conversion, which was reported to be 2.8%. Gallagher et al. [170] tested 8 small scale quantum dot solar concentrator (QDSC) devices to determine fill and

concentrating factor, the latter was calculated by comparing the developed sample against a polyurethane mirrored perspex mould casted sample without QDs (a), an unmirrored perspex mould casted polyurethane without QD sample with the same PV orientation as QDSC (b) and a sample perpendicular to the incident radiation PV cell (c). Without exception concentrating factors with a minimum of 1.33 to a maximum of 3.05 were observed compared to (a) and better concentration factors from 3.78 to 8.65 when compared to (b). Sample 5, a QDSC of 0.08% volume fraction of CdSe/CdS F2 QD, attained the highest fill factor of 0.7, being 12.5% lower than specifications by the manufacturers of the PV cell. Kerrouche et al. [171] presented research into a stained glass window using previous 3D ray-tracing simulations to predict trapped photons inside the LSC being transported to the edge of the sheet with the aim of calculating power output and optical efficiency. According to the results, the experimental data and 3D raytracing agree well, having $\pm 5\%$ deviation within a wide concentration range (optical density = 0.05–8) and a maximum difference of $\pm 13\%$. Highest power density values were obtained at the prototype edge when it was perpendicular to the source with optical efficiency increasing as the tilt angles does. Thereby, the agreement between simulation and experimental values was 7%, leading to the assumption that this LSC window can generate energy from a wide range of incident light angles with the peak power of 5W. Similarly, a prototype was presented by Fathi et al. [172] incorporating a LSC coating on a window whereby recovery of high energy UV photons can produce energy with the aid of PV cells embedded at the edges of the window. Energy data shows that the device can produce 1.07 W/m^2 at low irradiance (250 W/m^2) and up to 4.28 W/m^2 in standard conditions (1000 W/m^2) with daily estimations of 450 Wh/Day for a 20 m^2 LSC glazing making this prototype suitable for places such as Northern Europe.

2.2.3 Building integrated PV concentrators summary

Solar concentrators present a wide variety of technologies to reduce the PV material and improve the efficiency of these devices. However, predominantly

window integration of these technologies was assessed here, aiming to improve indoor conditions and produce clean onsite energy. Additionally, some drawbacks are in the way to accelerate these technologies to the further stages. One of them is the overheating on CPV due to the high amount of energy concentrated in a small area of PV cell, hence further thermal assessments and cooling through air or PV/T systems can be adapted to solve these issues. Regarding LSC with inorganic, organic and Qdots the issues to solve are related to the degradation, red shift between absorption and luminescence, reduced re-absorption yielding and higher quantum efficiency. Table 2.6 presents the summary of optical characterization and materials used for LSC and CPV windows, as well as relevant research consulted for this review on CPV.

Table 2.6. Summary of relevant research in CPV and LSC window integrated.

Device name	Concentration type	PV cell	Power output	Quantum efficiency	Optical efficiency	Ref.
RACPC	rotationally asymmetrical compound parabolic	Si-mono	0.050 W	n/a	84 %	[115]
PRIDE	truncated asymmetric compound parabolic concentrator	Si	70 W	n/a	>40 %	[135]
LSC/Qdot	CdSe core/multishell Qdots	Si, GaAs	-	45%	-	[158]
LSC/Dye	Glazing with luminescent coating	mc-Si	4.8 W	>60 %	-	[161]
LSC	Fluorescent concentrator	GaInP	580 mV	45%	-	[156]

2.3.1 Smart windows

The application of “smart windows” leads to a decrease in energy consumption of glazed buildings due to the reduction of cooling and heating loads which is achieved by controlling the solar heat and light entering the indoor space as well as mitigating electric lighting demand [173]. These devices must fulfil aesthetic and economic requirements as part of the technical solution for producing net-zero energy buildings [174]. Some smart windows are capable to regulate the amount of transmitted solar and long-wave radiation in response to an applied stimulus, such as heat, being thermo-responsive, therefore is important to present a relevant materials review related with this technology.

2.3.2 Thermotropic materials

Recently novel glazing concepts have been adapted to fenestration using self-adjusting systems to control the incoming light to the buildings. These systems utilise thermotropic materials capable to cloud themselves when warmed up by sunlight and recover clear state when cooling. Two types of thermotropic materials have been used for building integrations purposes: natural polymers, and synthetically produced polymers. Both are currently widespread available in the market [175-177], and both aim to fulfil the demand for inexpensive, non-toxic, and environmentally compatible characteristics.

2.3.3 Hydrogels

Hydrogels are the basis of natural compounds such as gelatine and polysaccharides. Polymeric hydrogels are well known and well examined, and they provide the desired characteristics of a thermotropic material mentioned earlier in this review. These properties make hydrogels extremely valuable to several fields including food science, molecular biology, in vivo drug delivery systems, 3D cell Biology, tissue engineering and microscopy sample preparation [178]. Hydrogels can be chemical or physical cross-linked molecules of which large parts

are composed by hydrophilic groups called “polymer networks”. These polymer networks have the capacity to retain large amounts of water at low temperatures with molecules mixing homogeneously. When the temperature rises the aggregation of the polymer takes place [179-181]. This phase change, characteristic of thermotropic hydrogels, is commonly referred to as sol-gel transition describing a process where a solution turns into a gel state. The threshold for the phase change to occur can be defined by the temperature [182].

2.3.4 Relevant thermo-responsive materials

To continue with the thermotropic materials review, this section revises research relevant to thermotropic materials, to understand in detail their composition, main features and characteristics.

One of the most interesting materials is Ethyl(hydroxyethyl)cellulose (EHEC, a non-ionic amphiphilic polymer containing ethylene oxide (EO) groups, mixed with hydrophobic and hydrophilic structural units. EHEC shows a sol-gel transition occurring at temperatures around 35°C. In addition, the presence of greater amounts of hydrophilic segments in relation to hydrophobic units renders EHEC water-soluble. Furthermore, by the addition of surfactants the aqueous solution of EHEC can become more viscous with increasing temperature, forming stiff gels below the clouding point [183-185].

One of the most used polymers in the world is the Hydroxypropylcellulose (HPC) which has cellulose ether with hydroxyl groups on the cellulose backbone hydroxypropylated. It is prepared by reacting alkali cellulose with propylene oxide at elevated pressure and temperature to yield a highly substituted cellulose ether. Due to the high levels of hydroxypropylation ~70%, it is considered more plastic and relatively more hydrophobic as compared to other water-soluble cellulose ethers. It is soluble in polar organic solvents, like methanol, ethanol, isopropyl alcohol (IPA), and acetone. Solubility of HPC in water is temperature dependent,

easily soluble at temperatures below the temperature below which the polymer starts to phase-separate [186-188].

Another polymer broadly used in several industries like drugs and food is Hydroxypropyl methylcellulose (HPMC) is part of the group of cellulose ethers in which hydroxyl groups have been substituted with one or more of the three hydroxyl groups present in the cellulose ring. HPMC is hydrophilic, a biodegradable, and biocompatible polymer having a wide range of applications in drug delivery, dyes and paints, cosmetics, adhesives, coatings, agriculture, and textiles. HPMC is also soluble in polar organic solvents, making it possible to use both aqueous and nonaqueous solvents [189-191].

Poly-*N*-isopropylacrylamide (PNIPAM) is a thermo-responsive polymer with inverse solubility and a reversible phase transition upon heating. It has a phase change value of 32°C, below this temperature is hydrophilic and water soluble; above 32°C, becomes hydrophobic and a viscous gel that is strongly adherent to tissue. PNIPAM is soluble at room temperature, but its phase change starts at body temperature (37°C); it therefore can be used as a linear polymer, a hydrogel, or a copolymer [192-194].

2.3.5 Smart windows with thermotropic technologies

Hydrogel smart windows have evolved with multifaceted characteristics by mixing different technologies and materials, moving from the affinity intelligent window (AIW) concept developed by Watanabe [195] to new complex solutions [196-199].

In regard of smart window research Wu et al. [200] presented a novel BICPV “smart window” featuring a glazed thermotropic layer (hydrogel) with solar cells embedded on the edges. This window has the feature of onsite energy production and the ability to react to climate changes through controlling the solar and heat gains entering the building, thus controlling the buildings energy consumption. The schematic concept of this novel device can be seen in Figure 2.9.

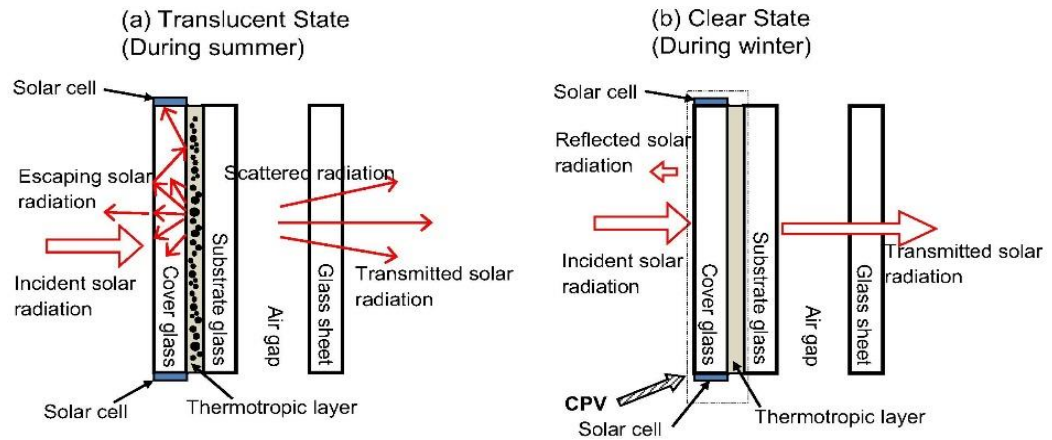


Figure 2.9. (a) light scattering state for electricity generation (b) transparent state for indoor passive heating [177].

In a hot season, when the proposed thermotropic layer is in a translucent state the proportion of light transmitted and scattered through it may vary depending on the heat it is subjected. A large proportion of scattered light is directed with total internal reflections towards the of the edge of the window where optically coupled solar cells are located. When the temperature of the thermotropic layer is below a designed threshold switching temperature (cooler season), the thermotropic layer appears transparent. As opposed to conventional designs with controlled shading devices that reflect in summer uncomfortably high solar irradiation back to the environment the proposed smart window collects and uses the energy with solar cells to generate renewable electricity. In winter, light and heat pass preferentially through the system helping to offset heating and lighting energy demands. Significant optical predictions were made for the proposed smart window. Specifically, CPV with BK7 glazing cover (dimensions 120 mm by 120 mm with a thickness of 6 mm, $C_g = 5$) and thermotropic layer with different reflectance levels were investigated. No significant variation in optical efficiency was observed for the entire solar incidence angles measured. The highest value recorded was 27.4% and lowest 25% when rays were perpendicular to the smart CPV aperture, thus angular acceptance in relation to diffuse solar radiation was suitable for application in Northern European climates. Subsequently, the power output was

optically simulated with the following inputs: aperture area of 1.44 m² with 100 modules each with dimensions of 120 mm × 120 mm × 6 mm, 99% thermotropic reflective layer, BK7 glasses in a south facing system in 2014 in a London climate location with realistic values of direct and diffuse solar radiation from real values on the 30th of June 2014. Results showed that 57W of power output can be generated at around 11:00 on that simulated day.

Connelly et al. [201] developed the thermotropic membrane for the proposed BICPV “smart window” comprised of distilled water, hydroxypropyl cellulose (HPC) and gellan gum. A 6 wt. % HPC sample showed a switching temperature (T_s) of ~42°C with a reduction of transmittance from 90% at 20 °C to ~20% at 60 °C and a reflectivity of ~10% below the T_s to ~50% above the T_s , showing promising performance for smart window applications. A visual description of the thermotropic membrane and the smart window is shown in Figure 2.10.

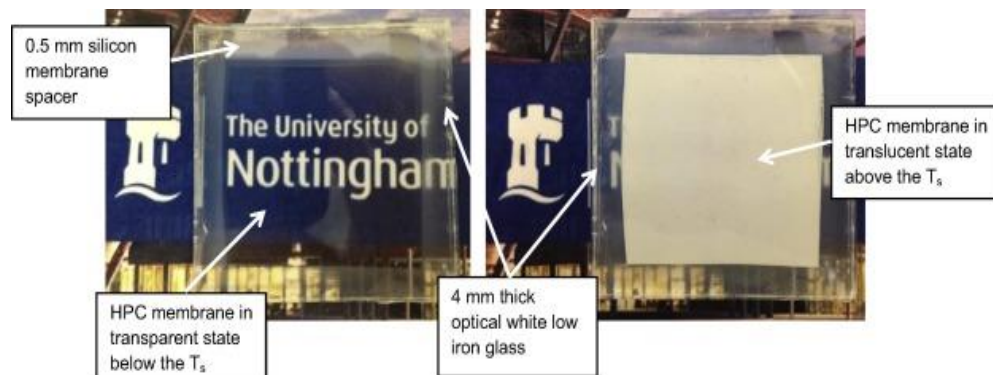


Figure 2.10. Smart window prototype with 0.5 mm silicon spacer, low iron glass and HPC membrane below the T_s (left) and above the T_s (right) showing clear and light scattering state, respectively.

Further work regarding the BICPV smart window for dynamic control in a building was carried out by Allen et al. [202]. Simulations were undertaken using Energy Plus for the system with 4 different tilt angles (0°, 30°, 60°, 90°) installed at a typical office cell located in Palermo, Italy. The results showed that outside ambient temperatures and incident solar radiation are significant factors in the reflection

and transmission indexes of the smart window. The 6 wt. % HPC-based thermotropic window coefficient (SHGC) was between 0.44 and 0.56, and with this, lower than the coefficient of a double glazing with 0.74, the sample was compared to. An annual energy saving of 22% was calculated using the HPC thermotropic window as in comparison to the simulation results for double glazing. Visible transmittance and solar transmittance below the transition temperature of 40° C were 0.9 and 0.74 respectively and above the transition temperature 0.16 and 0.11, respectively.

In addition, other technologies also have been tested as a part of the smart window research. Different combinations of several technologies such as luminescent concentrators, thermotropic, photochromic and electrochromic have been used so far. Debije et al. [203] presented a “smart” window using fluorescent dye in a liquid-crystal host between glass panels. This device can generate power via attached PV cells and allows the user to have control of the amount of transmitted light. Absorption varied by 31% when voltage was applied through the cell, whereas usable light varied just 11% because of the increased efficiency of light collection due to the homeotropic dye orientation. Additionally, this device can switch from “dark” and “bright” states to control light inside the room whilst light emission is attained at on or off state, with the highest light output due to the lowest device’s power consumption point. Wang et al. [204] developed an Energy Storage Smart Window (ESS) integrated multifunctional flexible device. The ESS window is a versatile device comprising an integrated supercapacitor and electrochromism function in one, with polyaniline nanowire arrays as electrodes. The addition of a solar cell permits the device to harness, store and use generated energy efficiently. In daylight the window darkens which blocks heat and sunlight from entering the internal space and is instead converted into energy which can be stored electrochemically and charges the device. When the stored energy runs low the window colour lightens. The ESS window shows high areal capacitance and stability as a supercapacitor and this window can also be used as a power source

for electricity-consuming devices such as LCD screens. Malara et al. [205] developed a new structure for a photovoltachromic window prototype which has two distinct counter electrodes with two physically separated platinum and tungsten oxide layers, in different conductive substrates ordered to be two different intercommunicated electrolytic chambers. This feature permits twofold the self-powered fast-responsive control of the optical transmittance and the production of energy through solar energy conversion. Samples with 397, 360 and 320 mm² catalytic areas produced efficiencies of 2.75%, 2.35% and 1.91% respectively. The study concluded that the larger the interposed Pt-ITO-PEN counter electrode platinum area, the higher the conversion efficiency, with the bleaching process directly affected by the increase of platinum area. Kwon et al. [206] assessed smart window designed by combining an optically tuneable liquid crystal layer with a dye sensitized solar cell. The liquid crystal layer switches between a clear and an opaque state depending on the incident sunlight. Different configuration types were evaluated including a liquid crystal cell placed directly below the DSSC (1), a liquid crystal layer stacked on top of the DSSC (2) and a liquid crystal layer and DSSC between crossed polarizers (3). Type 1 showed a J_{sc} of 16.43 mA cm⁻², V_{oc} of 0.744 V, a Fill Factor of 0.626 with overall efficiency of 7.936% under 100 mW cm⁻² at 1 sun conditions. Type 2 showed J_{sc} 2.13 mA cm⁻², V_{oc} 0.698 V, 0.739 Fill Factor, with an efficiency of 1.099%. Whilst type 3 showed a J_{sc} of 5.671 mA cm⁻², V_{oc} of 0.779 V, with a Fill Factor of 0.745 and efficiency of 3.248%. This indicates that in the transparent mode solar energy is collected, whereas in the opaque mode light is blocked resulting in user privacy and security with the transition between modes performed without any external power. Huang et al. [207] designed a device with a semi-transparent Si thin-film solar cell (Si-TFSC) substrate, an electrochromic solution and a transparent non-conductive substrate. The PV-Electrochromic device has two main functions: one operates as a PV cell module and the other as a self-powered smart glass. Upon receiving solar beams part of the energy produced by the device is converted into ionic current triggering

the colour change of the device, whilst the monolithically integrated Si-TFSC module produces energy to the connected load. The findings show that the photoelectric conversion for semi-transparent Si-TFSC sample photoelectric conversion layer (cathode) area of $5 \times 0.5 \text{ cm}^2$ were V_{oc} 0.93 V, J_{sc} 12.3 mA/cm², 73.23 % Fill Factor, P_{max} 20.94 mW and efficiency of 8.38%. Moreover, the device uses an anodic colouring *N,N',N,N'*-tetramethyl-*p*-phenylenediamine (TMPD) solution with a transmittance change ($\Delta T\%$) that was around 70% at 590 nm, with 200 seconds colouring time and device transparency restored when the sunlight declines. The external output switch layout coupled on the Si-TFSC can control the energy load produced and, connected to a DC/AC inverter or to a DC charge storage device, can store a direct current provided by the Si-TFSC module. Zhou et al. [208] reported a novel VO₂-based smart window combining energy generation and saving. This window offers the potential to intelligently regulate and utilize solar radiation efficiently by using light scattering to transport light to solar cells added to the glass panel for energy production as well as regulating infrared transmittance therefore maintaining visible transparency functioning as a thermochromic smart window. Three samples C_a, C_b and C_c were tested with a light conveyer surface made from a polycarbonate plate with refractive index of 1.59 to guide scattered light to poly-silicon solar cells. The low reflective index medium used was a VO₂ particle film on a quartz plate for C_a, VO₂-based power arrays for C_b and a VO₂ thin film for C_c. Results showed that C_a, C_b and C_c devices have efficiencies of 0.50%, 0.52% and 0.34%, V_{oc} values of 0.501 V, 0.498 V and 0.497, Fill Factor values of 50.18%, 59.68% and 52.06% and I_{sc} values of 2.0 mA/cm², 1.74 mA/cm² and 1.32 mA/cm², respectively. The higher efficiency and Fill Factor values of C_b as compared to C_a and C_c indicates that the structure of C_b is more efficient in the collection of scattered energy as compared to C_a and that C_c is the least efficient due to decreased scattering. A study from Guo et al. [209] presented a smart photovoltaic window design comprised of VO₂ nanoparticles in a thermotropic layer with an organic solar cell. This window generates electricity

utilising the visible part of the solar spectrum whilst response to ambient changes in temperature allows for smart control of NIR radiation entering the window. This device achieved a power conversion efficiency of 3.1%, having more than 7.5% solar module ability, whilst keeping visual transparency at 28.2%. Martina et al. [210] proposed a 12×17 cm² photoelectrochromic glass-on-glass module with four dye sensitized solar cells and a central electrochromic area in the same glass panel. This trifunctional glass combines a photo-electrochromic device with an organic light-emitting diode and an electronic control system. Additionally, a 10×8 cm² transparent white OLED was designed and clamped onto the back of the electrochromic module to affect the light emission. The energy is stored in supercapacitors, useful for inducing shading effects in the day or artificial lighting at night. The average efficiency of the four-dye sensitized solar cells modules section was 2.4% and the electrochromic section high was $\Delta T = 42\%$ close to 700 nm, whilst coloration efficiency and modulation in optical density ΔOD reached maximums of 1.17 and 73 cm² C⁻¹ respectively near to 1200 nm.

2.3.6 Smart windows summary

At this stage smart windows are supporting an excellent way to improve daylight, indoor and energy consumption in commercial and residential buildings. Due to the variety of technologies available in this field different issues can be solved or mitigated in different ways. Electrochromic, thermochromic, photovoltachromic lead the way to improve overall performance of the buildings. Nonetheless, some drawbacks can be found depending on which technology is used. Some of the issues include low efficiency, low transparency levels, long bleaching cycles between colours, electrical charge needed to control on/off modes, overproduction energy, material degradation, discoloration, and device life span. Table 2.7 shows the highlights of the smart window technologies and features.

Table 2.7. Highlights of smart window technologies and main features.

Smart window technology	Device description	Features	Power output	Transparency when activated	Ref.
Electrochromic	40mm x 40 mm PET layer and Polyaniline electrode with Si PV cells	Self-powered, energy storage	-	30%	[204]
Photo-voltachromic	20mm x 20mm window made of TiO ₂ , Pt, Pen/ITO and WO ₃	Self-powered	-	-	[205]
Electrochromic	55×5 cm ² Si thin-film solar cell substrate, an electrochromic solution, and a transparent non-conductive substrate	Control energy load and storage	20.94m W	-	[207]
Thermotropic	100 nm, 250 nm and 400 nm thickness VO ₂ films with an organic PV cell with an active area of 10.4 mm ²	NIR control	-	28.2 %	[209]
Photo-electrochromic	All-printed 12×17 cm ² module, with DSSC, electrochromic area and 10×8 cm ² organic LED	Lighting and dynamic shading control	18.85m W	30 %	[171]
Thermotropic	120 mm x 120 mm x of 6 mm double glazed window with HPC & Gellan gum membrane	No voltage required, daylight control and energy loads savings	57W	20 %	[200]

2.4 Summary.

This chapter provided an overview on the different smart window technologies and reviewed the most relevant studies and developments. The introduction of new technologies to achieve zero emission buildings has opened the door for the development of smart windows and BIPV. In the last decade, these technologies have evolved in different ways to suit the needs of the customers looking to compete with conventional solar panels. It was the intention of this paper to

provide a comprehensive review of these new and novel technologies from the working principles, the way they have evolved over time and the improvements that have been made to them. Overall, the features and constraints of low CPV presents an excellent opportunity for producing electricity from sunlight passing through windows. A wide variety of technologies offer diverse solutions for onsite problems to attain the goal of low energy buildings, from regular solar cells, luminescent solar concentrators, and smart windows for energy generation. It is important to highlight that thermotropic materials adapted to the 'smart windows' have a bright future in sustainable building design due to their multi-functional use assisting in cooling, heating, and lighting loads. Additionally, offering to control thermal energy and generating electricity, hence providing a promising solution for sustainable development.

After this comprehensive technologies and materials review is highlighted the opportunity to develop a novel smart window capable to promote practical solution to all the issues stated in this review. Thus, matching the research gap to continue with the study presented in this Ph.D. thesis. The next chapter will provide information on the materials and methods used for the development and testing.

Chapter 3

Methods & materials

This chapter provides details of the methodology followed to select the new polymers and the thermal and optical characterisation of the selected polymers and gelling agents in the thermotropic membrane. This chapter also details the ray tracing modelling and its validation, design, and fabrication of the smart window prototype for indoor testing with optical and electrical characterisation of the device and its components. Additionally, the experimental outdoor settings are detailed with a description of the experiment designs and experimental board fabrication for the smart window outdoor testing.

3.1 Building Integrated Concentrating PV (BICPV) “smart window”.

The working principle of the presented novel solar concentrator resides in the total internal reflection (TIR). The TIR process can be explained by Equation 1, where the critical angle θ_c , where n_1 is the refractive index of the air and n_2 is the refractive index of the glazing cover.

$$\theta_c = \sin^{-1} \frac{n_2}{n_1} \quad (1)$$

Thus, the sun rays that fulfil TIR conditions will be reaching the edges of the CPV and producing electricity via the Si cells mounted in there. TIR is depicted in Figure 3.1.

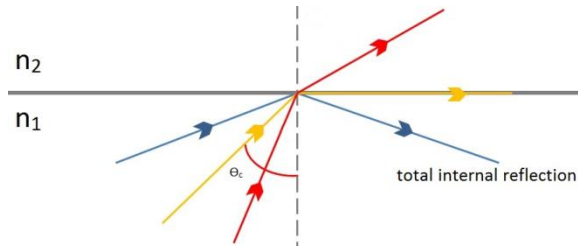


Figure 3.1 Total internal reflection concept.

This novel BICPV “smart window” consists of a thermotropic hydrogel polymer layer between two white optical glasses with solar cells attached to the edge of the glazing pane. When the glazing temperature is above the switching temperature, the thermotropic layer transitions to a translucent state, then the incident sunlight hitting the thermotropic layer will experience diffuse reflection. depending on the reflected angle of the light rays, some of them will fill the total internal reflection being trapped inside the glass reflecting toward the glass edge where the solar cells are mounted, thus producing electric energy as shown in Figure 3.1

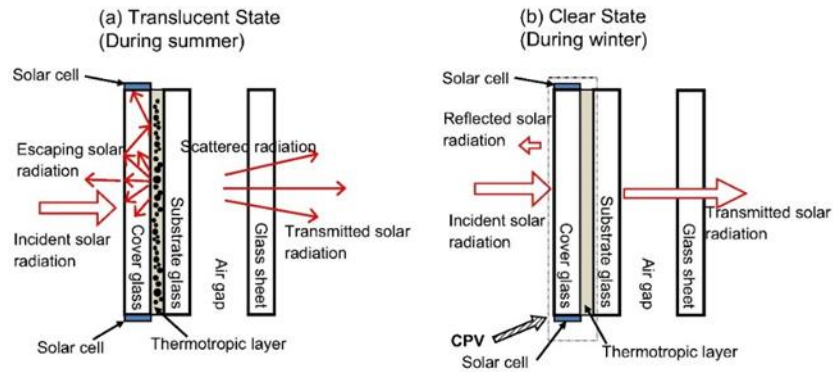


Figure 3.2 BICPV working principle (a) Translucent state, (b) Clear State [177].

The geometric concentration ratio of the smart window is calculated using Equation 2.

$$CRg = \frac{Aa}{Ar} \tag{2}$$

Where CR_g is the geometric concentration ratio, A_a is the area of the collector and A_r is the surface area of the receiver, hence the CR_g of the smart window prototype is 4.8X or 1.2X per side with a solar cell attached.

3.1.1 Material selection

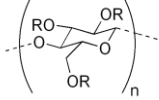
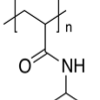
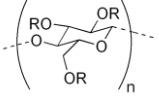
Aiming to broaden the scope of the smart window, research for new membrane materials was undertaken. This device uses a thermotropic membrane which initially was made with HPC, a phase changing polymer and GGF as a matrix or gelling agent. This polymer can be changed to find new features or different conditions than HPC, thus adding variations in the smart window configuration, making it more versatile to building integration. The materials that were considered suitable to be part of the smart window membrane in this research were required to have the following properties:

1. **Thermotropic:** capable of responding to a thermal stimulus.
2. **Polymer:** a cellulose derivative gel-based polymer that is water soluble so that hazardous material is avoided, and preparation costs is low.
3. **Adjustable Transition Phase:** the transition phase temperature of the material can be adjusted with the addition of salt; this provides the ability to tailor the material to preferential conditions.
4. **Optical Properties:** it must have high transmittance levels in a clear state, diffuse reflectivity, and a high reflective index to increase the probability of light capture by the edge-mounted solar cells.
5. **Eco-friendly:** The environmental impact of production must be minimised, and the potential for use to aid zero emission designed buildings should be maximised.

Following the last criteria, Hydroxypropyl cellulose (HPC), Poly(N-isopropylacrylamide) PNIPAM and Hydroxypropyl methyl cellulose (HPMC) were selected to be part of the new thermotropic membranes testing. Table 3.1 shows

the three materials showing with a tick and a cross if they matched or not, the sought features.

Table 3.1 Polymer structure and features.

Features	Materials		
	HPCM	PNIPAM	HPC
Structure	 $R = H \text{ or } CH_3 \text{ or } CH_2CH(OH)CH_3$	 $(C_6H_{11}NO)_n$	 $R = H \text{ or } CH_2CH(OH)CH_3$
Sol-gel transition	✓	✓	✓
Switching temp.	47-70°C[211, 212]	32°C[213]	~40°C[214, 215]
Water soluble / non-hazardous	✓	✓	✓
Adjustable transition	✓	✓	✓
Heavy environment impact	✗	✗	✗

Additionally, as a part of the smart window membrane, a matrix or gelling agent was used to keep the sample more homogeneously and retain water while the temperature increases. Thus, Gellan gum type F (GGF) was used as a gelling agent with similar environmental and safety selection parameters as had been used for the other materials. As a fermentation product of bacteria, gellan gum is a water-soluble polysaccharide. It has no thermo-reversibility and is optimal to be a matrix for smart windows membrane due to a large number of hydroxyl groups (OH) in its structure [201]. On the other hand, Ethyl hydroxyethyl cellulose soluble in water (Ethulose) was selected to add variations to the thermotropic membrane and determine whether the membrane's optical and thermal properties can be improved. Ethulose is a white granular solid that contains both ethyl and hydroxyethyl ether groups and is used as an emulsifier, stabilizer, thickener and film former in many types of solutions such as foods, cosmetics and paints [216]. Despite not offering a large group of hydroxyl, ethulose offsets this limitation with a more stable membrane due to the emulsifier, stabilizer properties [217]. Due to

the fact that the membrane does not stem from bacteria fermentation, higher transparency levels and a longer lifespan are obtained from cellulose via treatment with alkali, ethylene oxide, and ethyl chloride [218]. Therefore, ethulose was used as a matrix for the thermotropic membrane to expand further possibilities and variations for the smart window.

3.2 Samples preparation

The liquid HPC samples were prepared by heating distilled water at 60°C in a covered beaker and adding the HPC slowly until it was fully dissolved by magnetically stirring for a period of 12 hours. The HPMC and PNIPAM samples were prepared by magnetically stirring using distilled water at room temperature with a stirring period of 12 hours for full dissolution of the polymers. Regarding the gelling agents, on one hand, the GGF sample was prepared heating distilled water at 75° for 3-5 minutes then adding the GGF slowly until GGF was completely dissolved by magnetically stirring. On the other hand, Ethulose was prepared with distilled water at room temperature adding the Ethulose and mixed by magnetically stirring for 1 hour. Further details of the membrane synthesizing process can be found in the membrane manual for HPC and GGF listed in appendix A.

3.3 Samples characterization

Prior to commencing the smart window prototype testing the material samples' characterisation the material samples' characterisation was conducted to collect information on their thermal, optical, and physical properties. Thereby, Differential scanning calorimetry (DSC), The Fourier Transform Infra-red spectroscopy (FTIRs), Environmental scanning electron microscopy (ESEM), UV-VIS spectroscopy and long-lasting test were performed on liquid and membrane samples.

3.3.1 Micro DSC Test

Differential scanning calorimetry is a technique to measure thermal properties of the samples to determine the relationship of physical properties of the samples across a temperature range providing the enthalpy associated with this process. In other words, DSC provides the thermal analysis to determine the temperature and heat flow related to the transitioning process of the samples. This analysis is done in the function of time and temperature, measuring heat quantity absorbed or radiated by the sample on the basis of the temperature difference between the sample and the reference material [30, 219, 220]. In Figure 3.3 the internal diagram of a DSC components can be seen showing the reference and sample pans, heat sink, thermocouples, heat resistors and the data collected flow diagram.

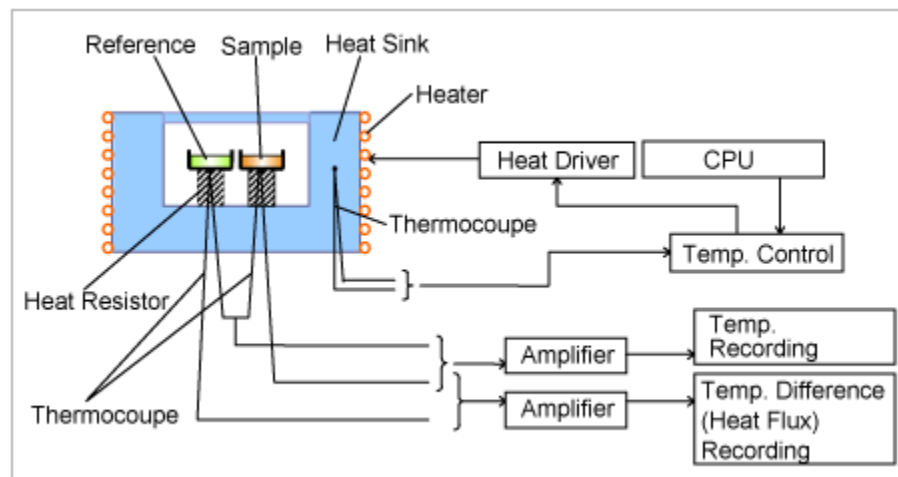


Figure 3.3 DSC components and data collection flow.

Micro DSC offers a controlled environment where endothermic and exothermic reactions are recorded and examined in a more sensitive way to explain the thermal behaviour of the sample compared to the DSC, providing a subtler approach of the physical change inside the samples. Therefore, the Micro DSC test was used to determine how and when the phase change occurs in the selected materials and how the addition of water and gelling agent s used to blend the aqueous sample affects the phase change in the materials. Furthermore, it offers

valuable information regarding hysteresis in the samples tested due to the heating and cooling cycles in the DSC testing. According to the heat capacity of the material, it is possible to determine after which temperature further changes in the sample will not occur, thus selecting the temperature range for further testing.

In the curve interpretation, the maximum height of the transition (maximum heat capacity) (T_m) occurs at the phase transition when the material has a symmetrical curve. The width of the curve is the enthalpy (ΔH), and the beginning and end of the transition are determined by the lower (T_s) and upper boundaries (T_L)[221-223]. The latter explanation is illustrated with the graph in Figure 3.4.

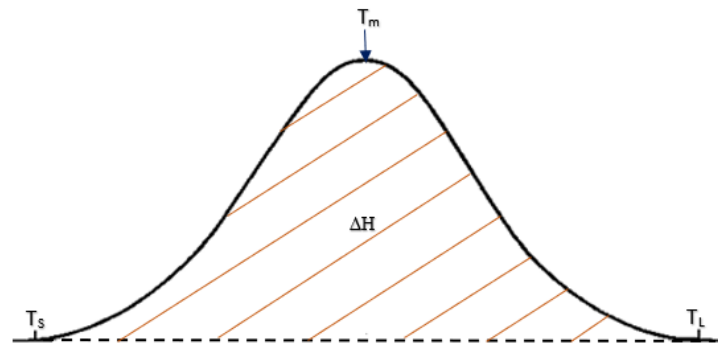


Figure 3.4 ΔH , T_m , T_s and T_L describe under the DSC endotherm curve.

Setaram High sensitivity micro-DSC (III) was used to perform differential scanning calorimetry (DSC) tests on the samples. Due to the high sensitivity and precision in phase transition materials for this test, one liquid HPC and two membranes were used. The liquid sample was used as a reference to match the phase changing temperature with results previously revised on the literature review and to determine the effect of water on HPC. The membrane samples were compared against the liquid sample, and the effect of the gelling agents on these membranes was examined. Liquid and membrane samples were tested over a temperature range from 20-80°C. Details of the concentrations and samples are shown in Table 3.2.

Table 3.2 showing DSC samples concentrations.

<i>Sample</i>	<i>Concentration</i>
<i>Liquid HPC</i>	2 wt. % & 6 wt. %
<i>Membrane HPC & GGF</i>	2 wt. % & 2 wt. %
	6 wt. % & 2 wt. %
<i>Membrane HPC & ethulose</i>	6 wt. % & 1.5 wt. %
	6 wt. % & 0.5 wt. %
	6 wt. % & 1.5 wt. %

3.3.2 FTIRs test

The Fourier Transform Infra-red spectroscopy is a test that uses a mathematical process (Fourier transform) to translate the raw data (interferogram) to the actual spectrum recording. The ' vibrational spectrum is used as a fingerprint to determine the samples' qualitative aspect deducing backbones and functional groups present there [224]. FTIR analysis identifies organic, inorganic, and polymeric materials using infrared light to scan the samples. Any variations in the absorption bands pattern indicate a change in the material composition, being useful in identifying and characterizing unknown materials, detecting contaminants, finding additives, and identifying decomposition and oxidation [225]. Details of the process inside of the FTIRs device are shown in Figure 3.5.

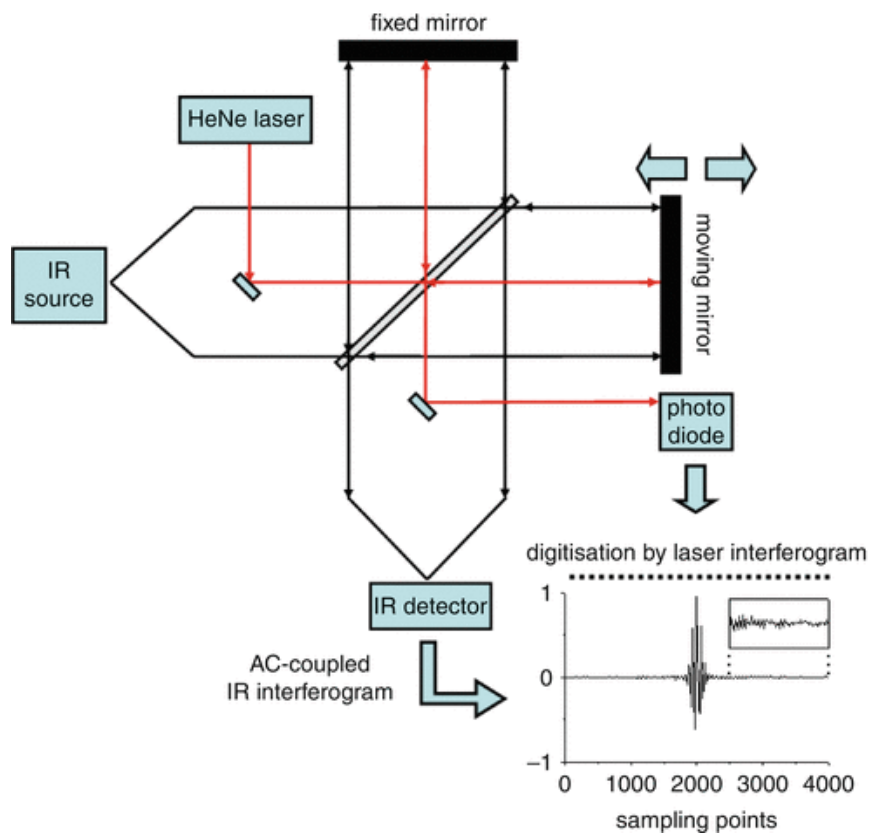


Figure 3.5 FTIRs components diagram.

FTIRs were utilised to determine how the samples respond to the infrared spectrum absorbing heat from incoming sunlight and how this will impact the smart window temperature, electrical performance, and heat gains inside the building, with this complementing what cannot be tested in the DSC test. A Bruker Tensor 27 FT-IR & OPUS Data Collection Program equipped with a room temperature DTGS detector, mid-IR source (4000 to 400 cm^{-1}), and a KBr beam splitter was used to test the samples under the IR spectrum with a maximum resolution of 1 cm^{-1} . One HPC liquid and two membrane samples were used for this test. The liquid sample was done to obtain a reference about the liquid HPC sample behaviour through the absorption bands of the IR spectrum, and the membrane samples were used to cross-compare changes in the absorption bands of the samples due to the addition of the different gelling agents. Details of the liquid and membrane samples are shown in Table 3.3.

Table 3.3 FTIRs samples concentrations.

<i>Sample</i>	<i>Concentration</i>
<i>Liquid HPC</i>	6 wt. %
<i>Membrane HPC & GGF</i>	6 wt. % & 1.5wt.%
<i>Membrane HPC & Ethulose</i>	6 wt. % & 1.5 wt. %

3.3.3 Environmental electron scanning microscopy.

An environmental scanning electron microscope is a device with which uncoated biological and industrial materials can be examined using an electron beam in a high chamber pressure atmosphere filled with water vapour. Specimens can be analysed using ESEM without destruction and additional specimen preparation procedures. Dynamic experiments are also possible in the ESEM, such as drying or crystallization. A complementary diagram to the latter explanation is shown in Figure 3.6.

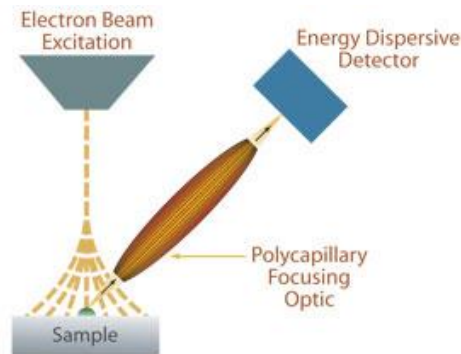


Figure 3.6 ESEM components.

In order to explore the homogeneity level of the membrane blend at a molecular level, HPC, HPMC, PNIPAM with GGF membranes and HPC with ethulose membrane ESEM pictures were required. Thereby cross-comparing the results observed in the sample pictures it is possible to determine if the chemical blend is optimal at this level. Table 3.4 shows the membrane concentrations for the ESEM pictures.

Table 3.4 ESEM pictures of membrane concentrations.

<i>Sample</i>	<i>Concentration</i>
<i>Membrane HPC & GGF</i>	6 wt. % & 1.5wt.%
<i>Membrane HPMC & GGF</i>	6 wt. % & 1.5wt.%
<i>Membrane PNIPAM & GGF</i>	6 wt. % & 1.5wt.%
<i>Membrane HPC & Ethulose</i>	6 wt. % & 1.5 wt. %

The ESEM device FEI Quanta 650 SEM was used to take the membrane samples pictures. This device can generate high -resolution images of uncoated or hydrated samples. The samples were held on the SEM at 3°C from 4.27-5.8 Torr and with a 95% humidity level to keep the samples hydrated during the analysis. Two distances for the imaging process were selected, 100 µm and 50 µm using a 10kV acceleration voltage. Unfortunately, the ESEM pictures can only be taken in the clear state of the sample. Due to the nature of the device, it is impossible to heat the sample while it is being scanned.

3.3.4 Long-lasting prototype window test

Since the building components are exposed and affected by dynamic environments (indoor and outdoor) a long-lasting indoor test was performed to determine the membrane samples capacities to retain water when the membrane is exposed to an indoor environment. Two smart window prototypes consisting of two different membranes and a ~0.7mm spacer between two 50 x 50 x 4 mm optical white low iron glass panes were manufactured. Membrane concentrations for the tested smart windows are shown in table 3.5.

Table 3.5 Long-lasting test sample concentrations.

<i>Sample</i>	<i>Concentration</i>
<i>Membrane HPC & GGF</i>	6 wt. % & 1.5wt.%
<i>Membrane HPC & Ethulose</i>	6 wt. % & 1.5 wt. %

During the long-lasting test, the smart window prototypes were tested over four weeks under indoor conditions of 25°C temperature controlled by an air conditioning system inside the energy Technologies building lab A4 at the University of Nottingham. These prototypes were left inside the lab to determine the gelling agents' performance when exposed to the indoor environment without sealant.

3.3.5 UV-VIS spectroscopy

The optical characteristics of the liquid samples have been tested through the UV-VIS spectroscopy using an Ocean Optics Spectrometer 2000+UV-VIS-ES, a Q-Pod for temperature control with its 1 x 1cm quartz cuvette and a HL-2000 Ocean optics as a light source. The temperatures range used was based on preliminary DSC tests on the HPC samples, only adding 10 °C more to the HPMC test because its transition phase requires more heating. Details on the temperature range can be seen in table 3.6.

Table 3.6 Temperature range for the selected polymers.

<i>Polymer</i>	<i>Temperature range</i>
<i>HPC</i>	20 °C to 55 °C
<i>HPMC</i>	20 °C to 65 °C
<i>PNIPAM</i>	20 °C to 55 °C

During the transmittance test in liquid state, measurements were taken at intervals of 5°C within the polymer's temperature range, waiting 20 minutes between each measurement to stabilize the membrane. These experiments were reproduced three times for each sample, and the procedure was performed during heating and cooling, aiming to find effects on thermotropic transmittance in liquid samples. The cuvette was filled with distilled water to be used as a reference for transmittance levels. The switching point was defined by the temperature at which the phase changing of the polymer sample occurs hence transitioning from clear state to light scattering. The transmittance test was conducted with the methods

outlined in BSI Standards BS EN 410:2011 [226], which is commonly used to calculate average visible light transmittance in the wavelength range 430–780 nm. Following the methodology from the previous work by Connelly et al. [201] and comparing the data for visible light transmittance, 600 nm transmittance and direct solar transmittance, it was found that there were slight differences in transmittance values both below and above the switching point. Therefore, to fit the purpose of this research, a wavelength of 600 nm was selected

A prototype of a thermotropic window was manufactured, casting the membrane made of the selected polymer with GGF on to a ~0.7mm spacer suspended between two 50 x 50 x 4 mm of optical white low iron glass panes. Three replica samples of every polymer and concentrations were made and tested to get accurate results. Reflectance and transmittance tests were performed by placing the prototype window on a hotplate with four thermocouples attached to monitor the temperature changes across the sample. Pictures depicted in Figure 3.7 shows the details of the setup.

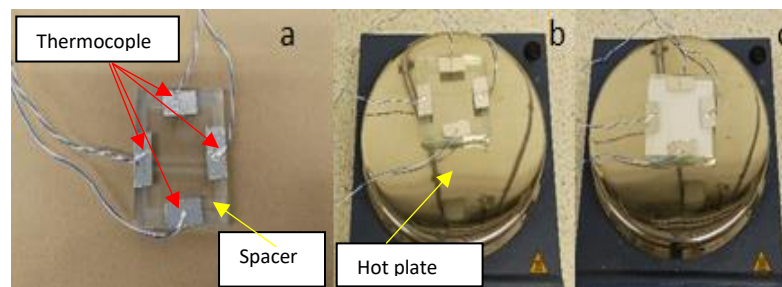


Figure 3.7 (a) Illustrating the positions of the thermocouples at the window sample, (b) smart window prototype in clear state at room temperature at the hot plate (c) smart window prototype in light scattering state.

Measurements were taken every 20 minutes, using the integrating sphere FOIS 1 from Ocean Optics, for transmittance, and ISP-REF Integrating Sphere for reflectance testing. The same light source and spectrometer used in the previous liquid test were employed for this test. A single layer glazing was used as a reference for transmittance and reflectance. Liquid and membrane samples concentrations selected for these experiments are shown in table 3.7.

Table 3.7 selected concentrations for liquid UV-VIS samples concentrations.

<i>Polymers</i>	
HPC	
<i>Liquid</i>	2 wt. %, 4 wt. % and 6 wt. %
<i>Membrane</i>	2 wt. % & 1., 4 wt. % & 1.5wt. % GGF and 6 wt. % & 1.5wt. % GGF
HPMC	
<i>Liquid</i>	2 wt. %, 4 wt. % and 6 wt. %
<i>Membrane</i>	2 wt. % & 1.5wt. % GGF, 4 wt. % & 1.5wt. % GGF and 6 wt. % & 1.5wt. % GGF
PNIPAM	
<i>Liquid</i>	2 wt. %, 4 wt. % and 6 wt. %
<i>Membrane</i>	2 wt. % & 1.5wt. % GGF, 4 wt. % & 1.5wt. % GGF and 6 wt. % & 1.5wt. % GGF

Ethulose was used as a secondary gelling agent to be compared against GGF selecting the same conditions as before in the GGF membrane experiments. Details of sample concentrations of ethulose membrane are shown in table 3.8.

Table 3.8 selected concentrations for gelling agent comparison.

<i>Gelling agent</i>	<i>Sample Concentration</i>
<i>GGF</i>	6 wt. % & 1.5 wt. %
<i>Ethulose</i>	6 wt. % & 0.25 wt. %
	6 wt. % & 0.5 wt. %
	6 wt. % & 1.5 wt. %

AlfaEsar and Sigma Aldrich provided the polymers. Ethulose was obtained from Talas, Azko Nobel and the GGF by Special Ingredients LTD, without any further purification or processing.

3.4 Lab instruments and experimental settings characterisation

After completing liquid and membrane samples characterisation and ray tracing, it was proceeded to determine the experimental settings for indoor testing and the lab instruments and smart window components characterisation. A 200W tungsten lamp was used as a light source for indoor experiments. A cosine corrector CC-3-UV-S with a wavelength range of 200-2500nm from Ocean Optics

was used to collect the absolute irradiance of the incident light from the lamp. Additionally, an ocean optics spectrometer USB2000+UV -VIS-ES with a 200-850 nm wavelength range was used to measure the irradiance. A Kipp & zonen CMP11 pyranometer with a spectral range of 285 to 2800 nm was used to verify the accuracy of the irradiance against the cosine corrector. I-V measurements were done using a Keithley 2420 source meter. Temperature readings were recorded using a Datalogger with five thermocouples, two in the front cover glass, two in the back and one between the glass panes to measure the membrane temperature directly. Figure 3.8 displays the experimental rig used for the smart window indoor characterisation.

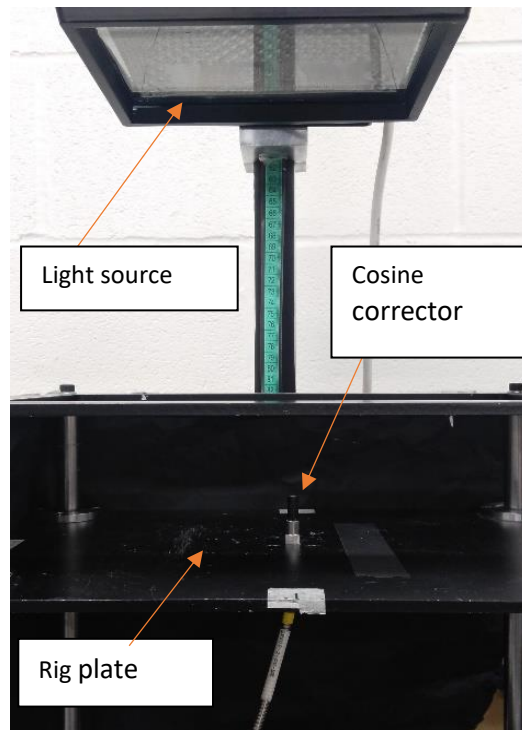


Figure 3.8 Experimental rig for indoor testing.

An important aspect of this experiment is the uniformity of the light source. Light uniformity will have an important impact on the optical and electrical characterization results of the smart window; therefore, it must be evaluated. The uniformity test of the light source was done using the cosine corrector, which was centred at the rig plate to calculate the absolute irradiance. Different heights were set between the lamp and the device to achieve low, mid, and high irradiance

levels at 170 W/m^2 , 400 W/m^2 , and 700 W/m^2 . A total of 44 squares of 2 cm^2 each were measured across the rig plate. Corner squares were avoided for the measurement because they cannot reach a proper illumination, due to the round borders of the pillars holding the rig plate structure. The centre of the plate was used as a reference for the X & Y axis. Details of this explanation are illustrated in Figure 3.9.

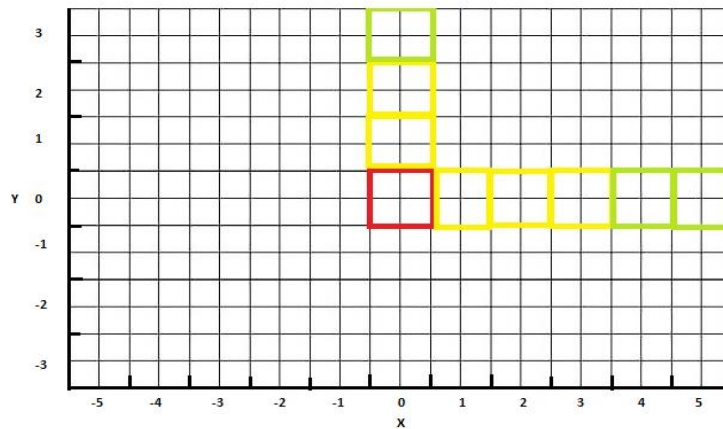


Figure 3.9 Uniformity of light source grid.

Accordingly, as part of the calibration process to achieve the best performance of the equipment for this testing, the irradiance levels were plotted with contour maps to understand how light uniformity was distributed over the rig plate. Values for low, mid, and high irradiation levels are presented in table 3.9. Figure 3.10 shows the contour map of low, mid, and high irradiance levels light distribution on the rig plate. The differences in the values are expected as they move away from the centre where the absolute irradiance is calculated firstly. This can be explained by to the non-uniform illumination from the light source. Moreover, it was found that the higher the irradiation level, the lower the uniformity of the light source, thus low and mid values are more likely to be close to the absolute irradiance centre reference point. The values on the light distribution contour map provide an average value accordingly with the colour presented, showing the areas where

irradiation was more uniform, thus presenting the best areas in the rig plate to get a uniform phase change in the smart window when indoor testing is performed.

Table 3.9 Calculated average values for the experimental rig plate.

Irradiance	Rig plate area		
	low	mid	High
Average value	165.20 W/m ²	363.54 W/m ²	565.09 W/m ²

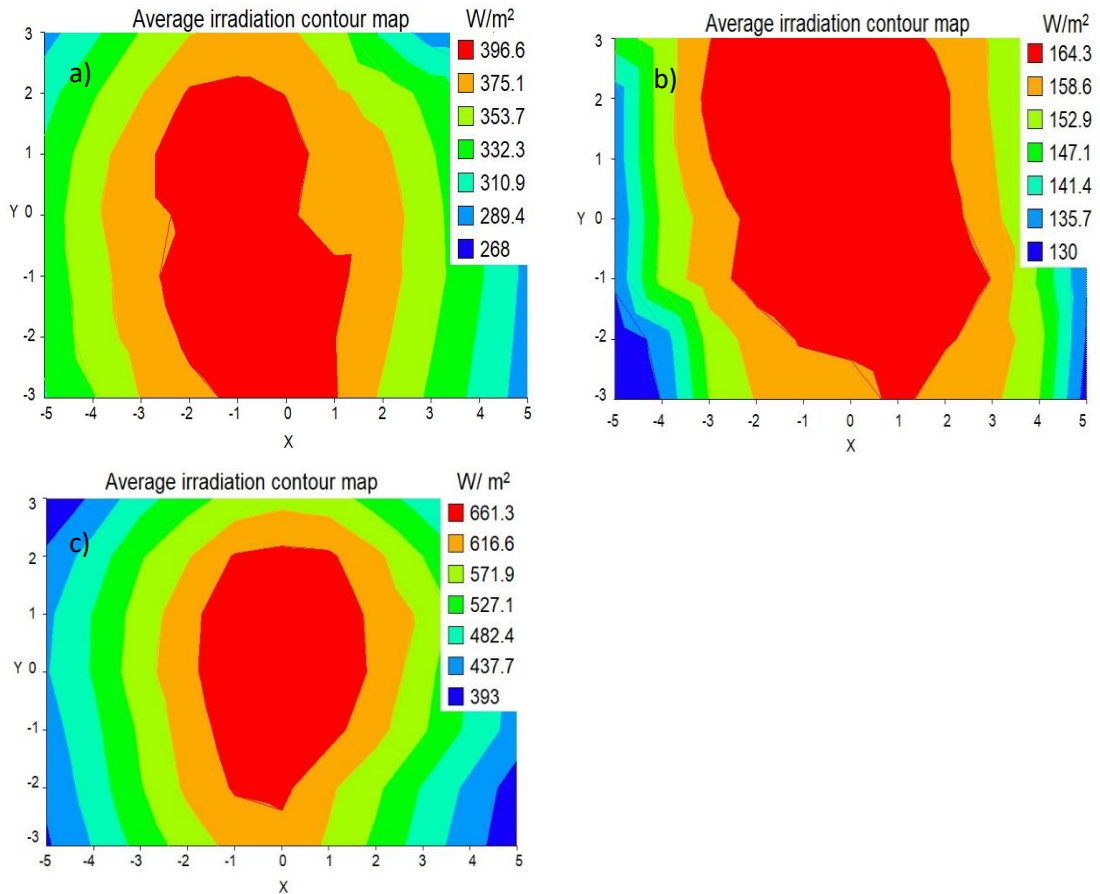


Figure 3.10. Light distribution contour maps, (a) low irradiation 170 W/ m², (b) mid irradiation 400 W/ m², (c) high irradiation 700 W/ m².

Additionally, the smart window area, which is 116x116 mm², must be characterized inside the contour map to assure that experimental testing is the closest to the correct irradiation. Unlike the simple light distribution test, in smart window area, variations in irradiation level are less; however, to assure that the irradiance level is correct, an offsetting must be done to pair the irradiance levels

closer with the desired value and get further results correctly. To achieve this 410 W/m² and 745 W/m² were used instead of 400 W/m² and 700W/m² to get similar average values and proceed with experimental work. Examples of the latter can be seen in Table 3.10 and Figure 3.11.

Table 3.10 Calculated average values for a smart window area.

Smart window area			
Irradiance	low	mid	high
Average value	165.20 W/m ²	384.28 W/m ²	618.46 W/m ²

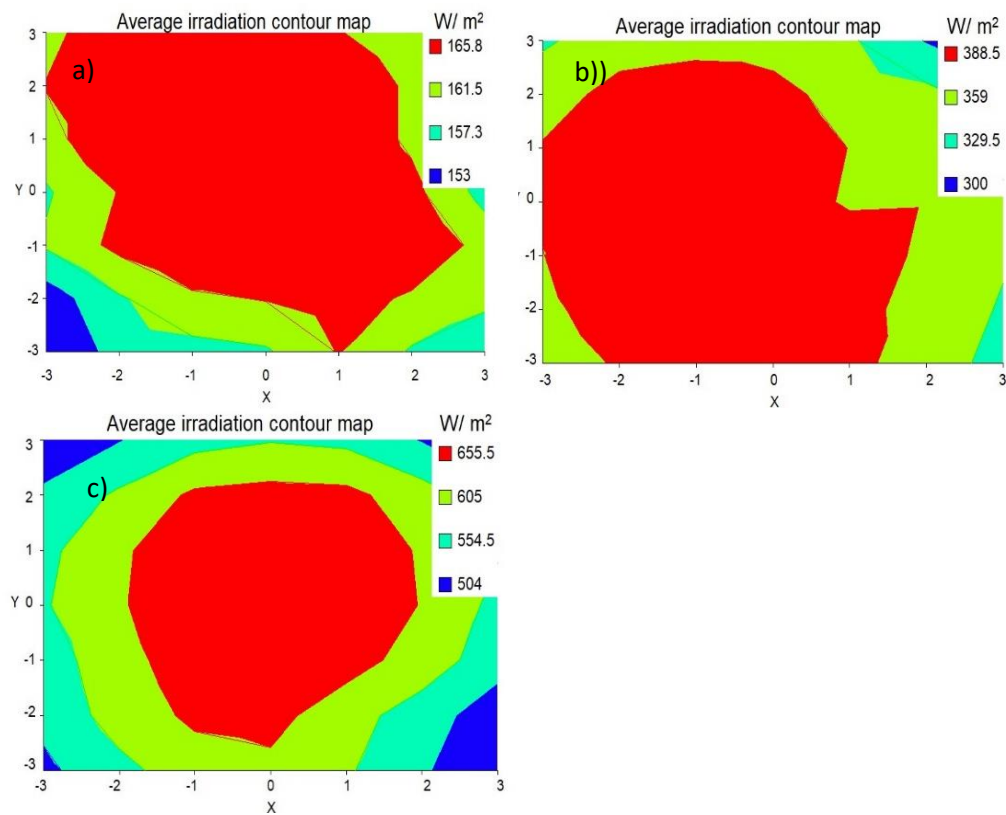


Figure 3.11 Smart window area contour maps. (a) low irradiation 170 W/ m², mid irradiation 400 W/ m², (c) high irradiation 700 W/ m².

Additionally, to the light distribution test, the Kipp & zonen CMP11 pyranometer was used to measure the irradiance. The centre of the rig plate was used as reference, which was the same as the absolute irradiance measurement done with the cosine corrector. This additional test was performed to know how the light distributes on average inside the rig. This test was needed because the

pyranometer has a wider range than the cosine corrector, which is a single point, thus understanding the rig plate's light distribution and irradiance levels. In this way, it can be seen that the closest of the selected levels to the standard conditions irradiance for PV cells for testing is the high level (700 W/m²) with an average value of 1092 W/m² recorded by the pyranometer. The latter explanation is summarized in Table 3.11.

Table 3.11 Cosine corrector versus pyranometer.

Absolute irradiance (W/m ²)	Pyranometer (W/m ²)
170	295.7
400	515.4
700	1092.7

3.5 Smart window design and characterisation

3.5.1 Single PV cell characterisation

To begin with the smart window components characterization, two PV cells were characterized as part of different prototype experiments, one for white-diffuse reflector-based window prototype and the other for the thermotropic window prototype. The irradiance level used for I-V characterization of the solar cells was 700W/m² at lab indoor temperature in each Saturn PV cell with crossbars and two thermocouples attached. Details of the testing can be seen in Figure 3.12.

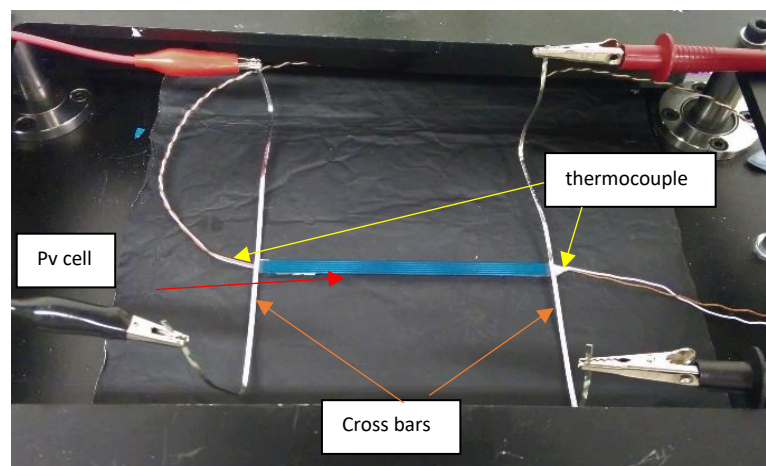


Figure 3.12 PV single cell indoor characterisation.

3.5.2 Smart window components

Once the single PV cell has been tested and characterised, it was proceeded to make the smart window prototype with the integrated PV cell. Optical white low iron glass size 116 x 116 x 6 mm with a spacer of ~0.7 mm between the glass panes were used. The solar cells used were Saturn PV cells with dimensions of 116mm x 6 mm manufactured by an electrolytic copper-plating process with a reported efficiency of 16% [227]. In Figure 3.13, the PV cell with the Crossbars attached, ready to be part of the smart window, is shown.

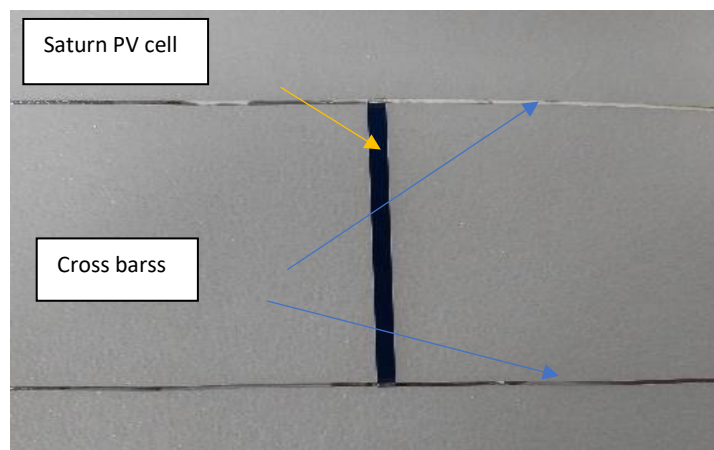


Figure 3.13 Saturn PV cell ready to be attached to the smart window.

Crossbars were provided by ULbrich of Austria GmbH, having a width of 1.3-2.5 mm +/- 0.08 and thickness: ≤ 0.20 mm +/- 0.008 with a Basemat Cu-ETP1. A reflective material White Optics 97[®], with 97% average reflectivity, was used as a reflective layer, and Dow Corning 1-2577 conformal coating material was used to optically bound the solar cells and the reflective material to the glass surfaces. The thermotropic membrane was made with HPC and GGF following the sample preparation criteria mentioned earlier in this chapter at section 3.2. The Figure 3.14 displays the smart window prototype ready to be tested with the PV cells attached and the thermotropic membrane in the clear state.

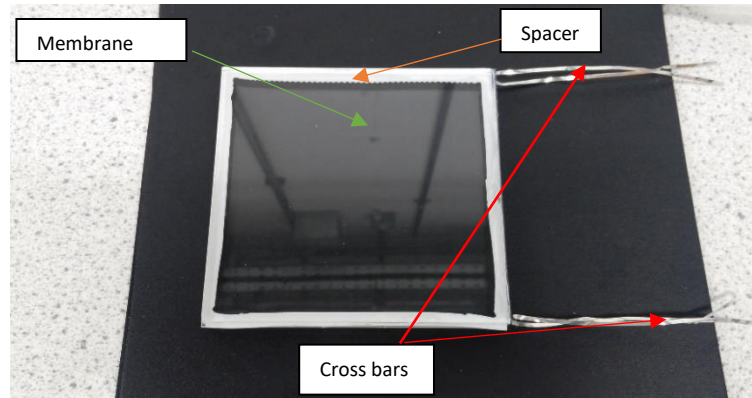


Figure 3.14 Smart window prototype ready to be indoor characterised.

3.5.3 Smart window with reflective layer attached.

For the smart window characterization, it was very important to test the smart window concept as a solar concentrator. Thereby, validating that the working principle of the smart window is working as expected. Therefore, a single PV cell's performance was compared against the smart window prototype with a 97% reflectivity layer attached. The PV cell and the reflective material white optics 97 were optically bounded to the optical glass using the Dow Corning 1-2577 conformal electrical coating material under pressure and left to cure at room temperature for 72 hours before testing. Whereby producing a highly reflective uniform layer inside the smart window prototype to test how the device is performing through the total internal reflection inside the glass and producing energy. Details of this smart window configuration can be seen in Figure 3.15.

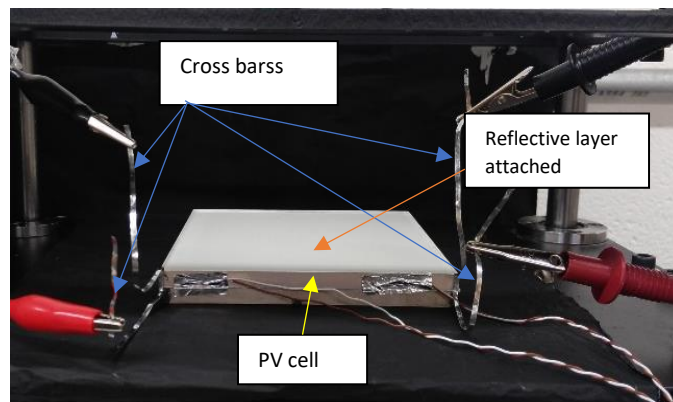


Figure 3.15. Smart window prototype settings on the experimental rig.

3.6 Ray tracing modelling approach

Ray tracing simulation as a counter part of solar concentrator tests was done. Aiming to match results and proceed to prototype testing with reliable data. Therefore, non-sequential ray tracing was selected because it permits the modelled light rays to intersect objects or surfaces regardless of sequence and repetition times. Thus it is suitable to investigate light diffused by total internal reflection (TIR), diffuse surfaces and global light collected by absorbers (solar cells) [228, 229]. During the simulation, the rays launched may hit a surface or an object in its way; this will produce reflection, refraction, or scattering according to the object properties. Additionally, the rays will be tracked until they cannot reach the next object. According to the smart window working principle, the device can switch from a clear state to a light scattering state when the switching temperature is achieved, thus producing Lambertian type diffuse reflections where the reflected rays take a random direction. Nevertheless, not every single ray can be split into several rays, a condition which would represent true Lambertian reflection of the thermotropic layer, therefore this drawback is compensated using a vast amount of rays [200].

3.6.1 Model description

The designed 3D ray tracing model generated according to the smart window specifications and parts, which comprises two 116 mm x 116 mm optical glass panes, a 116 mm x 6 mm mono facial Saturn solar cell and the white optics 97 reflector, which has 97% of reflectivity. The PV cells and reflector layer are attached to the glass with no air gap between them. The optical properties of the smart window components were measured previously and defined accordingly within the software environment aiming to obtain the best results. It is also important to note that in the simulation setting, rays will escape from the front cover when they cannot fill critical angles Θ_c expressed in equation 3.

$$\Theta_c = \sin^{-1} \frac{n_1}{n_2} \quad (3)$$

Where n_1 represents the refractive index of air and n_2 the refractive index of the glazing cover. The rest of the simulated rays that satisfy the TIR will be trapped inside the glass until they reach the solar cells at the glass edge. The geometric concentration ratio of the smart window is calculated using equation 4.

$$CR_g = \frac{A_a}{A_r} \quad (4)$$

Where CR_g is the geometric concentration ratio, A_a is the area of the collector and A_r is the surface area of the receiver, hence the CR_g of the smart window prototype is 4.8X or 1.2X per side with solar cell attached. Another key factor in solar concentrators is the effective concentration ratio (C_e), defined by the number of rays reaching the solar cell at the exit absorber after concentration. This can be represented by Equation 5 where C_g is the geometric concentration ratio, and η_o is the optical efficiency on the solar concentrator[200].

$$C_e = C_g \times \eta_o \quad (5)$$

Regarding the light source, the radiation intensity used to conduct the simulation was 700 W/m^2 with 1,000,000 rays perpendicular launched to the smart window front cover at a single wavelength of $0.54 \mu\text{m}$. In Figure 3.116 (a) the ray tracing model for the smart window with its axis and grid source can be seen and (b) shows the path of light rays tracked after the simulation.

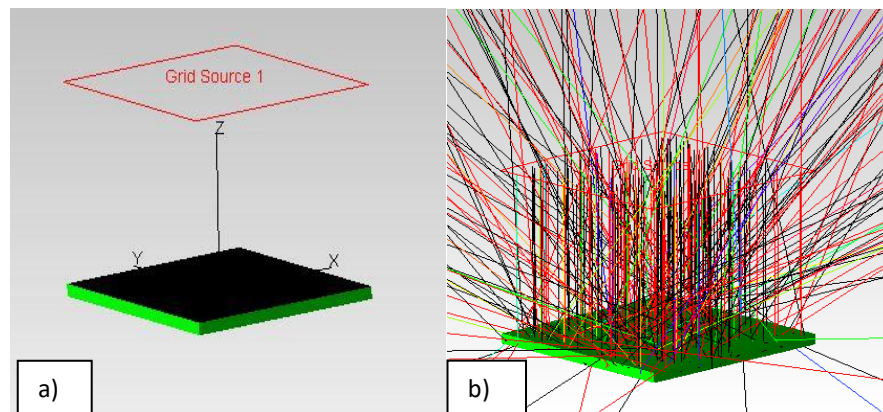


Figure 3.16 Ray tracing model design (a) & (b) light rays tracked by the simulation.

3.7 Smart window prototype indoor test settings

Before starting the smart window indoor testing, the device's concept was proven, and the ray tracing validation was done. The smart window with a thermotropic membrane was tested to examine the device's optical, thermal, and electrical performance when switching between transparent and light-scattering states, namely, in a dynamic environment. I-V curve measurements, power curves tests and correlation tests between MPP and transmittance were done using 2 wt. % HPC & 1.5 wt. % GGF and 6 wt. % HPC & 1.5 wt. % GGF membranes at $400\text{W}/\text{m}^2$ and $700\text{W}/\text{m}^2$. For these tests, the thermocouples distribution was the following: One inside of the prototype window to get the temperature measurements of the membrane, two more were attached to the smart window prototype on the top glass and bottom glass, and two more at the PV cell. Additionally, the cosine corrector was placed in the centre of the rig plate just behind the smart window to record the transmittance variations across the experiments. The locations of the thermocouples and cosine corrector can be seen in Figure 3.17. Furthermore, it is important to note that $170\text{W}/\text{m}^2$ was not used as irradiance level from the three selected irradiance levels due to the fact that not enough heat was produced at this level to achieve the phase change in the smart window prototype.

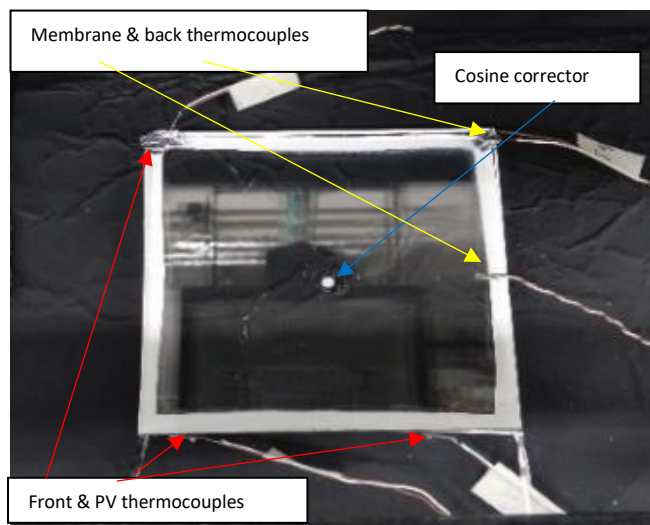


Figure 3.17. Thermocouple distribution and cosine corrector positioning on the back of the smart window prototype.

3.8 Outdoor testing experimental settings

After completing the smart window characterisation and prior to the smart window prototype outdoor testing, the experimental design was done. For the outdoor experiments of the smart window summer sunny days were chosen at a south-facing location at ground level outside the Energy Technologies Building Nottingham, U.K., where no buildings interfere with the sun path across the day. In order to perform the outdoor testing, an experimental board was manufactured with two window holders for the smart window, one for the reference window and another for the smart window. Three Kipp & zonen CMP11 pyranometers with a spectral range of 285 to 2800 nm were installed on the board, two behind the reference (Pr) and smart window (Ps), and the third one on top of the façade board (Pt). Moreover, two thermocouples were attached to the smart window (Ts) and reference window (Tr) front covers, with two additional sensors at the back of smart window PV cell (TPVs), reference window PV (TPVr) and one in the middle of the board (Tb) to measure ambient temperature. A Datalogger was used to retrieve the collected data. Details can be seen in Figure 3.18 and 3.19.

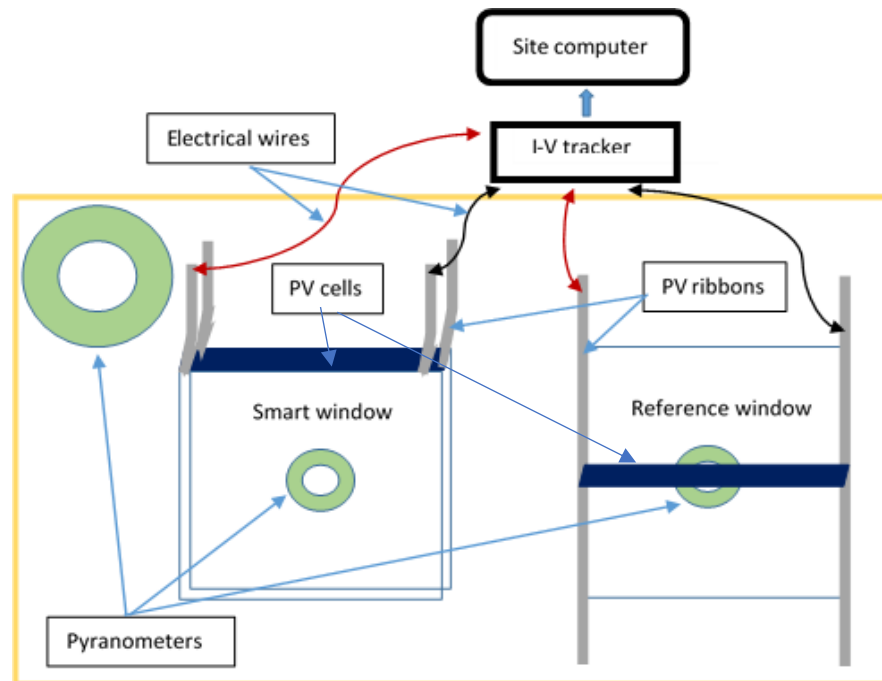


Figure 3.18. Experimental board components and settings.

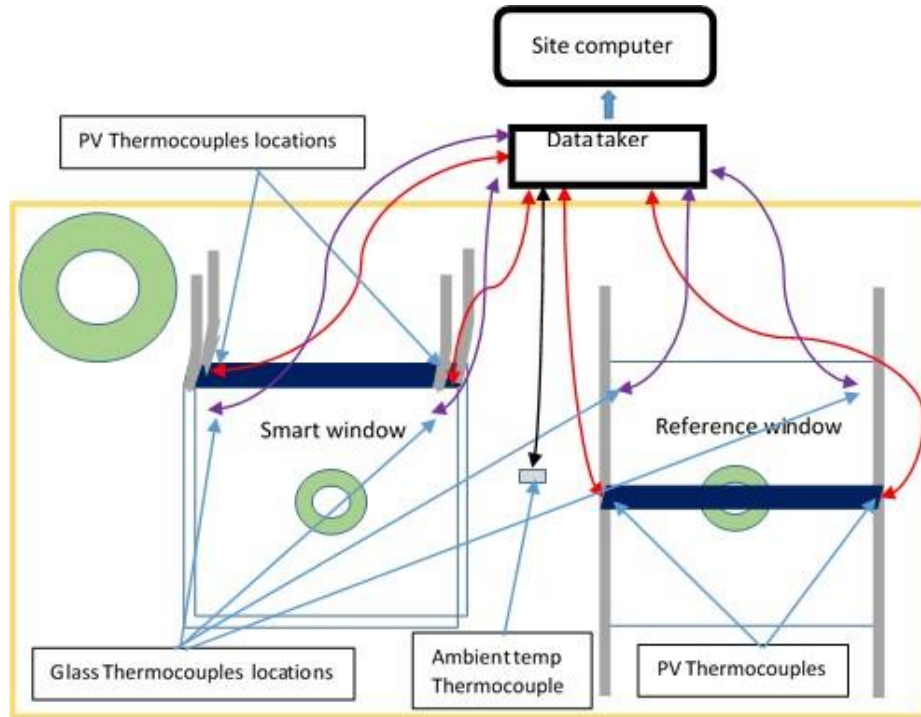


Figure 3.19. Experimental board thermocouple's locations diagram.

The PV cell efficiency was calculated in all outdoor experiments using the equation (6).

$$\eta = \frac{MPP}{I * A_{pv}}$$

Where η is efficiency, MPP is maximum power point, I is irradiance level and A_{pv} is the PV cell area. The nomenclature for the smart window PV cell efficiency was η_{PVs} and η_{PVr} for the reference window. The electrical power output measurements were done using a Keithley 2420 source meter with a programming sequence to take measurement each 2 min for a period of 7 hours using the front and the rear part of the source meter with four cables each. Besides, the cable length used for this experiment was tested previously in the lab to avoid any energy loss length related problems during outdoor testing.

The outdoor experiments were performed from 9:30 to 17:30 on the 29th and 31st of August and 1st of September. During the experiment, the samples were facing south at 30°, 60° and 90° of inclination, respectively. The three angles were

selected to understand the smart window performance not only as a building window but as a skylight, roof or envelop of a building. Details of the latter explanation are shown in Figure 3.20.

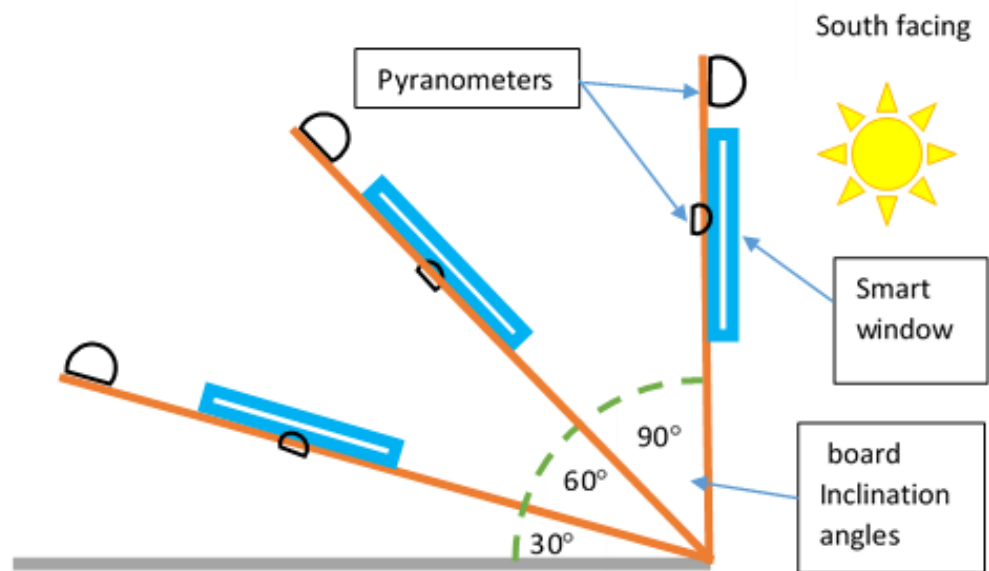


Figure 3.20. Experimental board positioned at three different inclination angles for outdoor testing.

3.9 Outdoor smart window prototype

The smart window was made of two optical white low iron glasses measuring 116 x 116 x 6 mm with a ~7 mm spacer between the glass panes, and a 6 wt. % HPC & 1.5 wt. % GGF membrane. HPC and GGF were provided by Sigma Aldrich and GGF by Special ingredients LTD, respectively, without any further purification or any other process added to them. The solar cells used were Saturn PV cells with dimensions of 116mm x 6 mm. Crossbars were provided by ULbrich of Austria GmbH having a width of 1.3-2.5 mm +/- 0.08 and thickness: ≤ 0.20 mm +/- 0.008 with a Basemat Cu-ETP1. Dow Corning 1-2577 conformal coating material was used to optically bound the solar cells to the glass surfaces. The window edges were sealed with silicon. Figure 3.21 (a) displays the smart window prototype mounted on the experimental board in clear state showing high transparency level

and (b) show the same sample in the light scattering state with all the membrane inside the glass turned into opaque white.

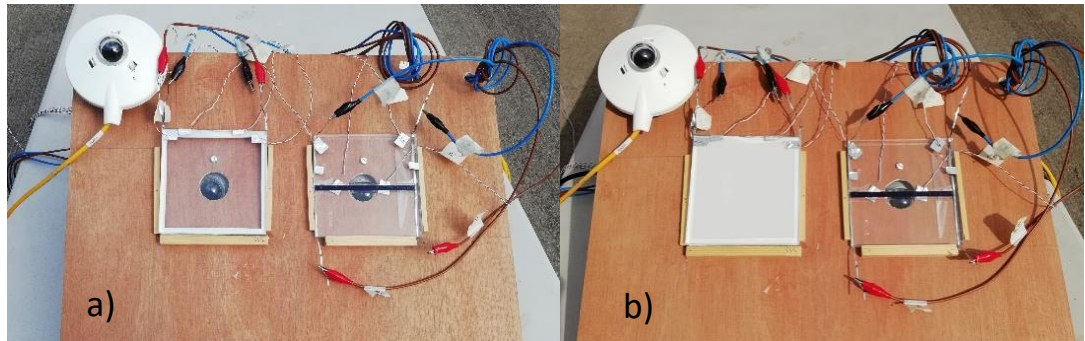


Figure 3.21. The Experimental board (a) smart window at clear state (b) at light scattering state.

3.10 Summary

Different materials, membrane blending methods and characterisation processes were described in this chapter, aiming to design and develop a novel “smart window” for solar control and energy production.

Liquid and membrane thermal properties were characterised using techniques as the FTIR and DSC. ESEM pictures were taken to go deeper and determine the quality of the membrane blend on a microscopical scale. The long-lasting test was used to get a better understanding of how the membrane will respond when exposed to an indoor environment.

The indoor characterisation was undertaken moving from simplicity to complexity, starting with the experimental rig settings, uniformity of light source, single cell characterisation, proving the device’s concept, finishing with ray tracing simulations, validation, and an optical and thermal characterisation of the smart window prototype.

Lastly, for the outdoor testing, an experimental board was fabricated using three pyranometers, and I-V tracker, Datalogger (for thermocouples temperature

readings), and a smart window prototype with 6 wt. % HPC & 1.5 wt. % GGF membrane and a reference window at 30°, 60° and 90° of inclination.

The result for all these applied methodologies and experimental designs can be found in chapters 4, 5 & 6 for design and membrane development, indoor testing, and outdoor testing, respectively.

Chapter 4

Design and development of thermotropic membrane for novel smart window

In accordance with the methodology presented in chapter 3, the selected polymers, HPC, HPCM and PNIPAM were characterised in liquid and membrane samples. The optical and thermal characteristics of the samples were investigated to examine the suitability of the selected polymers for smart window application through DSC, FTIRs and UV-VIS spectroscopy. ESEM pictures were taken to evaluate the homogeneity of membrane structure on a smaller scale. Also, a long-lasting test was performed to determine the way the membranes inside the window prototype can retain the water when exposed to indoor conditions. Lastly, A gelling agent test was performed using ethulose to explore further configurations for the thermotropic membrane inside the smart window.

4.1 Characterisations of liquid and membrane samples

Following the methodology described in chapter 3 and the appendix A, a liquid and membrane samples characterisation has been done using different tests to understand the thermal and optical characteristics of the materials selected. Firstly, it was necessary to determine the switching temperature (phase change) of the HPC to match what the literature review previously reported. It is important to note that due to high cost for this test and the difficult access to the DSC testing device, HPC was selected for this test because it is the primary polymer in this

research and its similarity to HPCM. FTIR test, ESEM pictures, prototype window long -lasting test and UV-VIS spectroscopy, were conducted to determine the thermal properties of the samples in the infrared spectrum. Membrane homogeneity, membrane response, when exposed to the indoor environment and optical characteristic of the samples were obtained from the tests.

4.2 Differential scanning calorimetry test

As a result of the micro-DSC, all the samples tested presented a broad curve shape. This particular shape is related to partially crystalline polymers, which give a big peak due to the crystal's distribution, which attaches to the crystalline properties of the cellulose on the HPC. Figure 4.1 shows the DSC test results for HPC 2% wt. and 6% wt. liquid samples, presenting an increase of the heat capacity as the HPC wt. % rises. Regarding the switching point temperature, the lower boundary of the transition phase curve can be seen at $\sim 42^{\circ}\text{C}$ for the HPC 2% wt. sample and $\sim 40^{\circ}\text{C}$ for the 6% wt. sample, which is close to what previous studies have reported for the switching point of HPC [214, 215]. In addition to the transitions, 6% wt. showed higher T_m values with 3 mW and -3.1 mW for cooling and heating respectively, when compared against 2% wt. with 2 mW and -2.2 mW for cooling and heating, respectively. This result can be referred to bigger heat capacity in the sample due to the increasing of the weight percentage of the polymer. Higher heat flow values on the 2 wt. % samples before and after the phase change are caused by water due to its phase change requires $\sim 100^{\circ}\text{C}$, however transition heat gains start before 100°C , hence the more water the sample has, the more heat flow it will present before and after the phase change.

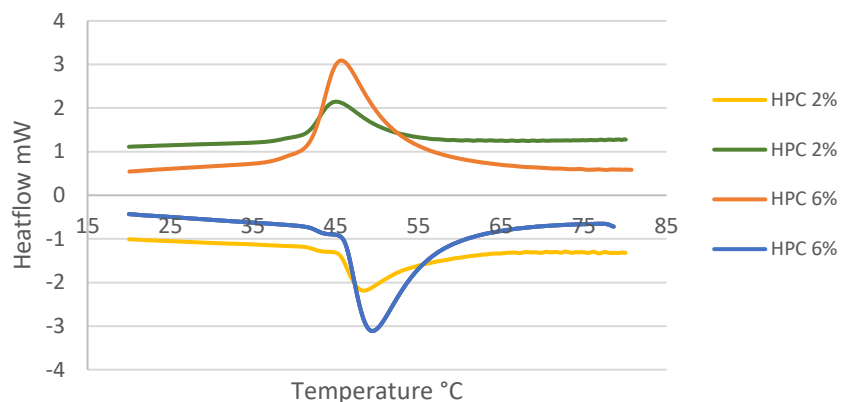


Figure 4.1 Liquid HPC 2 wt. % and HPC 6 wt. % micro-DSC test.

Additional tests were performed to determine how the gellan gum affects the transition phase and thermal behaviour of the membranes. In Figure 4.2 cooling and heating transition phases for all the membrane samples are very similar, with a slight offset caused by the hysteresis between heating and cooling cycles. In the heating cycle, all the samples presented a transition phase with a lower boundary of $\sim 40^{\circ}\text{C}$ and negligible changes after 65°C T_m values were -2.4 mW and -3.5 mW for HPC 6 wt. % and GGF 1.5 wt. % and HPC 6 wt. % and GGF 0.5 wt. % respectively. In contrast, the cooling cycle presented T_m peaks of 2.1 mW and 3.2 mW for HPC 6 wt. % and GGF 1.5 wt. % and HPC 6 wt. % and GGF 0.5 wt. % respectively, proceeding to determine that the bigger the amount of GGF, the smaller the heat capacity. In addition, when comparing the heating cycle in liquid HPC 6% and membrane HPC 6 wt. % and GGF 0.5 wt. %, the T_m values were -3.1 mW and -3.5 mW respectively with a phase transition lower boundary of $\sim 40^{\circ}\text{C}$ for both samples, whereas for cooling, T_m values were 3 mW and 3.2 mW for liquid HPC 6% and membrane HPC 6 wt. % and GGF 0.5 wt. % respectively. These results lead to the conclusion that small amounts of GGF can improve the heat capacity of an HPC and GGF membrane.

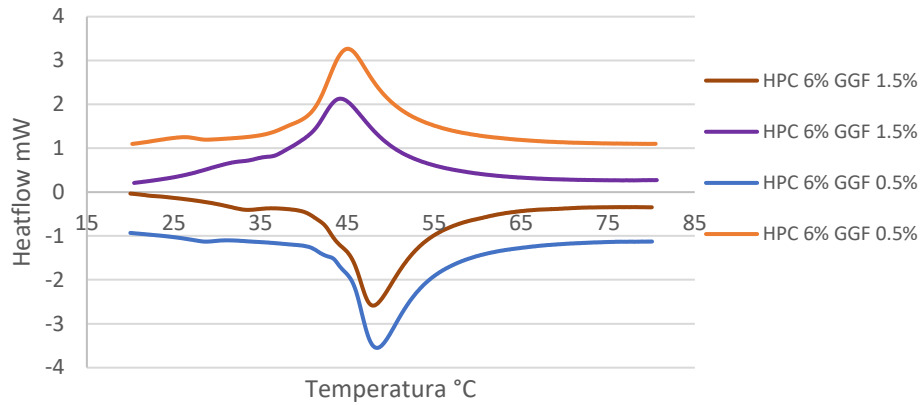


Figure 4.2 HPC & GGF membranes micro-DSC test.

Subsequently, Figure 4.3 shows the cooling and heating transition phases for HPC 6 wt. % and ethulose 1.5 wt. % and HPC 6 wt. % and ethulose 0.25 wt. % membrane samples with similar shapes presenting low hysteresis levels. In the heating cycle, all the samples presented a transition phase lower boundary of $\sim 40^{\circ}\text{C}$ with T_m values of -2.5 mW and -3.3 mW for HPC 6 wt. % ethulose 1.5 wt. % and HPC 6 wt. % and ethulose 0.25 wt. % membranes, respectively. Whereas in the cooling phase, T_m values were 2.1 mW and 3.2 mW for HPC 6 wt. % and ethulose 1.5 wt. % and HPC 6 wt. % and ethulose 0.25 wt. % membranes respectively with no further changes from 65°C to 80°C . Furthermore, T_m values showed higher heat capacity values when the membranes sample had lower ethulose concentration.

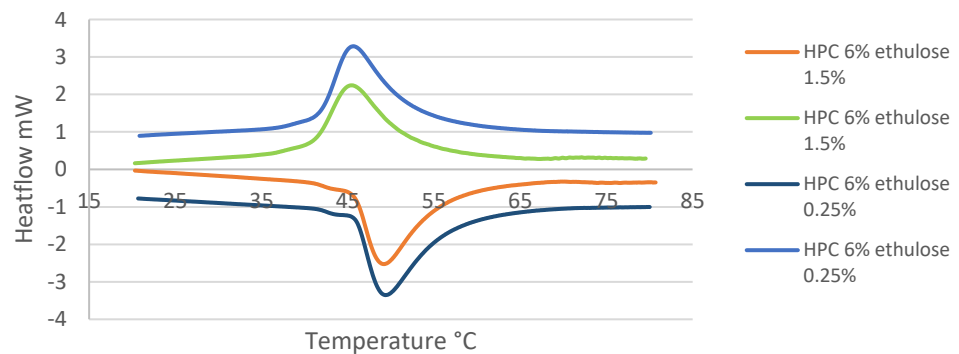


Figure 4.3 HPC & ethulose membranes micro-DSC test

The comparison test between gelling agents at HPC 6% and GGF and ethulose 1.5% is shown in Figure 4.4, revealing that ethulose, despite not having the same OH groups as the GGF, offers good reversibility and heat capacity. Besides, ethulose membrane keeps a steadier flow until reaches the switching point because of stronger chemical bonds to retain water, which can be translated into higher transmittance levels before achieving the cloudy state. Both membranes presented a lower transition boundary of $\sim 40^\circ\text{C}$ in the heating cycle, whereas both presented steadier flows in the cooling cycle after the transition phase. Nevertheless, none of them reached the T_m values of the liquid HPC 6% wt. sample 3 mW, -3.1 mW for cooling and heating, respectively. They only reached 2.4 mW, 3.2 mW when cooling and -3.2 mW, -3.3 mW when heating for GGF and Ethulose membranes, respectively.

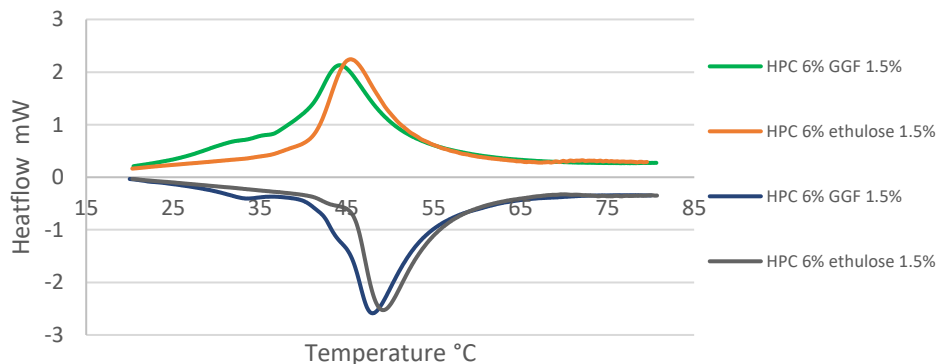


Figure 4.4 HPC & 6 wt. % GGF 1.5 wt. % VS. HPC & 6 wt. % ethulose 1.5 wt. %.
Micro DSC test.

4.3 FTIRs on liquid and membrane samples

To continue with the membrane materials characterisation, FTIRs tests were performed following chapter 3 methodology, starting with the liquid HPC sample. The liquid HPC sample present absorption bands of 3666 cm^{-1} , 2067 cm^{-1} , 1606 cm^{-1} and 1091 cm^{-1} . The first stretch is related to the normal polymeric OH stretch, thereafter water peaks are present around 3400 cm^{-1} . The second bend is located at the 2067 cm^{-1} , which is related to carbonyl group C=O including a connection

with an “aromatic ring” define as organic compounds that consist only of a conjugated planar ring system or possible conjugation with C=C which is the third stretch at 1606 cm^{-1} . The fourth, is the bend at 1091 cm^{-1} and the following peaks are related to water peaks again. The latter explanation can be seen in Figure 4.5.

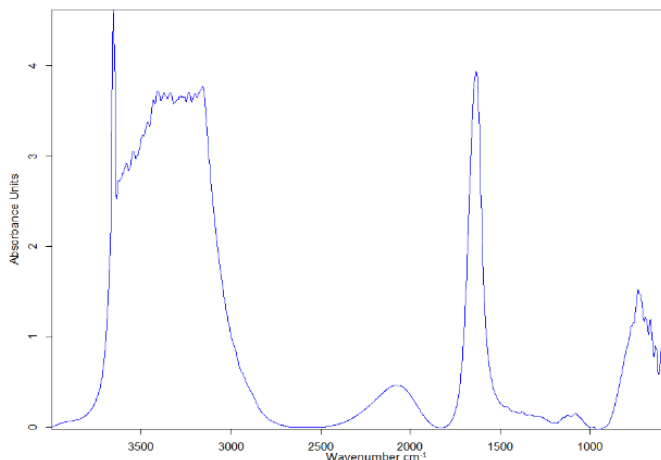


Figure 4.5 FTIR spectroscopy on 6 wt.% HPC and distilled water sample.

Additionally, the comparison between the gelling agents was made with HPC 6% wt. GGF 1.5% wt. against HPC 6% ethulose 1.5% wt. Results shown in Figure 4.6 reveal a similar shape to the liquid test but with a significant difference at the absorbance between membranes samples. The ethulose membrane shows a higher and wider OH stretch absorption band at 3467 cm^{-1} and having similar bends around 2109 cm^{-1} and 1618 cm^{-1} , these highly related to the HPC and distilled water sample. Moreover, a couple of bends appeared at 1103 cm^{-1} and 752 cm^{-1} . These bends are characteristic of a simple hydroxyl compound due to the simple hydrogen-bonded OH absorption of a hydroxyl has this characteristic shape[224]. In contrast, the GGF membrane shows a bend at 3407 cm^{-1} absorption band, also related with the OH stretch plus another bend 1651 cm^{-1} related to the aromatic ring and no further reliable bends to determine any other compound or bonding.

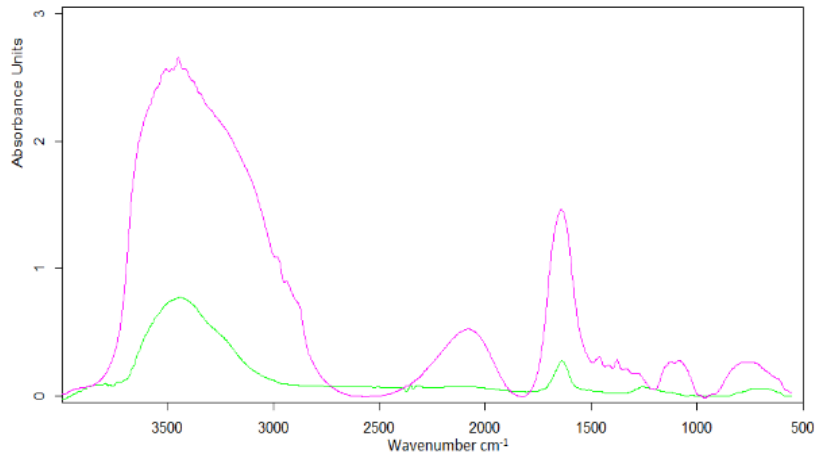


Figure 4.6 FTIR spectroscopy of HPC 6 wt.% GGF 1.5 wt. % in green against HPC 6% ethulose 1.5 wt. % in pink.

Since the solar energy is constituted by 7% ultraviolet, 44% visible light, and 48% infrared[230], it is important to say that almost half of the solar energy will reach the window as heat which the membrane and the solar cells will absorb. The peaks observed on 3467 cm^{-1} , 2109 cm^{-1} , and 1618 cm^{-1} show how the ethulose membrane is responding to the infrared spectrum, namely heat. This absorbance is under Near IR and Mid IR according to the ISO 20473:2007 standard that specifies the division of optical radiation into spectral bands for optics and photonics. The stretch at 1618 cm^{-1} absorption band can be translated into the higher level of heat collected by the material/membrane within the NIR spectrum. The stretch at 3500 cm^{-1} can be understood as less intense heat because it belongs to the Mid IR spectrum, but with a higher absorbance unit and a wider range than the 1618 cm^{-1} stretch. The bend on 2109 cm^{-1} also represents a heat gain but at a smaller level than the latter due to its location at Mid IR and with low absorbance units. Lastly, 1103 cm^{-1} and 752 cm^{-1} represent the closest absorption bands to the Near IR, although small bends are present that should not be neglected. Conversely, the GGF membrane only presents two bends, one at 3407 cm^{-1} and 1651 cm^{-1} with less absorption range and absorbance units compared with membranes that falls within the detection range of the Si solar cells, which is between $0.7\text{-}1\mu\text{m}$, as it can be seen at table 4.1.

Table 4.1. Classification of IR bands according to ISO 20473 standard, which specifies the division of optical radiation into spectral bands.

Type of infrared	Wavelength range (μm)	Semiconductor and detection range
<i>Near</i>	0.7-3	Si (0.7-1); InGaAs, PbSe(1-3)
<i>Medium</i>	3-50	InSb (3-5); HgCdTe (8-14); Si:As (15-30)
<i>Far</i>	50-1000	Thermal detectors

The latter will have repercussions on the passive heat entering the windows into the building, mitigating the cooling and artificial lighting loads providing a smart filter. Nevertheless, energy production can be affected due to any electrical resistance induced by overheating. Hence these materials and membranes are capable of blocking or absorbing the heat from sun rays in different wavelengths, therefore different types of heat.

4.4 ESEM in membrane samples

After characterising the membrane materials with DSC and FTIRs tests, it was proceeded with another fundamental test on the membranes: ESEM imagery provides a microscopic view on to the membranes to determine homogeneity levels. ESEM pictures of HPC, HPMC, PNIPAM with GGF membranes and HPC with ethulose membrane are presented in Figure 4.7. Figure 4.7(a) shows that the HPC membrane is very uniform at 100 μm and 50 μm promoting uniform light transmittance and reflectance. On the other hand, Figure 4.7(b) shows how the HPMC membrane presents a well -mixed surface at 100 μm , which promotes light uniformity and reflectivity at 50 μm , and at a closer look, the sample presents a similar texture as the HPC. Figure 4.7(c) shows PNIPAM membrane, which is highly homogeneous at 100 μm and 50 μm with excellent transmittance and reflectance levels. Lastly, Figure 4.7(d) shows a HPC and ethulose membrane. Here it can be

seen that the membrane is homogeneous with few differences between 100 μm and 50 μm .

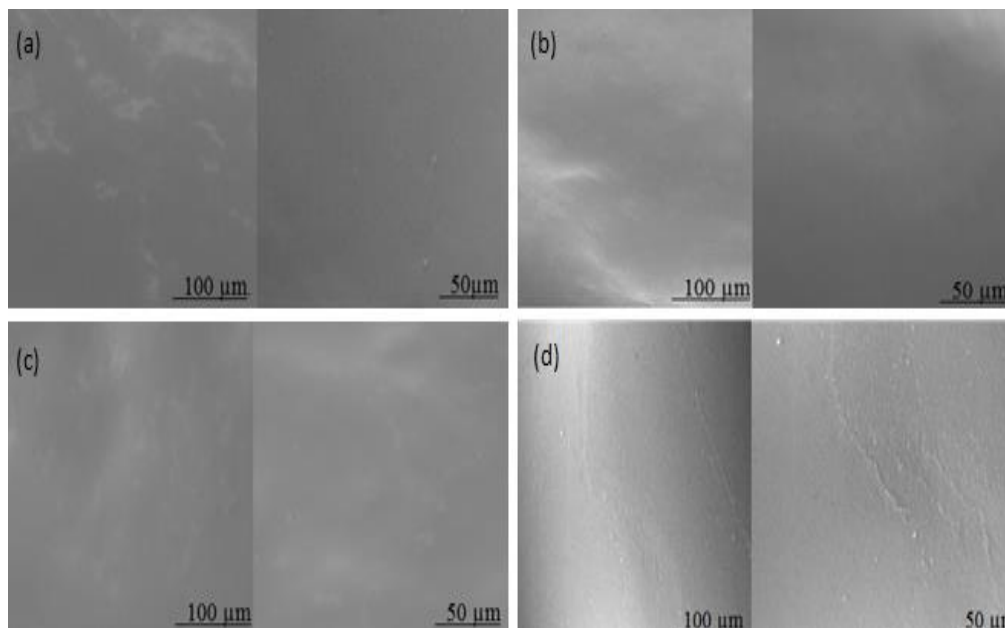


Figure 4.7 ESEM membranes photos (a)HPC & GGF membrane, (b) HPMC & GGF membrane, (c) PNIPAM & GGF membrane and (d) HPC & ethulose.

4.5 Smart window prototype long-lasting membrane test

In addition to the membrane characterisation tools and tests, the long-lasting test was performed to determine how the membranes will respond to the indoor environment, e.g., a smart window with glass damage exposed to the indoor building environment. Figure 4.8 (a) shows the HPC 6 wt. % GGF 1.5 wt. % membrane through the four weeks from A to D, respectively. It can be seen how the first two weeks, the prototype window remains clear and without any water loss (membrane shrink), although on the third week, losses appear with one side presenting shrinking and for the fourth week, transparency levels are affected and shrinking is noticeable on two sides of the prototype window. On the other hand, Figure 4.8(b) depicts how HPC 6 wt. % ethulose 1.5 wt. % smart window prototype presented no variation across four weeks, keeping transparency levels and showing no signs of shrinkage.

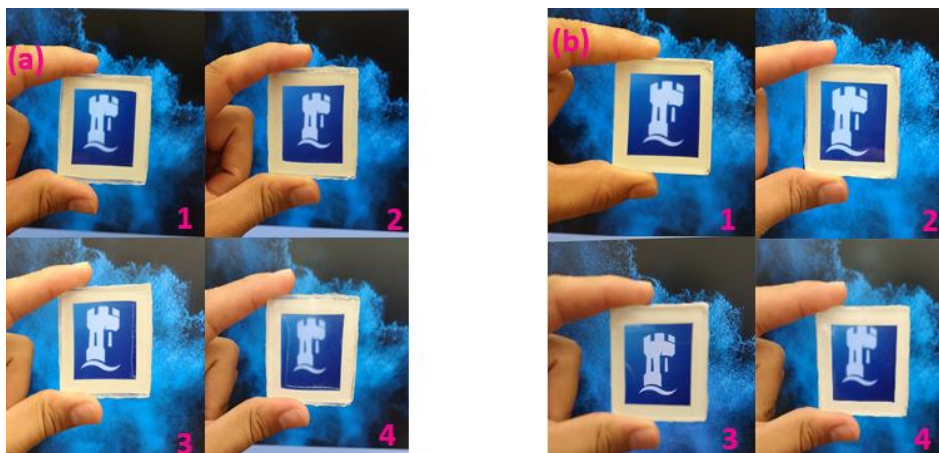


Figure 4.8 Room temperature long-lasting test of the smart window prototypes.

4.6 UV-VIS spectroscopy

After the membrane materials characterisation, the UV-VIS spectroscopy proceeded, aiming to determine fundamental aspects of the materials such as transmittance and reflectance. Because the success of the smart window concept relies on the duality of controlling the sunlight and heat entering the building and providing at the same time high and diffuse reflectivity to fulfil total internal reflection and produce energy. Results of the liquid HPC transmittance test can be seen in figure 4.9, where the heating cycle for HPC liquid samples shows switching points of $\sim 42^{\circ}\text{C}$, $\sim 40^{\circ}\text{C}$ and $\sim 39^{\circ}\text{C}$ for 2 wt. %, 4wt. % and 6 wt. % respectively. These results are very similar in comparison with the literature review reports [214, 215] and HPC liquid DSC results, which were $\sim 42^{\circ}\text{C}$ and $\sim 40^{\circ}\text{C}$, for 2 wt.% and 6 wt.% respectively. Therefore, it can be concluded that the higher the HPC concentration, the lower the switching point will be in liquid HPC samples. Transmittance levels for 2 wt. %, 4wt. % and 6 wt. % samples were $\sim 95\%$, $\sim 93\%$ and 89% respectively compared to the reference, which can be explained with the increase of turbidity as the HPC wt. % increased. Full light scattering was achieved in the cloudy state for all the HPC liquid samples. It was found that there are no significant differences between the cycles in transmittance levels during the

heating and cooling cycle. However, at the same temperature, low hysteresis levels similar to the heating and cooling cycles in DSC HPC liquid test were

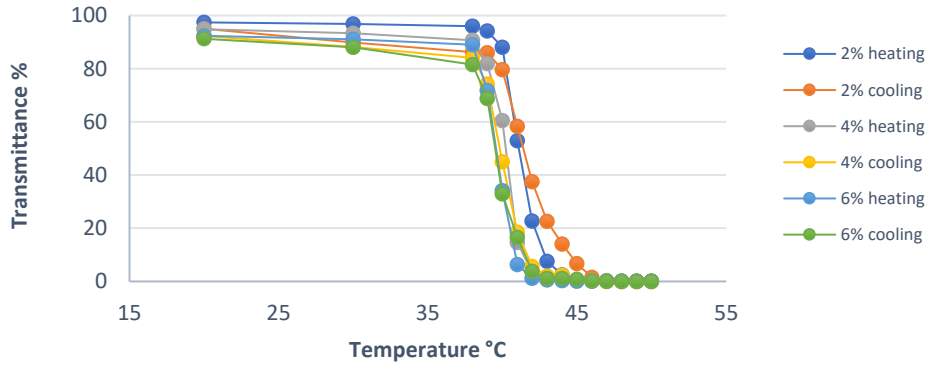


Figure 4.9 Transmittance on HPC liquid samples.

The transmittance variation of HPMC at different temperatures is shown in Figure 4.10, where HPMC samples in a clear state show transmittance levels from ~80%, ~90%, ~96% for 6 wt. %, 4 wt. % and 2 wt. % respectively, displaying higher turbidity levels than the HPC. For the heating cycle the 2 wt. % sample has a switching point of ~50°C, which is reduced to ~48°C and ~45°C for 4 wt. % and 6 wt. %, respectively, values which are within the temperature range presented in the literature review [211, 212]. Therefore, it can be reasoned that increasing the HPMC concentration lowers the switching point in the samples. Additionally, light transmittance levels in a cloudy state transitioned to full light scattering at ~65°C for 2 wt. %, ~63°C and ~60°C for 4 wt. % and 6 wt. %, respectively. Furthermore, in the cooling cycle, the HPCM samples maintain the full light scattering until ~50°C, and then start to recover the clear state. However, the HPMC shows high hysteresis with a significant difference between cooling and heating cycles.

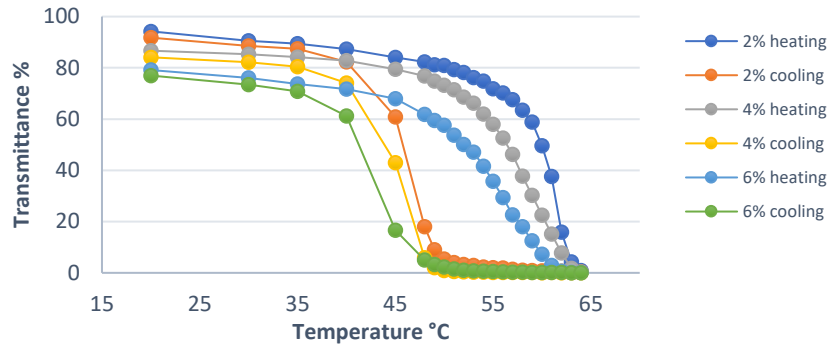


Figure 4.10 Transmittance on HPMC liquid samples

For its part, PNIPAM shows a switching point of $\sim 32^{\circ}\text{C}$, matching previous results presented in the literature review [213]. Transmittance levels of $\sim 98\%$ below the switching point of $\sim 32^{\circ}\text{C}$ for all the samples (2%, 4%, 6%) and almost no changes between samples were observed. Samples switched abruptly from clear to full light scattering, showing almost no hysteresis between cycles. No further changes were recorded as the temperature increased. The latter observations are plotted in the graph of Figure 4.11.

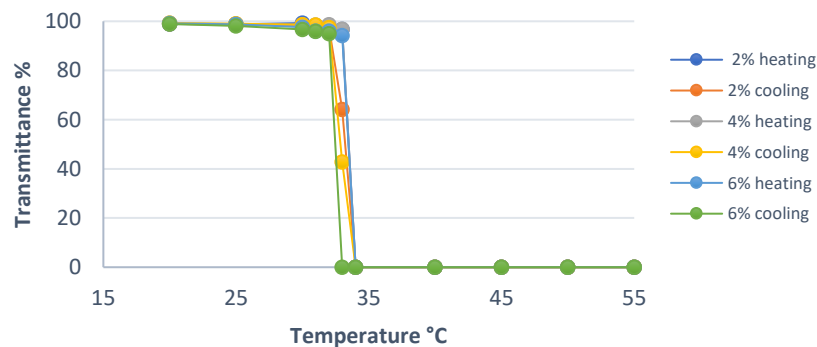


Figure 4.11 Transmittance on PNIPAM liquid samples.

After examining the three selected polymers in liquid samples, three thermotropic membranes were made to compare their optical and thermal performance and determine the effect of gelling agent in the blend. First, the HPC and GGF membrane was made and added to the smart window prototype to proceed with testing. From Figure 4.12 it can be seen that during the heating cycle, high

transmittance levels around 96% were maintained before the switching point for all HPC membrane concentrations is reached. In comparison to liquid HPC tests, these transmittance levels can be attributed to high homogeneity in the blend and the thickness of the smart window membrane compared to the liquid test where the Qpod cuvette thickness is 1 cm against ~0.7mm of the membrane. The switching point values are ~41°C, ~40°C ~38°C for 2 wt. %, 4 wt. %, and 6 wt. % respectively, being similar to what was reported in the HPC liquid transmittance test. A smooth transition from a clear to cloudy state is observed with a more gradual transition than the liquid test due to the new chemical bonds made with the GGF, thus expanding the switching range from 38°C to 55°C. The lowest light transmittance levels achieved for 2 wt. %, 4 wt. %, and 6 wt. % samples were 29%, 24% and 21% respectively. The cooling cycle shows a similar characteristic to the heating cycle, presenting low hysteresis and good reversibility.

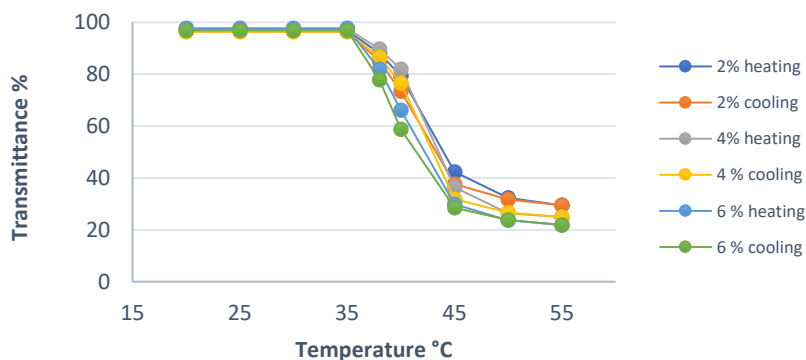


Figure 4.12 HPC and GGF membrane transmittance test.

HPMC & GGF membrane transmittance tests are illustrated in Figure 4.13, wherein heating cycles and transmittance levels of 95% are maintained before the transition; again, this change is related to the membrane thickness and turbidity losses blending when compared against the HPCM liquid transmittance test. Besides, the switching point values are ~55°C, ~50°C and ~45°C for 2 wt. %, 4 wt. %, 6 wt. % respectively, presenting slight changes in switching temperature when compared to liquid test. The transition phase range presented was similar to liquid

test with a transition phase ranging from 45°C to 65°C for the 2 wt. % and 4 wt. %, and 6 wt. %. The lowest recorded values for transmittance were 38%, 31% and 21% for 2 wt. %, 4 wt. %, 6 wt. %, respectively. On the other hand, during the cooling cycles, all samples showed a reduction in hysteresis when compared to the liquid test. This behaviour is related to the increase of elastic properties due to the addition of GGF as a gelling agent.

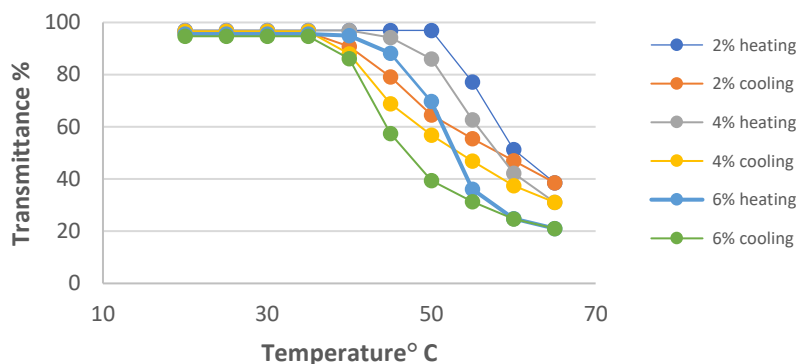


Figure 4.13 HPMC and GGF membrane transmittance test

Figure 4.14 shows the results for the transmittance tests of PNIPAM and GGF membranes, which present transmittance levels of ~98% in all samples during the heating cycle below the switching point and expand the switching range by 1°C compared with PNIPAM liquid test. The increment of PNIPAM wt. % did not affect the transmittance in the clear state. The lowest transmittance levels were 19%, 13% and 10% for 2 wt. %, 4 wt. %, 6 wt. % respectively. After 35°C, the samples presented a steady transmittance without any further change as the temperature increased. The samples did also show almost no hysteresis between the cycles.

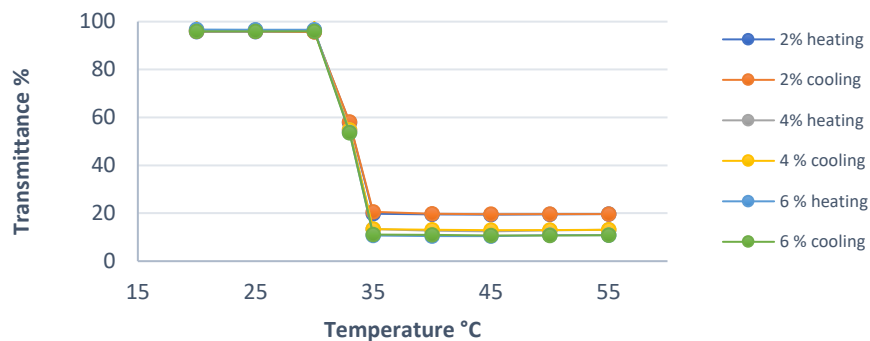


Figure 4.14 PNIPAM and GGF membrane transmittance test.

Ethulose as a membrane matrix was tested, measuring transmittance levels of 3 different samples, all with 6 wt. % HPC but with ethulose at 0.25 wt. %, 0.5 wt. % and 1.5 wt. % respectively. This test showed no significant changes between the concentrations, presenting a smooth curve with a switching point of $\sim 43^\circ\text{C}$ in all concentrations, which represents an increment of 5°C when compared to 6 wt. % HPC and 1.5 wt. % GGF membrane. In the heating cycle before the switching point, all concentrations presented a steady $\sim 99\%$ transmittance level and reaching the lowest transmittance values of 44%, 42% and 41% for 0.25 wt. %, 0.5 wt. % and 1.5 wt. %, respectively. In a direct comparison against the 6 wt. % HPC and 1.5 wt. % GGF membrane, it was found that the ethulose membrane lowest value was 41% against 21% of GGf membrane, thus reducing HPC sunlight blocking capacity. The samples presented good reversibility with almost no hysteresis and similar values across the curve in the cooling cycle. No further transmittance changes were seen after 55°C , only water loses and material degradation. The latter is shown in Figure 4.15.

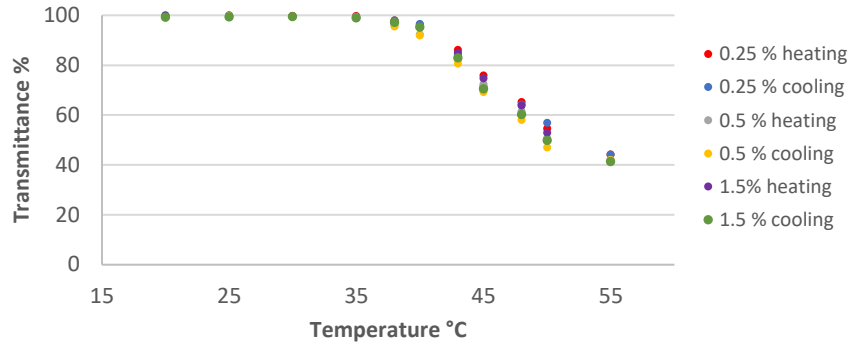


Figure 4.15 Ethulose and HPC membranes transmittance test.

A reflectance test was performed for continuous analysis and register any changes due to the addition of the gelling agents and how they affect the thermal and optical properties of the blend. Although single glass was used as a reference, the reflection level for smart window samples starts at ~13 % due to the reflection of the membrane itself and the bottom glass. Additionally, no further reflectance changes were recorded after 55°C and 65°C for HPC/PNIPAM and HPMC, respectively. Figure 4.16 shows the reflectance test with HPC and GGF membrane, presenting ~14% for all the concentrations at a clear state within a temperature range of 20°C to 38°C. The reflectance range starts at 43°C keeps increasing until 55°C, where reflectance levels of 26%, 37% and 41% are reached by 2 wt.%, 4 wt.% and 6 wt.% samples, respectively, thereby it can be inferred that as the HPC concentration increases the reflectance will increase too. The samples behaviour shows no significant changes between the cycles, being overall highly consistent.

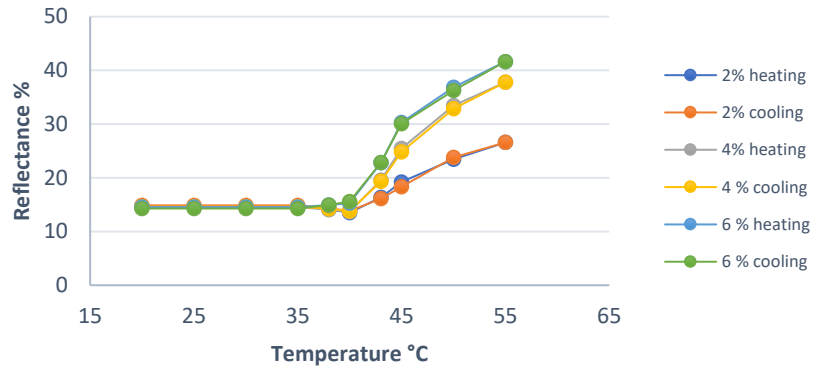


Figure 4.16 HPC & GGF membranes reflectance test.

HPMC membrane has a ~15% reflectance level in the clear state within the temperature range from 20 to 50°C, having only a 10°C range from 55°C to 65°C where reflection is increased. Moreover, reflection on HPMC reached maximum values of ~16% ~25% and ~29% for 2 wt. %, 4 wt. % and 6 wt. %. Respectively. Therefore, when the HPMC concentration was increased the reflection level increased too. The differences between the cycles were minimal, with the cooling cycle presenting slightly lower values than the heating cycle. The previous description can be seen in Figure 4.17.

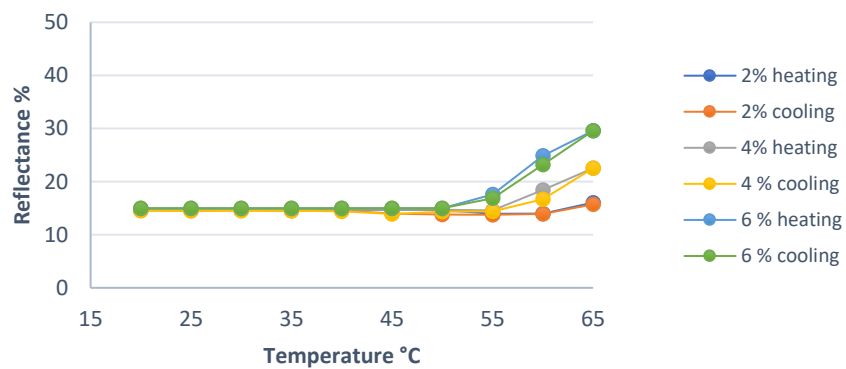


Figure 4.17 HPMC & GGF membranes reflectance test.

PNIPAM and GGF membrane reflectance test results can be seen in Figure 4.18, where steady reflectance of ~14% from 20 to 30°C is shown. In addition, above the switching point membrane presented a sudden change from clear to cloudy state as the membrane transmittance test did. Moreover, the reflection range was

increased by 5°C when compared to the membrane transmittance test. The reflectance values of ~42% for 2 wt. %, ~53% for 4 wt. % and ~57% for 6 wt. % were recorded with good reversibility performance between cycles.

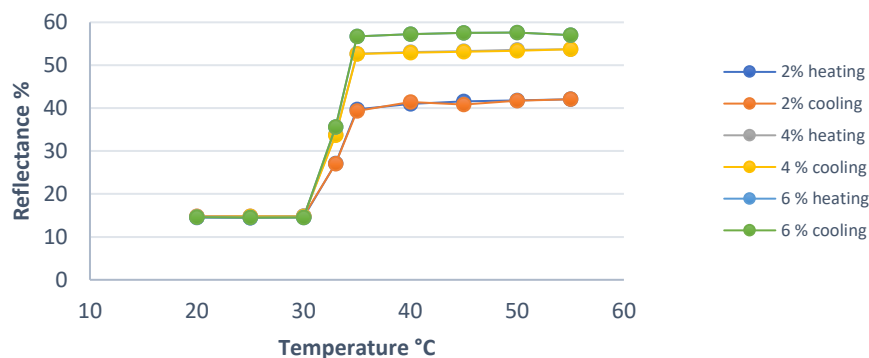


Figure 4.18 PNIPAM & GGF membranes reflectance test.

Similarly, a reflectance test of HPC & ethulose membranes was done. Three membranes were made with 6 wt. % HPC and ethulose at 0.25 wt. %, 0.5 wt. % and 1.5 wt. % respectively. Results showed that in the heating cycle below the switching point, all the samples presented a ~13% reflectance level, whilst above it, the values were 28% for 0.25 wt. % and 29% for 0.5 wt. % and 1.5 wt. %. On the other hand, in the cooling cycle, the samples present good reversibility and similar heating cycle values. Moreover, similar to the transmittance test, no further reflectance changes were recorded after 55 °C only water loses and material degradation. The latter explanation and results are depicted in Figure 4.19.

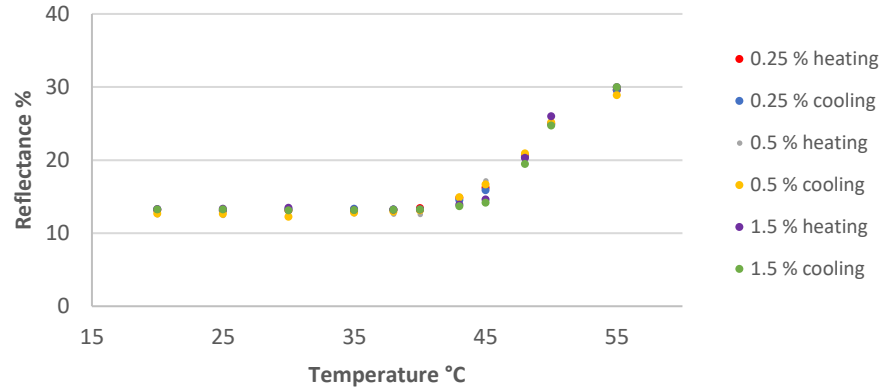


Figure 4.19. Ethulose and HPC membranes reflectance test.

Lastly, it is fundamental to assess the particularities of each gelling agent used in this research. Therefore, GGF and ethulose were cross-compared both with the same polymer (HPC) concentration to get a better understanding of their features. In Figure 4.20 a comparison of 6 wt.% HPC 1.5 wt.% GGF vs. 6 wt. % HPC 1.5wt.% ethulose membranes can be seen. For the transmittance, cloudiness starts early on GGF membranes. A lower transmittance level is achieved with steeper change, whereas on ethulose the transition is smoother, less steep, and blocking ~20% less light against GGF membrane. For reflectance, levels below the switching point are similar, whilst above it, GGF membrane shows higher reflectivity reaching more than 40% and an early transition. Conversely, ethulose membrane has a slower transition phase to achieve cloudy state and reaches lower reflectance around 30%. The latter behaviour of the ethulose sample against GGF can be explained by the way it interacts with HPC in chemical bonding when they are blended. Since the GGF offers more capability to OH bonding, HPC will take over and lead the behaviour more like the HPC does. In contrast, ethulose, which offers less capability to OH bonding due to chemical structure ($\text{CH}_2\text{CH}_2\text{OH}$), will get less of this behaviour, leading to slower response at the temperature changes and lower values than its GGF counterpart.

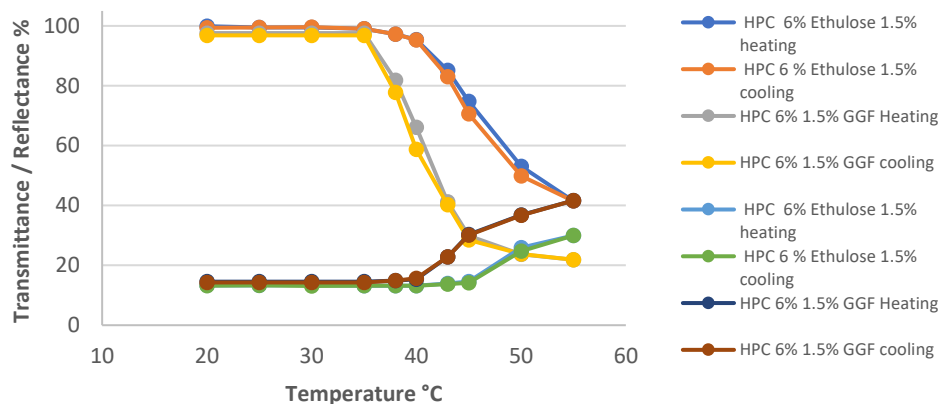


Figure 4.20. Comparison of HPC & GGF membrane against HPC & Ethulose membrane.

4.7 Conclusions

Throughout this chapter, membrane materials were characterised using different tests such as DSC, FTIRs, and UV-VIS spectroscopy, thereby obtaining a better understanding of the materials characteristics and how they can be utilised. First, DSC was used to examine the membrane materials in a more controlled environment, helping to determine more precisely the switching point of the materials and heat capacity through the phase change. Fourier Transform Infrared spectroscopy for the GGF and ethulose membranes showed that ethulose membrane is more likely to absorb upcoming heat in the IR than GGF. However, this heat can be taken as an offset of cooling loads helping to control the indoor temperature of a room or energy transformed by the solar cells. On the contrary, if this heat exceeds the capacity of the solar cell, it may fall into overheating decreasing the solar cells energy production.

Based on chapter 3 methodology, UV-VIS spectroscopy was done, validating the switching temperatures of selected polymers against what previously was presented in the literature review. In regard to the liquid transmittance test, the three selected materials provided acceptable transmittance levels at a clear state, and they all achieved full light scattering. It is important to note that HPC had high

transmittance levels in all concentrations before the switching point, losing only 6% from 2 wt. % to 6 wt. %, and showing low hysteresis between heating and cooling cycles. In contrast, HPMC had a lower transmittance in the clear state, being the most affected by the wt. % increment, losing 16% of transmittance from 2 wt. % to 6 wt. % and presenting hysteresis between cycles. PNIPAM had not significant changes between concentrations in transmittance levels before switching point with a narrow phase of change, and no hysteresis was reported.

Additionally, HPC, HPMC and PNIPAM were synthesised in membranes, analysing their transmittance and reflectance under different temperature conditions. Unlike a liquid, in membrane tests, the materials did not achieve the full scattering state i.e., the transmittance did not reach 0% when above the transition temperature. PNIPAM was the best material with ~10% of light transmittance at 6% wt. sample keeping the narrow phase change as achieved in the liquid test. HPC had a slight change from its liquid test results, gaining a smoother transition phase with a lower transmittance value of 21%, and HPMC reduced hysteresis from the liquid test with a lower transmittance level of 21%. Regarding the reflectance test, again, PNIPAM reached the highest level with ~57% followed by HPC ~41% and HPMC ~29%, all of them with similar reflectance values on clear state around 14%. To sum up, HPMC has lower transmittance levels than HPC and PNIPAM but offers a larger transition phase providing smooth transition for building integration and environments with people, low reversibility, and less opportunity to generate energy due to low reflectivity. For its part, PNIPAM offers high reflectance and light scattering with abrupt phase change, but with the trade-off of more complex handling. Lastly, HPC offers gentle phase changing, lower transmittance levels at high temperatures, high reflectance, and low market price.

The gelling agent comparison between GGF and ethulose showed that GGF had higher transmittance and reflectance levels due to more OH radicals blended within, making the hydrogen bonding in the membrane predominant. On the other hand, ethulose, although not having OH radicals as GGF, offers excellent stability,

reversibility and slightly more heat capacity and a noticeable better absorption in the NIR zone. Additionally, the transition phases for both membranes showed an increase or decrease of heat capacity as the gelling agent percentage varied.

After completing the membrane materials characterisation and experimental data validation in liquid and membranes samples, the ground is set to advance to the next stage. Accordingly with the data gather and validated it was proceeded to select 2% wt. HPC & 1.5 % wt. GGF and 6% HPC & 1.5 % wt. GGF membranes for laboratory indoor testing. Moreover, the smart window prototype was built adding the solar cells to the device to validate indoor results against raytracing and test its full performance.

Chapter 5

Indoor optical, electrical, and thermal characterization of smart window prototype

This chapter presents the optical, thermal, and electrical characterization of a prototype smart window made by low iron optical glass, a thermotropic reflective membrane and a PV cell attached on the glass edge. This smart window is designed to control daylight in a building and produce energy at the same time. The device's concept validation was performed using a 97% reflectivity layer which was attached to the smart window. The collected data was compared to raytracing modelling. Additionally, the prototype characterization was carried out under controlled indoor conditions inside the lab, selecting three irradiance levels, low 170 W/m², mid 400 W/m² and high 700 W/m² using membranes with 2% wt. HPC & 1.5 % wt. GGF and 6% wt. HPC & 1.5 % wt. GGF.

5.1 Single-cell characterisation

To begin with the smart window components characterisation, two single PV cells were electrically characterised. The values obtained in the I-V curve test from these two selected PV cells can be seen in Table 5.1, where small changes are seen in the comparison of short-circuit current, open-circuit voltage, maximum power point and fill factor from one to another PV cell prototype. Saturn PV cell data reports an efficiency of 16% under AM 1.5 standard. This could not be reached due to difficulties to control the room temperature and light source, poor uniformity,

and the overheating of the samples. All these factors impacted the performance of the PV cells, details of I-V curve tests of the PV cells are shown in Figure 5.1.

Table 5.1 Characterization results of the PV cells.

<i>Cell measurements</i>		
	Cell 1	Cell 2
Room temperature	26.1°C	26.4°C
Irradiance	700 W/m ²	700 W/m ²
Short circuit	0.131 A	0.132 A
Open circuit	0.578 V	0.578 V
Maximum power point	0.0614 W	0.0614 W
Fill Factor	0.810	0.805
Efficiency	12.6%	12.5%

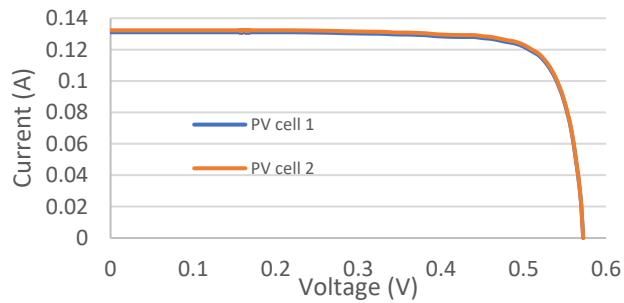


Figure 5.1. PV cells I-V curve measurements.

Consequently, since both solar cells present similar conditions, it was proceeded to the I-V Tracker measurements using solar the PV cell covered with optical glass because these PV cells will be covered by optical glass when incorporated into the smart window prototypes. Hence this helps to determine any possible changes in respect to the single-cell characterization. Firstly, different irradiation tests were performed on the single-cell prototype to see the variation on I-V curve values along with the low, mid, and high irradiance levels. These changes show a substantial increment in short circuit current, whereas for open-circuit voltage, the variation in values is less, although it keeps increasing as the irradiation level increases. The Improvements of short-circuit current are observed to be 126.4%

when the irradiance is raised from 170 W/m² to 400 W/m² and 73.4% when from 400 W/m² to 700 W/m², as can be seen from Figure 5.2.

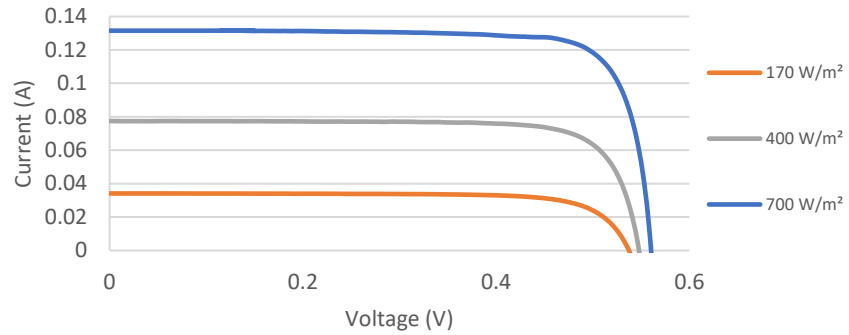


Figure 5.2 Low, mid, and high irradiance comparison.

Secondly, the temperature effect on I-V curve values was monitored. The laboratory's ambient air temperature ranged between 25.6 °C to 26.1 °C during the whole experiment. The PV cell temperature was also monitored by two thermocouples attached in the back of PV cell and the selected temperature range was from 28°C to 40 °C. The I-V curve measurements were taken every time the PV temperature was increased by 2 °C at 700 W/m². Figure 5.3 shows how the I-V curve values are changing from 28°C to 40 °C. However, those values did not change significantly, representing only a 4% variation from the lowest to the highest MPP. Additionally, the current values had small changes across the temperature range, and all the curves follow the same pattern before the curve's knee, whereas the voltage experienced small drops when the PV temperature increases.

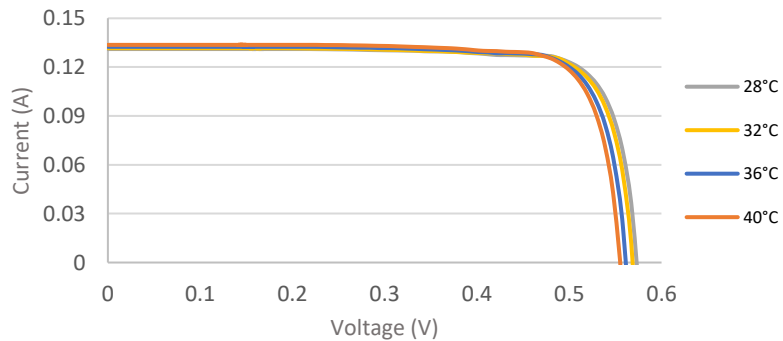


Figure 5.3 Temperature profile test on I-V curves at 700 W/m².

Figure 5.4 shows the efficiency variation under the temperature range of 28°C to 40°C at 700 W/m². Although changes are expected due to the thermal resistance when the PV cell increase s its temperature, the standard error variation average rate is 0.0038 each 2°C because these changes occur in a smooth way on a descend trend when the temperature increases.

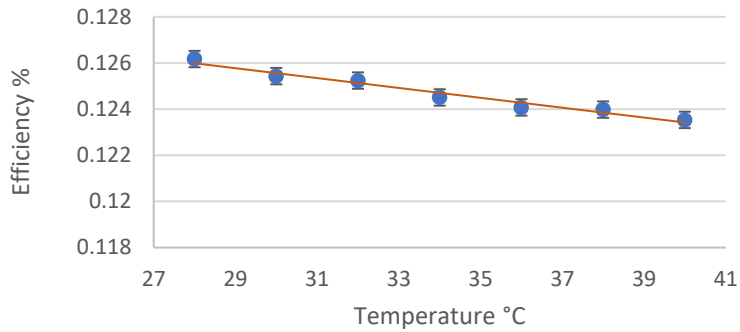


Figure 5.4 Efficiency variation from 28 °C to 40 °C at 700 W/m².

Lastly, in the same fashion, fill factor changes across 28°C to 40°C at 700W/m² were evaluated to complete this characterization. In figure 5.5 shows that the fill factor has a minimum millesimal linear decreasing rate when the PV temperature increases; therefore, changes in fill factor are negligible due to very low variation.

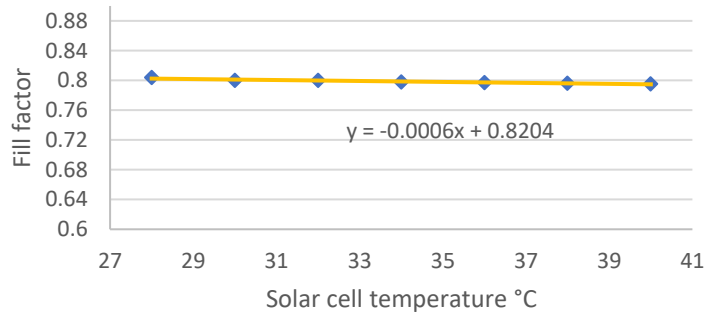


Figure 5.5. Fill factor from 28 °C to 40 °C at 700 W/m².

5.2 Smart window concentration concept

In order to begin with lab indoor characterization; two scenarios were selected to validate the smart window concept. The first was one compared the single PV cell

vs the smart window with a reflective layer attached to determine how the device performs as a solar concentrator. The second one was carried out to validate the smart window prototype indoor testing through ray tracing modelling, comparing both values. The first scenario test was performed on the smart window prototype with the reflective layer attached under the three selected irradiation levels, low, medium, and high and then compared against single-cell measurements to determine possible differences. Variations detected for single-cell and smart window prototypes were 5%, 8% and 6% for 170 W/m², 400 W/m² and 700 W/m² respectively with an average value for all of 6.3%. These can be addressed to the 3% missing from the reflective layer which is 97% reflectivity. The testing angle which was 0°, differing from the critical angle for this glazing which is approximately 41.1°, hence dropping up to 2.4% the optical efficiency of the device according with previous publication in this research [200]. The rest can be related to the optical losses due to reflections on the cover glass, rays not reaching the critical angle to fulfil the total internal reflection or escaped through the edges where there is no PV cell attached. Furthermore, additional losses can be caused by the non-uniformity of the light flux representing a drawback to get the maximum concentration ratio. Figure 5.6 shows the I-V curves from the latter explanation.

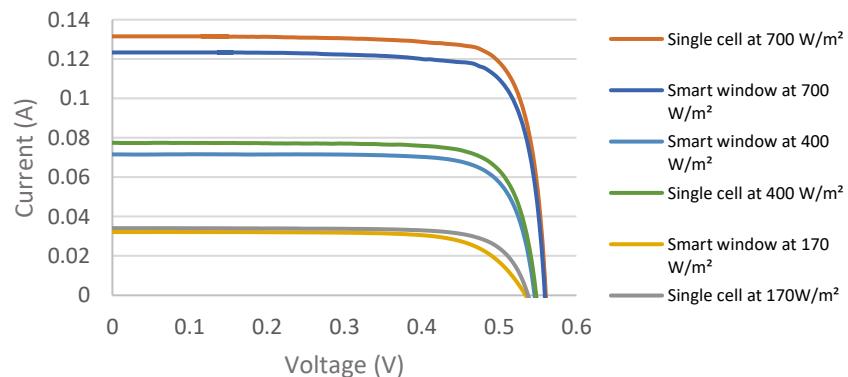


Figure 5.6. Smart window VS. Single cell I-V curves at 700 w/m².

5.2. Raytracing modelling validation

To validate the second scenario, the accuracy of the power output value from the simulation was compared against the experimental lab testing, using the same parameters used in lab experimental work with the smart window prototype as ray tracing simulation inputs. Results from ray tracing simulation are based on the irradiance map for absorbed flux, representing the number of watts absorbed by the solar cell during the simulation. However, to get accurate data to be compared with the lab experimental testing Equation 7 must be fulfilled:

$$MPP = I * \eta * A_{pv} \quad (7)$$

Where MPP is the maximum power point, I is the absorbed flux in the selected surface, η is the PV cell efficiency, and A_{pv} is the PV cell area. Details of the irradiance map are shown in figure 5.7.

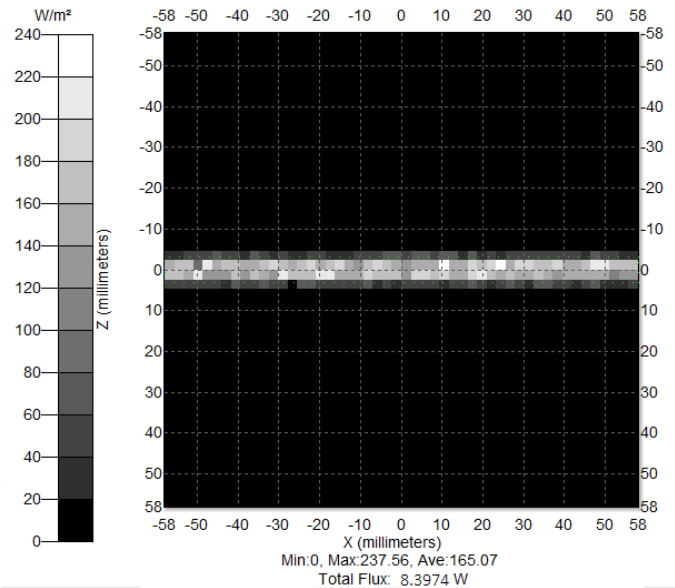


Figure 5.7 Irradiance maps for absorbed flux.

Consequently, filling the latter equation, the power output of the simulation at 700 W/m² was 0.0701W, which compared against the MMP of the smart window with the reflective layer attached at 700 W/m² was 0.0693 W, obtaining 8% of a

discrepancy, thereby leading to a state that the ray tracing is reliable to conduct experimental work and be reproduced on the lab successfully.

5.2.2 Smart window optical performance modelling

The optical performance of the smart window is linked to the optical efficiency and the effective concentration ratio (C_e), however using only a single wavelength to determine its performance cannot be accurate. Therefore, 15 points from 0.35 μm to 1 μm range were selected to determine the changes of the optical efficiency and C_e across the range of the Si solar cells, which is between 0.7-1 μm according to the classification of IR bands in the ISO 20473 standard. Thereby, an optical simulation was done for the smart concentrating PV to determine the C_e across the selected wavelengths at a solar incidence angle of 0° from a vertical position on top of the aperture cover. The model inputs were the following: A 116 x 116 x 6 mm optical glass with a refractive index of 1.52, one Saturn silicon BP solar cells of 116 x 6 mm mounted at the edge of the glazing cover. Additionally, the absorptivity of the solar cell is 1, and the geometric concentration ratio of the smart window is 1.2x. Values for the optical efficiency and C_e were around 0.3 μm to 0.5 μm at the lowest. This condition is related to the number of rays falling in this wavelength and the spectral response of the PV cells. However, as the wavelength values get closer to the visible light spectrum, they presented better values for both. Additionally, average optical efficiency values of 90% and $C_e = 1$ are seen from 0.5 μm to 0.9 μm , concluding there are no further changes in the device's optical properties across its spectral functionality range. The latter explanation is shown in Figure 5.8.

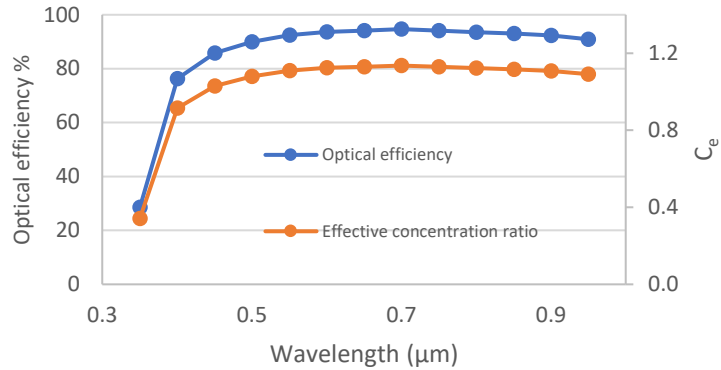


Figure 5.8 Predicted optical performance of the smart window.

5.3 Smart window prototypes with thermotropic membrane

After the single PV cell characterisation and the ray tracing model validation was accomplished, the 2% wt. HPC & 1.5 % wt. GGF, and 6% wt. HPC & 1.5 % wt. GGF thermotropic membranes were made following Appendix A methodology, and the PV cells were added to the smart window prototype to proceed with the indoor testing.

5.3.1 2% wt. HPC & 1.5 % wt. GGF membrane

The indoor testing started with the smart window prototype using the 2% wt. HPC & 1.5 % wt. GGF membrane under 400 W/m² irradiance average value. Overall, the result curves do not present big changes from 28°C to 36°C; this is because the membrane is on clear state, allowing the light to pass through. However, after 38°C the phase change starts, then cloudiness appears; thus, the device starts to produce more energy due to the increase of the total internal reflection occurring inside the glass. It is worth to mention that under 400 W/m², the device will not reach more than 46°C. As shown in previous work, transmittance and reflectance at this membrane concentration keep changing until 55°C, not reaching the expected transmittance and reflectance levels, hence producing less energy. The latter description is shown in Figure 5.9.

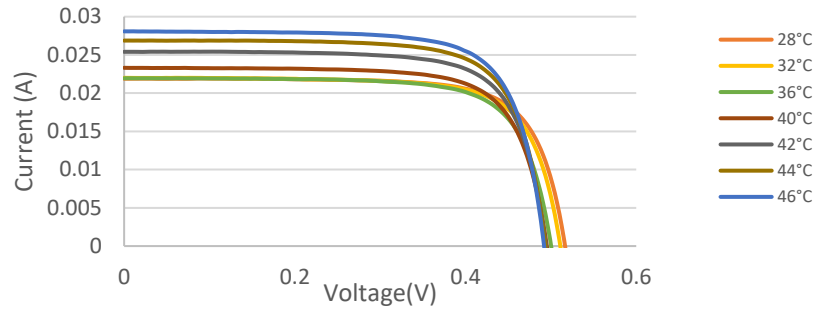


Figure 5.9 Smart window temperature profile using the 2% wt. HPC & 1.5 % wt. GGF membrane under 400 W/m².

Figure 5.10 shows the power curves presenting a 25% power output improvement from clear to light scattering state, where the clear state average was ~0.008W, and the highest value was 0.010W. Additionally, in these curves, open circuit voltage varies slightly due to the temperature rising in the PV cells. Maximum power values were achieved after 40°C, when the phase change occurs.

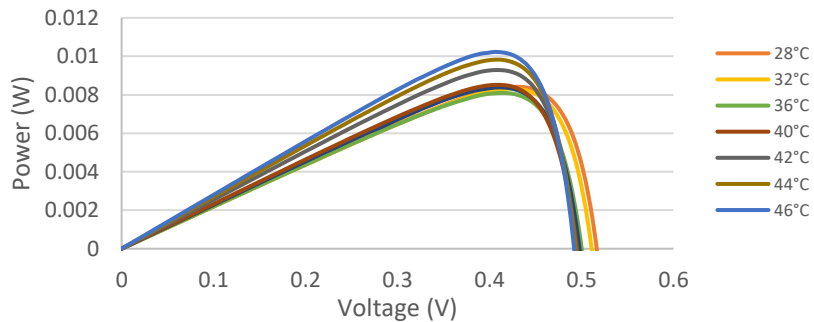


Figure 5.10 Smart window power curves using the 2% wt. HPC & 1.5 % wt. GGF membrane under 400 W/m².

Figure 5.11 depicts the correlation between MPP and light transmittance across the temperature range from 28°C to 46°C, where the clear state maintains a steady line until 38°C, where the first power increment is noted at 40 °C with increase until 46°C. This behaviour is directly proportional to the light transmittance, where the first change can be seen at 40°C, where the MPP increases for the first time and keeps increasing as the phase change occurs, like the power output that keeps increasing until 46°C. On the other hand, transmittance level (T. %) remains close

to 100% until 38°C, then after 40°C transmittance level starts to decrease as the phase change occurs reducing transmittance level to 62%.

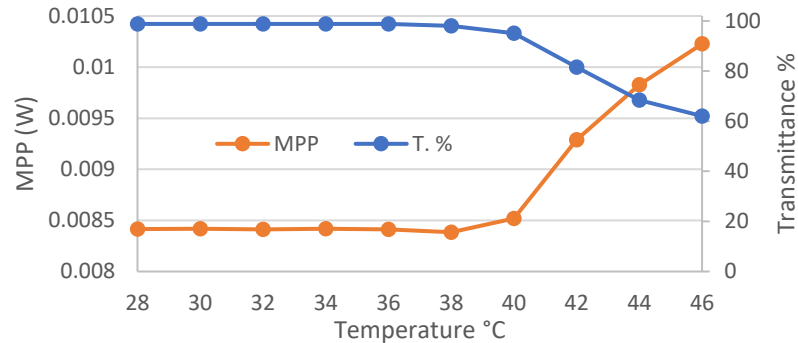


Figure 5.11 Light transmittance versus power output on smart window using the 2% wt. HPC & 1.5 % wt. GGF membrane under 400 W/m².

Unlike the 400 W/ m² test, the 700 W/m² test was capable of reaching 50°C, which is only 5°C away from its lowest transmittance and highest reflectance levels recorded in the previous chapter, thereby producing more energy. In the Clear state the short circuit current average value was ~0.038A, which, in comparison with the 400 W/ m² test with ~0.021A, represents an improvement of 80%. Whereas after 40°C, when the phase changing occurs, average values of ~0.027A and ~0.049A for 400 W/m² and 700 W/m² respectively were achieved, which represents an improvement of 81 %. Regarding the power-Voltage curve on clear state, the 400 W/ m² test average value was ~0.008 W compared to the 700 W/ m² test, which was 0.014 W showing an improvement of 75%. On the other hand, at the light scattering state highest value was 0.010 W for the 400 W/ m² test and for 700 W/ m², 0.018 W, which is an improvement of the power output of 44. The latter explanations can be seen in Figures 5.12 and 5.13.

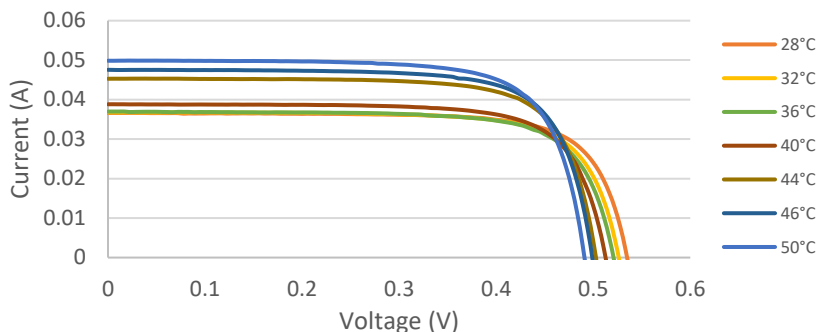


Figure 5.12 Smart window prototype I-V curves using the 2% wt. HPC & 1.5 % wt. GGF membrane under 700 W/m².

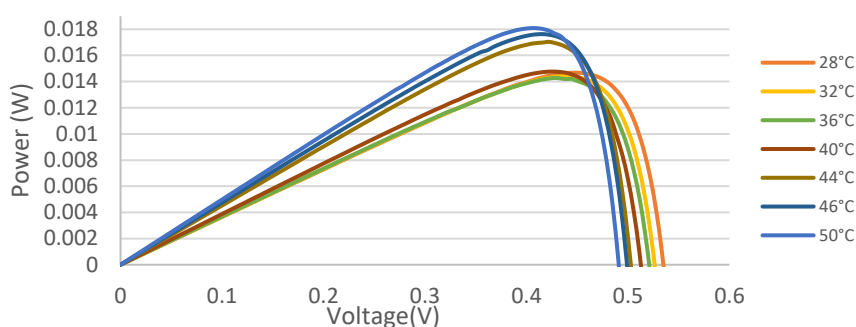


Figure 5.13 Smart window prototype Power curves using the 2% wt. HPC & 1.5 % wt. GGF membrane under 700 W/m².

The correlation between MMP and transmittance levels at 700 W/ m² is shown in Figure 5.14, where it can be seen how at higher irradiation levels the smart window presents earlier phase change starting at 38°C, reducing transmittance levels and getting higher MPP values until 50°C.

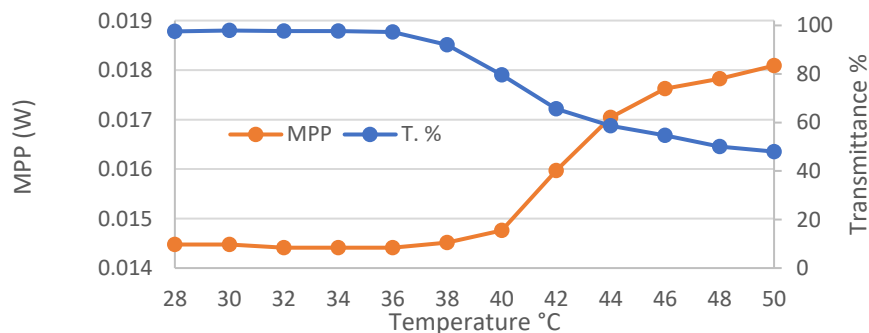


Figure 5.14 Light transmittance versus power output on smart window prototype using the 2% wt. HPC & 1.5 % wt. GGF membrane under 700 W/m².

An additional analysis of the temperature on the smart window was done, with a time lapse experiment of 30 minutes, with the membrane, top glass, bottom glass, and PV cell temperatures monitored and recorded. For this analysis, the membrane temperature was the main reference as the changes on the device were determined by the phase change of the membrane.

In Figure 5.15 it can be seen how the membrane and the top glass had the same temperature until 36°C, while the PV cell was ~1°C above and the top glass was ~1°C below. When the temperature reached 38°C, the first change was visible as the PV cell temperature matched the membrane temperature, whereas the top and bottom glass temperature remained ~1°C below the membrane and the top glass temperatures, respectively. This trend continued until the end of the experiment presenting some variation at the end of it, which can be related to the materials' thermal gains and losses. On the other hand, the MPP shows a steady line from 28°C to 36°C. At 38°C, a small decrease of the PV cell temperature was observed matching the membrane temperature, which can be explained with an increase of the thermal resistance. At this point, the phase change starts happening. Therefore, MPP values increase simultaneously as the reflectance values increase, trapping more rays by total internal reflection until the maximum temperature is achieved. After the first 30 minutes, no further changes were recorded in MPP or the window components values; therefore, no more data was plotted.

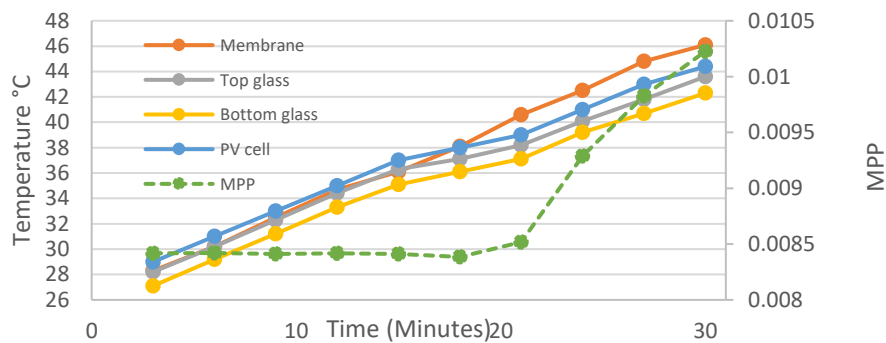


Figure 5.15 Smart window prototype temperature profiles at 2% wt. HPC & 1.5 % wt. GGF under 400 W/m².

5.3.2 6% wt. HPC & 1.5 % wt. GGF membrane

Results of the temperature profile of the smart window with 6% wt. HPC & 1.5 wt. GGF at 400 W/m² is shown in Figure 5.16, where from 28°C to 36°C, no significant changes were observed because the smart window is in clear state. After 40°C, the cloudiness started appearing, and the short circuit current values increased as well, with a small decrement in open-circuit voltage due to the temperature rise. In comparison with 2 wt. % HPC & 1.5 wt. % GGF membrane under 400 W/m², the maximum short-circuit current value was ~ 0.028 A and for the 6% wt. HPC & 1.5 5 wt. GGF at 400 W/m² was ~0.036 A, presenting an increment of 28%.

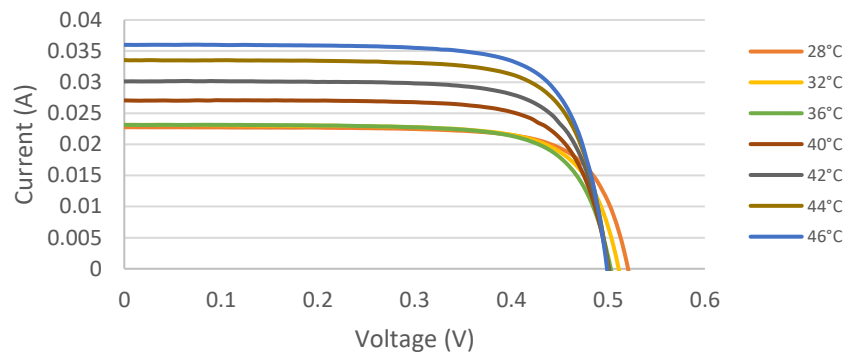


Figure 5.16 I-V curves Smart window prototype with 6% wt. HPC & 1.5 % wt. GGF membrane under 400 W/m².

The 6% wt. HPC & 1.5 % wt. GGF smart window power curves at 400 W/m² are shown in Figure 5.17. The comparison of power output at clear state against the light scattering values from 28°C to 36°C showed similar values, while after 36°C an improvement of 44% is observed with an average of ~0.009W against 0.013W, which was the highest.

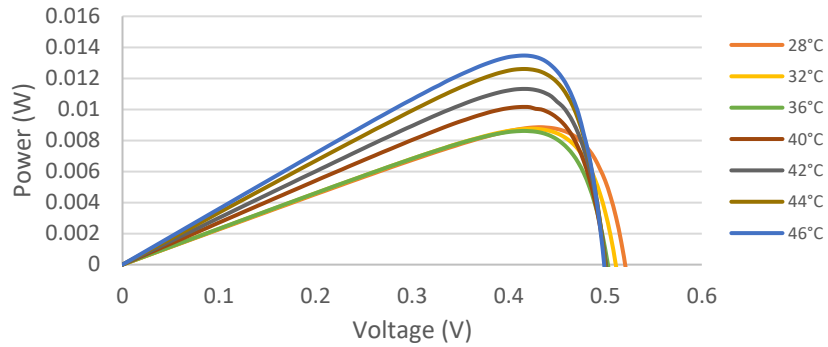


Figure 5.17 Power curves Smart window prototype with 6% wt. HPC & 1.5 % wt. GGF membrane under 400 W/m².

The correlation between MMP and transmittance levels at 400 W/ m² in a smart window prototype with 6% wt. HPC & 1.5 % wt. GGF is presented in Figure 5.18. This graph shows how the 6% HPC membrane obtained more stable results compared against 2% at 400 W/ m² and 700 W/ m², higher MMP values and lower light transmittance levels.

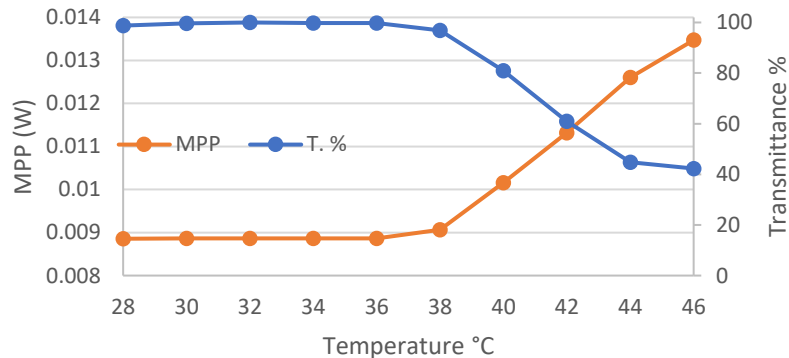


Figure 5.18 Light transmittance versus power output on the smart window prototype using the 6% wt. HPC & 1.5 % wt. GGF membrane under 400 W/m².

Consequently, the smart window prototype with 6% wt. HPC & 1.5 % wt. GGF membrane at 700 W/m² was tested, where the I-V curve results showed how, at this concentration, the smart window presented bigger changes between the range of temperature. From 28°C to 32°C, the short circuit current keeps at a steady value but started to increase until 50°C. An improvement of 82% was found from the direct comparison of clear state short circuit current average value of

0.035A to 0.064A, which was the highest recorded light scattering value. The latter explanation can be seen on Figure 5.19.

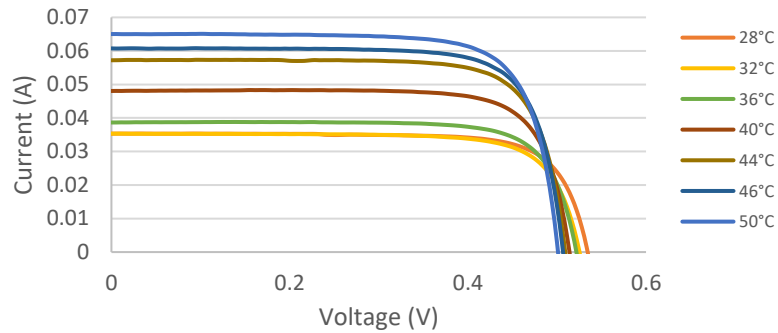


Figure 5.19 I-V curves Smart window prototype with 6% wt. HPC & 1.5 % wt. GGF membrane under 700 W/m².

On the other hand, in Figure 5.20, similar behaviour can be seen in power curves after 32°C, where changes are noticeable. Power output improvement from clear to light scattering is 71%, based on a clear state average value of 0.014W compared to 0.024W, the light scattering highest value.

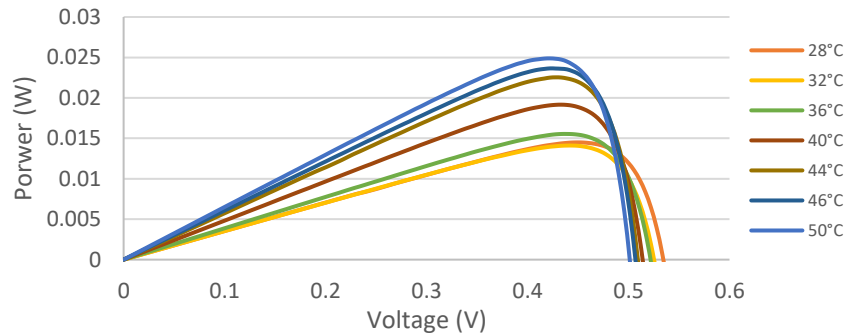


Figure 5.20 Power curves Smart window prototype with 6% wt. HPC & 1.5 % wt. GGF membrane under 700 W/m².

The correlation between power generation and transmittance levels at 700 W/ m² in the smart window prototype with 6 wt. % HPC & 1.5 wt. % GGF is presented in Figure 5.21, where the smart window presented changes in transmittance slightly before 36°; after passing this temperature transmittance level keeps decreasing close to 30%. Also, power output increases significantly and keeps increasing after

36°C until reaching 0.024 W at 50 °C, being the highest recorded value for all the concentrations and irradiances.

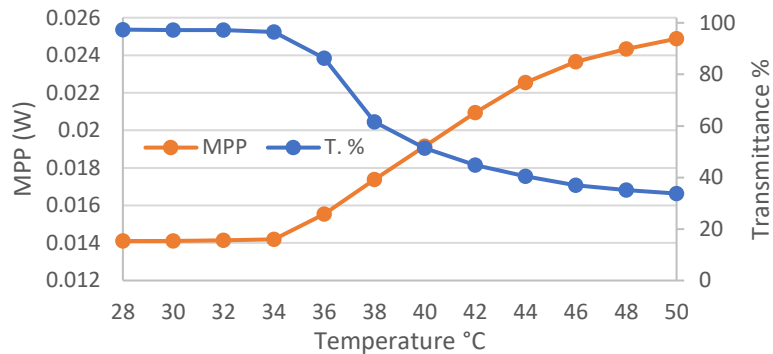


Figure 5.21 Light transmittance versus power output on smart window prototype using the 6% wt. HPC & 1.5 % wt. GGF membrane under 700 W/m².

Lastly, another analysis of the smart window temperature was done, using the same conditions as the 2 wt. % HPC & 1.5 wt. % GGF, monitoring and recording the membrane, top glass, bottom glass, and PV cell temperatures. In Figure 5.22 it can be seen how the membrane has a slightly higher temperature than the top glass until 36°C; this temperature difference can be related to the expanded heat capacity of the membrane due to the increase of the HPC. Additionally, PV cell, top glass and membrane have a similar temperature until 36°C. However, when the temperature reaches 38°C, the first change is visible as the PV cell temperature is ~1°C below the membrane temperature, whereas the top and bottom glass remain with ~1°C each, below from the PV cell and the top glass respectively. This variation at the end of the experiment in the bottom glass can be related to its thermal gains and losses. Moreover, the MPP behaviour presents a steady trend from 28°C to 34°C. At 36°C, another small decrease is seen on MPP, which can be related to the thermal resistance increment on the top glass, membrane, as well as PV cell temperatures. However, after this, the MPP values keep increasing continuously until the end of the experiment due to the phase change-related increase of reflectance levels. This trend persists until the maximum temperature is reached, similar to the behaviour of 2 % HPC & 1.5 wt. % of GGF membrane samples.

Similarly, no further value changes were observed in the MPP or window components after 30 minutes, thereby concluding the experimental work.

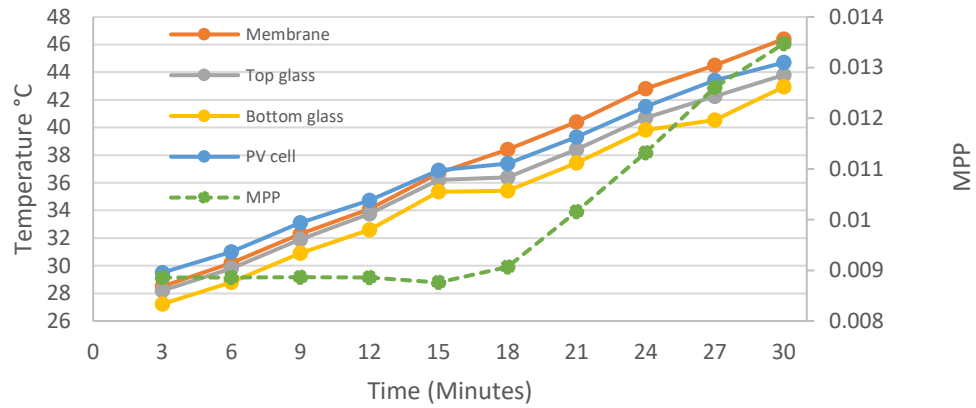


Figure 5.22 Smart window prototype temperature profiles at 2% wt. HPC & 1.5 % wt. GGF under 400 W/m².

5.4 Discussion

Across the smart window characterization, important values were obtained and presented; however, an additional comparison between the smart window prototypes should be made to consider the differences among the membrane samples and the way they affect the electrical performance of the device. Table 5.2 presents the I_{sc} , V_{oc} , η and MPP values for 2% wt. HPC & 1.5 % wt. GGF, and 6% wt. HPC & 1.5 % wt. GGF at 400W/m², where V_{oc} shows 1% of variation, I_{sc} 22%, η 15.6% and MPP 24% from 2% wt. HPC & 1.5 % wt. GGF to 6% wt. HPC & 1.5 % wt. GGF, respectively.

Table 5.2. Smart window electrical values comparison at 400 W/m².

Temperature 46 °C	Power output at 400 W/m ²	
	2% wt. HPC & 1.5 % wt. GGF	6% wt. HPC & 1.5 % wt. GGF
I_{SC}	0.0280	0.0359
V_{OC}	0.4909	0.5
η	3.6%	4.8%
MPP	0.0102267	0.013472

On the other hand, Table 5.3 shows the results for the 2% wt. HPC & 1.5 % wt. GGF, and 6% wt. HPC & 1.5 % wt. GGF at 700W/m². The values differences are 23%, 0.2%, 27.4% and 23.2% for *I*_{sc}, *V*_{oc}, η and MPP, respectively. In addition, low efficiency values can be related due to the non-uniformity of light source affecting how the membrane changes phase, thus impacting energy production and the fact that it cannot reach a higher temperature than 46°C at 400 W/m² and 50 °C at 700W/m². Therefore, the samples also cannot reach the higher reflectance levels necessary to get more rays into total internal reflection to produce more energy.

Table 5.3 Smart window electrical values comparison at 700 W/m².

Power output at 700 W/m ²		
Temperature 50 °C	2% wt. HPC & 1.5 % wt. GGF	6% wt. HPC & 1.5 % wt. GGF
<i>I</i> _{SC}	0.0498	0.0650
<i>V</i> _{OC}	0.4989	0.5
η	3.7%	5.1%
<i>MPP</i>	0.018089788	0.024882

To sum up, 6% wt. HPC & 1.5 % wt. GGF performs better than 2% wt. HPC & 1.5 % wt. GGF, as was expected, offers better optical, thermal, and electrical values due to the quicker phase change, higher reflectance and offering lower transmittance levels to control daylight.

5.5 Conclusions

An indoor optical, thermal, and electrical characterization for smart window prototype was done in this chapter. Firstly, the smart window prototype was characterized to understand its behaviour as a solar concentrator, comparing the single PV cell measurement versus the smart window with the white optics 97% reflective layer. Results show that differences between single-cell and smart window prototype were 5%, 8% and 6% for 170 W/m², 400 W/m² and 700 W/m², respectively, with an average value for all of 6.3.

A smart window prototype was tested using 2 wt. % HPC & 1.5 wt. % GGF and 6 wt. % HPC & 1.5 wt. % GGF to examine the performance of the device using different membrane concentrations. On the one hand, 2 wt. % HPC & 1.5 wt. % GGF prototype shown clear state short circuit average of ~ 0.021 A at 400 W/m^2 compared to ~ 0.038 A at 700 W/m^2 showing 80% of improvement, whilst at light scattering had average values of ~ 0.027 A at 400 W/m^2 and ~ 0.049 A at 700 W/m^2 representing 81 % of improvement. In clear state, power curve value at 400 W/m^2 average was ~ 0.008 W, and at 700 W/m^2 was ~ 0.014 W having a 75% improvement. In light scattering state at 400 W/m^2 the highest value was 0.010 W, and at 700 W/m^2 highest value was 0.018 W having 44% of improvement. On the other hand, 6 wt. % HPC & 1.5 wt. % GGF prototype presented Improvement of 82% comparing clear state short circuit average value against the maximum light scattering value, being ~ 0.035 A and 0.064 A, respectively. Power output improvement was 71% from a clear state average value of ~ 0.014 A to 0.024 A at the highest light scattering achievable.

This characterization was done after smart window materials characterisation, membrane development and raytracing validation, aiming to provide evidence of the smart window versatility and how the device can change its properties to adapt to different irradiations levels and the response to environmental temperature. Nevertheless, this prototype has been tested under indoor controlled conditions only; therefore, further outdoor testing should be done to continue with the device's analysis and development to provide more evidence about how it will perform under outdoor conditions. In this way, accomplishing the chapter 3 methodology steps, everything is set to begin with outdoor testing in the following chapter.

Chapter 6

Design, fabrication, and outdoor testing of smart window prototype for electricity generation and daylight control

This chapter evaluates the outdoor performance of a novel smart window system that automatically controls the incident solar radiation for indoor daylight, passive heating requirement and onsite electricity generation. This novel device is made of low iron optical glass, solar PV cells and a low cost thermotropic switchable layer. Experimental settings for this experiment were defined by three different south-facing angle inclinations 30°, 60° and 90°, using another window as a reference to determine the smart window performance. Temperatures in the smart window components, light transmittance and power output were examined throughout each experimental test.

6.1 Smart window outdoor testing

Once the membrane characterisation, ray tracing validation and indoor characterisation of the smart window prototype were done, it was proceeded to

the outdoor testing to evaluate its performance in an outdoor environment. These experiments were undertaken for three summer days at the Energy Technologies Building (ETB) in the University of Nottingham, U.K. The developed experimental board and the smart window prototype with 6 wt. % HPC & 1.5 wt. % GGF membrane and the reference window in three different inclination angles, 30°, 60° and 90° were used for the experiments.

6.2 Smart window with membrane vs reference window at 30° inclination

According to the methodology outlined in chapter 3, the outdoor testing began with mounting the experimental board with an inclination of 30°, where irradiance and window components temperatures were recorded. Figure 6.1 shows the irradiance levels captured by the Pt, Pr and Ps mounted on the experimental board across the day from levels below 100 W/m² to more than 1000 W/m² at solar noon, then going down in the afternoon as the sun goes down. On one hand, it is worth to note that at the beginning of the experiment, the sun comes up from the east, making Pr to receive more direct light than Ps, although irradiance values for Pr and Ps showed few differences. On the other hand, at the end of the experiment, when the sun is going down on the west, the irradiance values for Ps are slightly higher than Pr due to the horizontal position of the PV cell in the reference window blocking the pyranometer, while nothing is blocking the sun on the smart window. Moreover, Pr irradiance was consistent across the rest of the experiment with a similar trend as Pt values. Ps values presented a similar trend as Pt with expected differences due to their locations; nevertheless, as the sun was reaching its highest point of the day, the values got closer. The first phase change occurred around 11:30, then additional phase changes were observed at 13:40 and 14:54. Irradiance Ps values dropped because the sunlight was blocked by the light scattering state of the membrane. To support this explanation, the temperature profile of the smart window cover glass (Ts) in Figure 6.2 can be used. Because Ts

is highly related to the thermotropic membrane temperature, when the phase change is happening, values presented a fluctuation from $\sim 40^\circ\text{C}$ to $\sim 50^\circ\text{C}$, thus promoting heat gains in the glass, hence triggering the light scattering state.

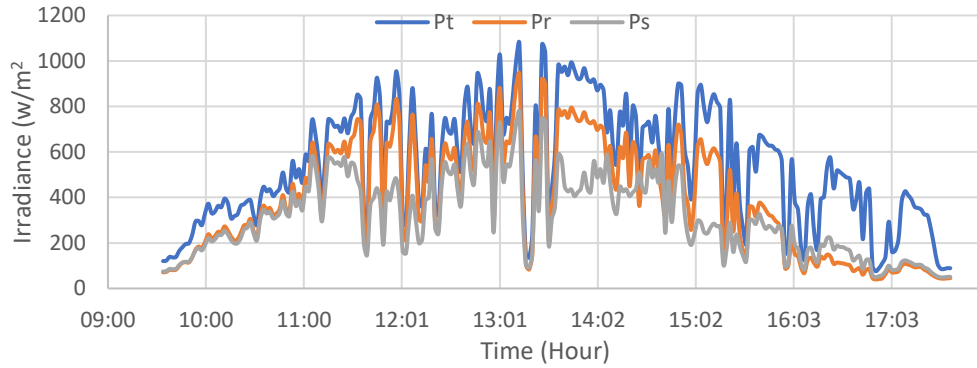


Figure 6.1 Irradiance levels on experimental board pyranometers at 30° .

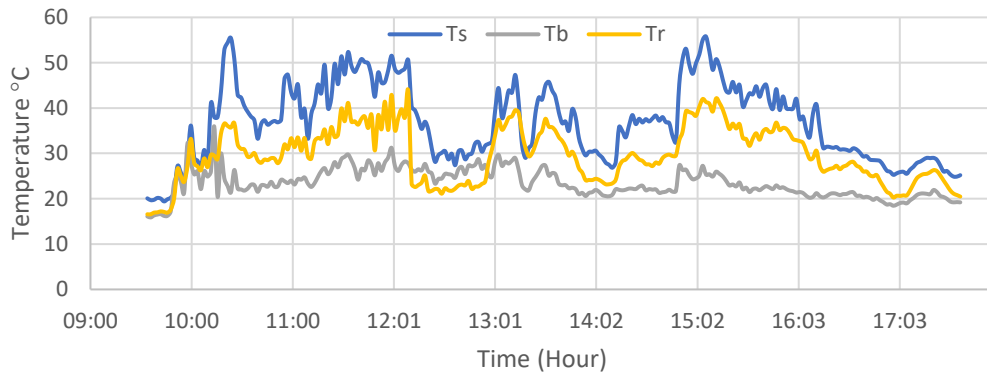


Figure 6.2. Temperature profile for smart window and reference window glass covers and ambient temperature.

Figure 6.3 presents the temperature profile of the TPVs, TPVr and their respective efficiencies η_{PVs} and η_{PVr} . Throughout the experiment, TPVs presented slightly higher values in comparison to the TPVr. This difference can be related to the light trapped by the effect of total internal reflection. The direct light hits the cells and the use of a membrane, which is proven to have heat absorption properties, promotes heat transfer from the glass to the PV cell. On the other hand, TPVr recorded lower values than TPVs because it is only the glass under the sun and ambient temperature with the thermal losses and gains. Regarding efficiencies, η_{PVr} recorded better performance at the beginning of the experiment. This

behaviour is associated with how the sun comes up from the east and goes down on the west, hitting directly first the reference window until noon where the difference is reduced, and the closest values of η_{PVr} and η_{PVs} are reached when the phase changes were achieved starting around 11:30, 13:40 and 14:54. Additionally, the experiment average efficiencies for η_{Pr} and η_{Ps} were 16% and 10%, respectively.

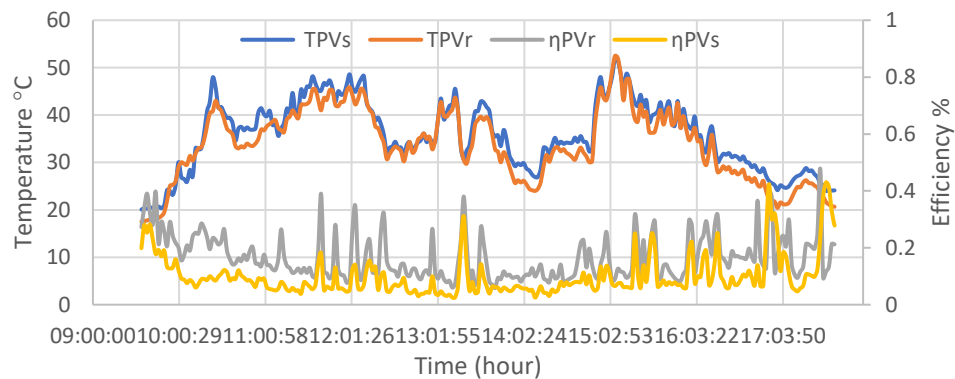


Figure 6.3 Temperature vs efficiency of experimental board components at 30°.

Figure 6.4 shows the variation of maximum power generated by the reference (R_w) and smart window (S_w) in relation to the temperature recorded on the day of the test. At the beginning of the experiment, a gap is observed in R_w from $\sim 17^\circ\text{C}$ to $\sim 19^\circ\text{C}$ and for S_w from $\sim 21^\circ\text{C}$ to $\sim 24^\circ\text{C}$. This is related to the first I-V tracker measurements before the sun illuminates the windows. Lower values are recorded repeatedly with a sudden leap into higher values, and then this trend continues increasing continuously as the temperature rises. The R_w values incremented until $\sim 35^\circ\text{C}$, where the values started to record similar values in a flat trend line with maximums over 0.062 W. Similarly, the S_w also presented a gap at the begin of the experiment in the range of $\sim 21^\circ\text{C}$ to $\sim 24^\circ\text{C}$, where the same explanation as the R_w applies to understand this issue. From $\sim 24^\circ\text{C}$ to $\sim 30^\circ\text{C}$, a flat line appears because the smart window is in clear state. Although some values are lower than the line, this is related to the irradiance variations across the day. In addition, from $\sim 30^\circ\text{C}$ to $\sim 40^\circ\text{C}$, MPP values were increasing continuously, the temperature range where the phase change occurs. Finally, after 40°C , a flat line trend appears, recording

the highest value of $\sim 0.038\text{W}$. Mixed values from $\sim 0.027\text{ W}$ to $\sim 0.037\text{W}$ can be seen due to the irradiance fluctuations and repercussions of those in the reflectance level of the thermotropic membrane inside the smart window prototype, when exposed to the outdoor environment, is prone to quick temperature changes.

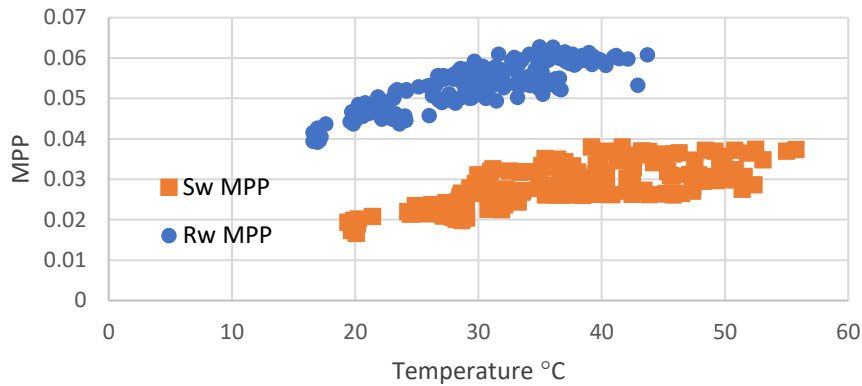


Figure 6.4. Power output distribution across the irradiance levels at 30° .

6.3 Smart window with membrane vs reference window at 60° inclination

The second configuration for the experimental board used the same with a 6 wt. % HPC 1.5 wt. % GGF thermotropic membrane. The only change was the inclination angle from 30° to 60° . The pyranometer on top showed a bigger difference compared to RW and SW during the 30° angle experiment. This behaviour is a direct result of the board getting closer to the right angle (90°) position, where less sunlight will reach the pyranometers behind the SW and RF. At the same time, it must be remembered that the PV cell on RF is in a horizontal position; therefore, the pyranometer will receive shadow overcast at certain sun positions during the day. Ps recorded four phase changes around 11:00 to 12:30, 12:44 to 13:16, 13:31 to 13:56 and 14:12 to 15:00. In three-time lapses Ps recorded higher irradiance levels than Pr. The first was at the beginning of the experiment because although the sun comes up from the east at 60° Pr it is not receiving the same amount of

sunlight as at 30° and the PV cell is blocking a considerable amount of sunlight. Ps values are lower than the Pr in the middle of the experiment, due to the rise of temperature promoting the phase change in the thermotropic membrane blocking the sunlight coming to the Ps. However, around 13:00 Ps values became higher than Pr, this can be related to the reduction in the irradiance Pt values recorded around 13:16 to 13:31 and 13:45 to 14:12, this being related to a cloud passing by lowering the irradiation level. Therefore, the reduction of irradiance levels caused a drop in smart window temperature values, regaining transparency whilst the sun is around at the highest position during the day. Additionally, the reference window PV cell should be considered, which blocks more sunlight while the sun is passing through the higher positions of the day. Details of the latter explanation can be seen in Figure 6.5. In figure 6.6 temperature readings presented an average of ~51°C, 47.8°C, 47.9°C, 48.6°C for 11:00 to 12:30, 12:44 to 13:16, 13:31 to 13:45 and 14:12 to 15:00 time-lapses respectively, supporting the conditions to raise the temperature and achieve the phase change at the same lapse time where the smart window reported them according to the Ps values. Tr showed a similar trend but with lower values than Ts across the experiment, and Tb recorded an average temperature of 24.3°C.

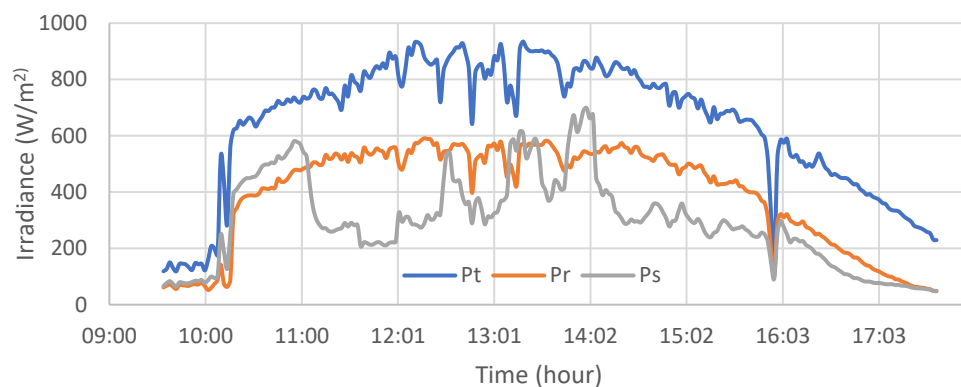


Figure 6.5. Irradiance levels on experimental board pyranometers at 60°.

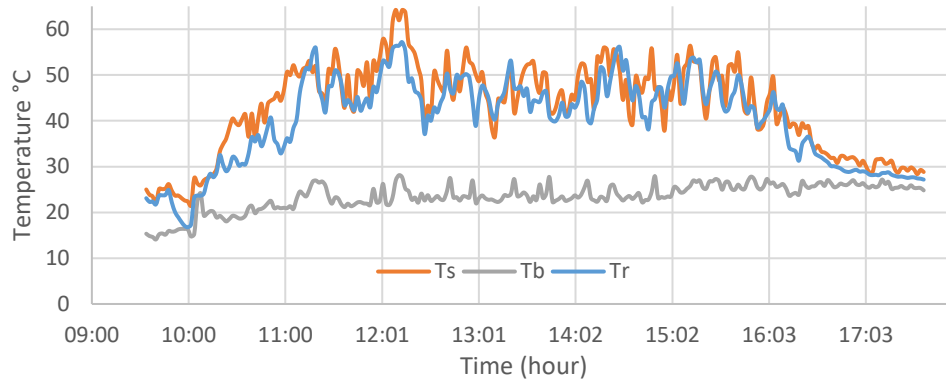


Figure 6.6 Temperature profile of experimental board components at 60°.

In Figure 6.7 TPVs and TPVr are shown with their respective efficiencies η_{PVs} and η_{PVr} . In this experiment TPVr recorded lower values than the TPVs, with less than 30° from 9:30 to 12:30, presenting a maximum value of $\sim 40^\circ\text{C}$, with a similar trend as the TPVs, but with lower values during the last part of the experiment. The factors causing the low temperature values are related to the change of inclination, radiating less light directly onto the PV solar cell; hence less temperature is gained, until the sun is passing through the higher positions of the day and the temperature increases. In comparing PV efficiencies, η_{PVr} had better performance through the whole experiment than η_{PVs} , showing less thermal resistance due to the lower temperature recorded in the PV cell, promoting better efficiency. Although η_{PVr} and η_{PVs} have similar trends, η_{PVs} had a lower performance at the beginning and the end of the experiment, however it presented better efficiency values when phase change was achieved between 11:00 to 12:30, 12:44 to 13:16, 13:31 to 13:56 and 14:12 to 15:00.

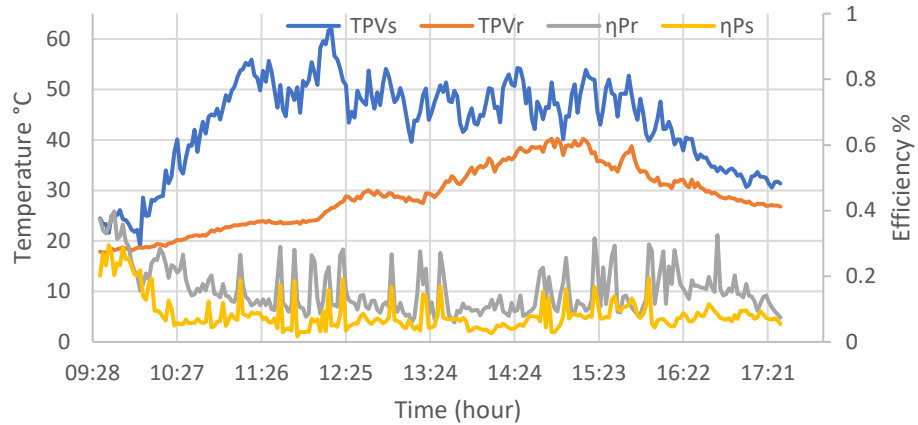


Figure 6.7. Temperature vs. efficiency of experimental board components at 60°. Figure 6.8 shows the R_w and S_w variation of maximum power generation at 60°. R_w presents an increasing trend as the sun goes up from $\sim 15^\circ\text{C}$ to $\sim 30^\circ\text{C}$ where a small flat trend of values starts at $\sim 35^\circ\text{C}$ ending at $\sim 40^\circ\text{C}$. Then preceded by a fuzzy trend with mixed values from $\sim 0.040\text{ W}$ to 0.060 W , this one related to the variation in the irradiation levels at the middle of the experiment followed by a flat trend with the highest value $\sim 0.062\text{ W}$. In addition, fuzzy mixed values from $\sim 0.040\text{ W}$ to $\sim 0.060\text{ W}$ related to the sunlight variations across the experiment were recorded. On the other hand, S_w showed a maximum MPP value with 0.043 W , and an increasing trend from $\sim 20^\circ\text{C}$ to 30°C . Afterwards, a flat trend appeared very similar to R_w followed by a fuzzy trend with mixed values from 0.021 W to 0.040 W from $\sim 35^\circ\text{C}$ to $\sim 45^\circ\text{C}$. Later, a fuzzy trend with mixed values appeared from 0.024 W to 0.041 W from $\sim 35^\circ\text{C}$ to $\sim 45^\circ\text{C}$. This trend was mainly caused by the change in reflectance levels while the smart window is in light scattering state due to the irradiance levels variations.

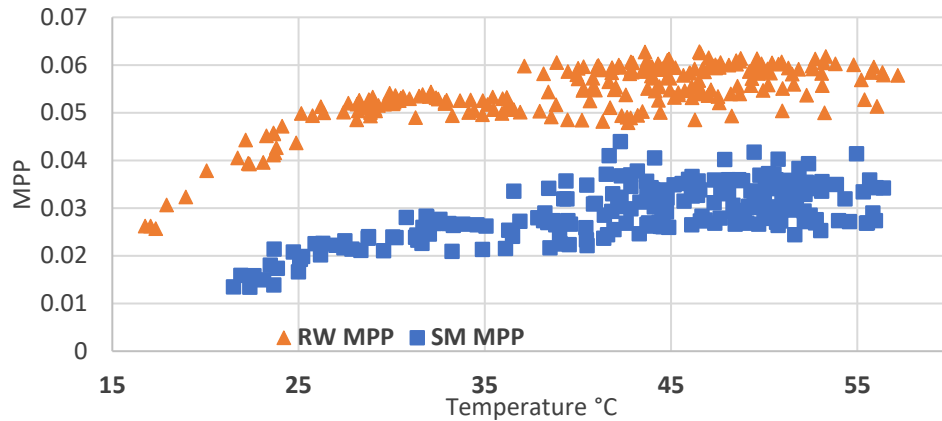


Figure 6.8. Power output distribution across the irradiance levels at 60°

6.4 Smart window with membrane vs reference window at 90° inclination

The third configuration of the experimental board was 90° of inclination, which is the closest condition to the regular building integration as a window or façade. Details of this last experiment are presented in Figure 6.9, where half of the day, it was a clear sky with some cloudiness appearing after 14:00 and being intermittent until the end of the experiment. Pr and Pt pyranometer presented different values at the beginning of the experiment due to the new inclination angle; however, as the sun reached the solar noon, more light radiated directly on Pr, leading to closer values. On the other hand, Ps began with a similar trend as Pr, but after 10:00 started to receive more light as the sun came up, however, a decrease of irradiance values as seen around 10:48. This was due to fact that the switching point temperature of the thermotropic membrane was achieved lasting until 14:42 approximately, and then to start again around 14:50 until 15:20. After these phase change events, the temperature dropped, and the smart window was not able to reach the phase change and kept fluctuating until the end of the experiment. To complement the irradiance interpretation, the temperature profile of the smart window, reference window and ambient temperature are shown in Figure 6.10. Ts values kept increasing from 9:30 to 10:40, and then fluctuating in the range of

~40°C to ~50°C until 14:00 triggering the phase change which was recorded by the pyranometers in Figure 6.9. Tr presented lower values than Ts but with a similar trend. Tb also presented a similar trend as Tr but with lower values across the experiment, reporting an average value of 24.7°C.

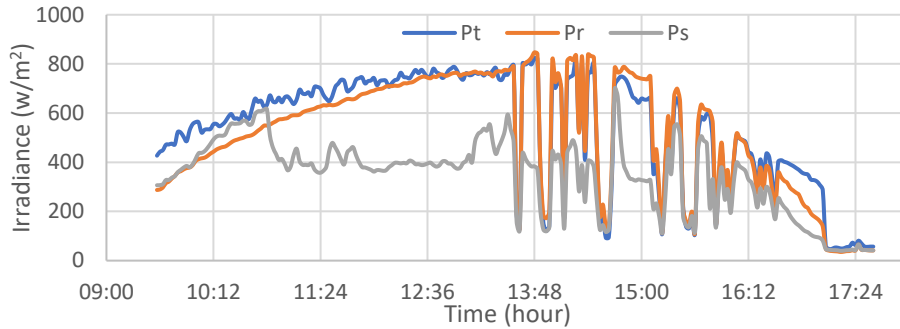


Figure 6.9. Irradiance levels on experimental board pyranometers at 90°

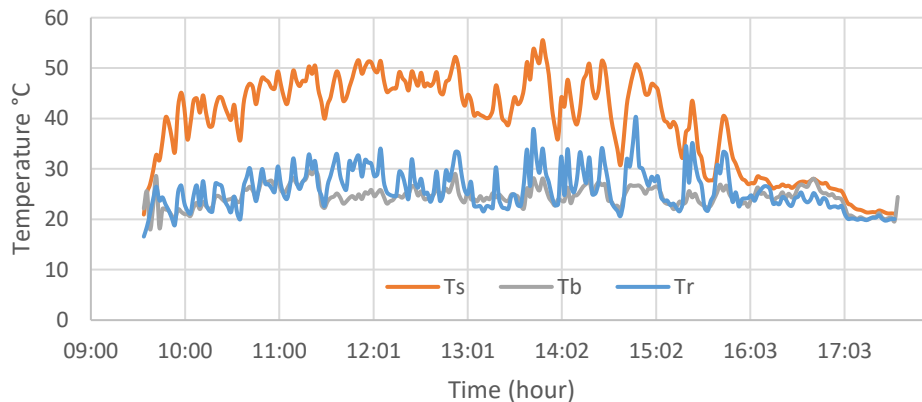


Figure 6.10. Temperature profile of experimental board components at 90°

In Figure 6.11, TPVs recorded higher values than TPVr from 9:30 to 15:00. Afterwards, the values got closer until the end of the experiment. TPVr recorded a temperature range from 20°C to 24°C from 9:30 to 12:20, having there the most consistent irradiance values of the experiment and matching the same time lapse where Ps recorded the phase change. Due to this, the highest efficiency peaks can be seen in this part of the graph, being conjugated the high irradiation levels with a low temperature in PV cell promoting high-efficiency levels. Similar values were recorded around 14:50 until 15:20, where again the phase change occurred due to high irradiance levels. Although η PVs had lower performance through the whole

experiment than η_{PVr} , part of this issue can be related to overheating of the PV cell, causing lower performance. Furthermore, η_{PVr} and η_{PVs} recorded similar trends, η_{PVs} closest efficiency values to η_{PVr} were achieved when phase change occurred from 9:30 to 12:20 and from 14:50 until 15:20.

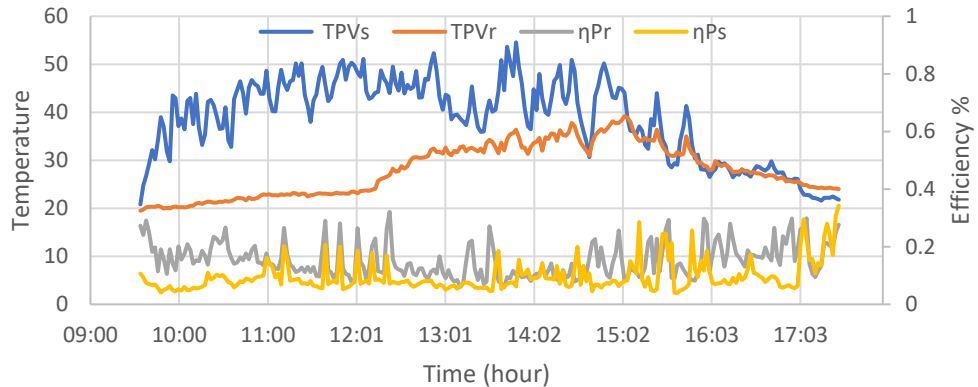


Figure 6.11. Temperature vs. efficiency of experimental board components at 90°

The variation of maximum power generation at 90° of inclination is presented in Figure 6.12, where MPP values for R_w and S_w shown the most significant difference in the temperature range. R_w presented temperature range from 20°C to 35°C , with only two measurements outside of this range, one at 37°C and the other one at 40°C which can be found in Figure 6.10 as the higher peaks in T_r at 13:44 and 14:50. The rest of the measurements are concentrated in the temperature range of 20°C to 35°C , however, presenting an increasing trend as the temperature rose during the experiment with a maximum MPP value of 0.087W. On the other hand, S_w presented a steady increasing trend from the beginning to the end of the experiment, with only one fuzzy mixed trend of 0.21W to 0.039W from 35°C to 45°C . This trend was related to the achieved phase change. Fluctuations then reduced this trend until the end of the temperature range at 50°C , with a maximum MPP value of 0.043W.

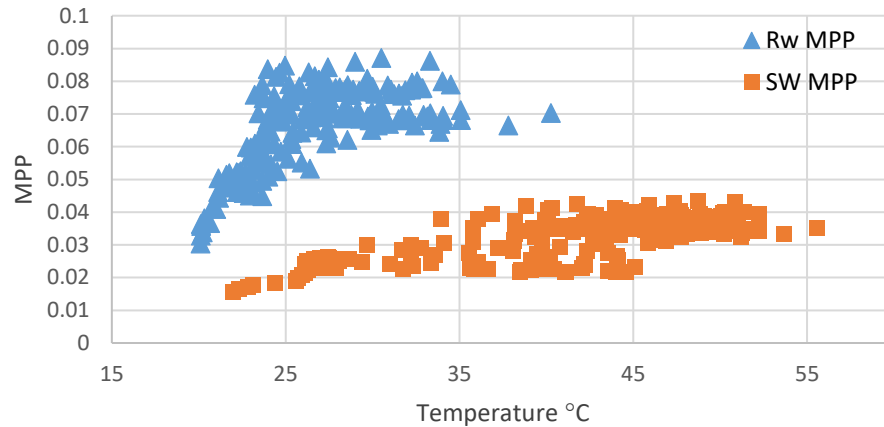


Figure 6.12. Power output distribution across the irradiance levels at 90°

6.5 Discussion

According to the irradiance and temperature tests in this study, the smart window prototype represents an opportunity for offsetting the cooling and lighting needs of a building because it had proven to block the incoming light from 800 W/m² to 200 W/m² when phase change was achieved. It has also shown high irradiance values while it is in a clear state, allowing the light to pass through it and effectively reducing the need for artificial light in indoor spaces. Additionally, this device is self-controlled. It does not need a control to be activated or turned off, which can be considered a benefit of smart technology. In contrast, the smart window presented lower efficiency and power output values when compared against the reference window. This can be linked to the thermotropic membrane which has a maximum of 41 % of reflectivity according to the values obtained from chapter 4. Additional overheating issues were observed, signalled by the higher PV cell temperature profiles of the smart window PV cell in comparison to the reference sample. Therefore, a gap for further work is left here to improve the membrane's reflectance level and control any temperature issue related to the total internal reflection and energy production.

6.6 Indoor vs outdoor testing

A direct comparison between indoor and outdoor testing was made to understand the differences in the performance of the smart window depending on the environment. Since the membrane characterisation stage, the switching temperature of HPC was given and validated through DSC, liquid and membrane tests in the UV-spectroscopy, whereby similar results were obtained at indoor and outdoor testing. Switching points observed after 40°C, helped to confirm that the material responds similarly in different environments.

On one hand, the Indoor testing of the 6 wt. % HPC 1.5 wt. % GGF at 400 W/m² presented the highest MPP of 0.01347W at 46 °C and at 700 W/m² an MPP of 0.02488W at 50°C. On the other hand, outdoor testing presented the highest MPP of 0.037W at 30° inclination, 0.043W at 60° and 0.043W at 90°, all of them within the temperature range of ~40°C-to ~55°C when the irradiation levels were above 800 W/m². These differences can be addressed since the samples did not achieve full light scattering due to limitations of the light source to reach higher temperatures. In this regard, in chapter 3 the HPC heating range from 20°C to 55°C was set and, in the UV-spectroscopy reflecting test, the highest reflection achieved was at 55°C, hence the highest energy production. Moreover, the non-uniform light source, the overheating of the PV cell and the lack of inclination angle 0° affect the overall optical efficiency of the device by up to 25%, leading to varying results.

6.7 Summary

A smart window with a thermotropic membrane made by 6 wt. % HPC 1.5 wt. % GGF and distilled water was tested under outdoor conditions with a south-facing orientation at 30°, 60° and 90° of inclination. The experiments at 30° showed a power output difference of 48.6% in the average energy generation for the R_w over the S_w with the highest values of 0.062W and 0.037W, respectively. The smart window at 60° experimented an average power output difference of 46.4% between R_w and S_w , with the same maximum value 0.062W for R_w and 0.043W

for Sw. The 90° inclination test presented an average of the biggest power output difference between the three inclinations being 55.4% the highest MPP values of 0.087W and 0.043W for RW and SW, respectively. On the other hand, the temperature profile test showed that the Ts had higher temperature values in all the tests against the Tr, which at 30° presented the closest values to Ts but in 60° and 90° values were different. For its part, Tb presented the lowest values in the three tests. Efficiency represented by η_{PVr} and η_{PVs} for reference and smart window respectively, showed that η_{PVs} recorded the closest values to η_{PVr} when the phase change was achieved, namely when the device was at 40°C or more in the three different inclination tests.

Overall, the results showed that the outdoor performance of this novel solar concentrator with an automated solar control allows sunlight to pass through in the morning and the evening but blocks the sun when irradiation levels surpassed the 600 W/m², thus offering indoor lighting and energy savings and to controlling passive heat gains inside a building during the day. In contrast, the energy production and device efficiency still need to be improved, according to what a device requires to be integrated into a building to meet the net-zero aim. In this regard, improving the reflectance level in the thermotropic membrane will impact significantly the way it produces energy. The current maximum reflectivity achieved was ~40. However, to produce a more efficient device, the reflectivity should be close to 90%.

To conclude, this chapter summarises the whole work done from membrane materials characterisation until outdoor testing, utilising all the data and information gathered at each chapter to produce this final one. However, this is not the final chapter of this thesis, the next and final chapter will provide the overall conclusions of the thesis and a outlook for future work.

Chapter 7

Conclusions and future work

7.1 Development and thermal and optical characterisation of the membrane

The characterisation of the thermotropic membrane detailed important characteristics of the materials tested e.g., the HPC phase change temperature validation, which according to the references used in the literature temperature required to achieve the phase change should be 40°C. The analysis of heat capacity of the HPC liquid, HPC & GGF and HPC & ethulose membranes and the hysteresis between the cycles, all of these by testing samples in the micro-DSC. In addition, FTIRs test showed that the response of the materials to the IR spectrum, broadening the approach of how the materials perform beyond the visible light spectrum and how GGF and ethulose presented different absorption bands in the IR spectrum. ESEM pictures showed a microscopy level of the membranes leading to the state that all the four samples tested presented a homogeneous blend at 100 µm and 50 µm. Moreover, a long-lasting test on GGF and ethulose membranes was carried out to determine their behaviour when exposed to the indoor environment due to a crack in the window, leaking or sealing problems, showing that GGF membrane reported membrane shrinkage after the 3rd week and got a yellowish colour, whereas the ethulose membrane remained the same in the four weeks of the experiment. Lastly, the UV-spectroscopy, where all the data gathered in the previous characterisation steps was validated, like the hysteresis cycles detected in the DSC test, which were recorded too in transmittance and reflectance tests, and the switching points for HPC, HPMC and PNIPAM, which all of them recorded similar transition values as the literature review reported.

For the conclusions of the membrane development and characterisation, the following results were highlighted:

- The smart window is a versatile device that can adapt to different environments.
- The use of different polymers and gelling agents broads the way that the smart window can be switched to fulfil different daylight and heat gains requirement for building integration.
- The easy use of different matrix for the selected polymers gives an opportunity to expand the scope of the thermotropic membrane used in the smart window.
- The thermotropic membrane offers more than simple daylight control; depending on the gelling agent, heat gains can be controlled too.
- PNIPAM offers an excellent way to improve the smart window reflectivity, hence the energy production, however, with a higher cost compared to HPC.
- Ethulose, as a matrix for the membrane, offers better results in retaining water against the indoor environment when it is exposed.
- The 6% wt. HPC & 1.5 % wt. GGF blend showed the best balance between high transmittance in clear state and high reflectivity in light scattering, environmentally friendly and accessible price.
- Although HPMC recorded the lowest transparency levels at a clear state and the lowest reflectance level, this polymer offers a wider phase change. This related to human indoor conditions represents a smoother change in the daylight coming on and off by the smart window avoiding the glare generated by a sudden change, therefore not being negligible at all.

This materials characterisation for the thermotropic membrane presented a deeper understanding about how these polymers, gelling agents performed. Gathering results and data from the spectroscopy with transmittance and

reflectance to heat capacity with DSC, To infrared spectrum with FTIRs tests. ESEM pictures helped to evaluate the chemical blend of these material in a nano scale and how they will interact integrated in a smart window prototype tested in the UV-VIS spectroscopy.

7.2 Indoor characterisation of the smart window

The Indoor testing and laboratory components characterisation reported in detail the evaluation of the single elements comprising the smart window prototype to the device's performance. Single cells used for these experiments were characterised to produce two smart window prototypes with the same conditions. In addition, the smart window concept was validated by comparing a single cell against the smart window, reporting only 6.3% of difference, which was mainly caused by the lab equipment limitations and the inclination angle of the smart window. Afterwards, the rest of the smart window components were analysed to produce a ray tracing model and predict the device's performance and proceed to the validation through a direct comparison against the indoor test. An 8% of discrepancy between modelling and indoor results was achieved, which provided confidence to start the smart window indoor test with the thermotropic membrane. For the smart window with the thermotropic membrane testing results showed that as the HPC concentration increased, the light transmittance values in clear state were not affected but in light scattering more light was blocked, going from 48% and 37% of transmittance for 2 wt. % HPC 1.5 wt. % GGF and 6 wt. % HPC 1.5 wt. %. Additional results are highlighted here:

- 6 wt. % HPC 1.5 wt. % GGF membrane offers a good balance between high transmittance in clear state and up to 41% of reflectivity at light scattering state.
- At $400\text{W}/\text{m}^2$. Voc shows 1% of variation, Isc 22%, η 15.6% and MPP 24% from 2% wt. HPC & 1.5 % wt. GGF to 6% wt. HPC & 1.5 % wt. GGF, respectively.

- At 700W/m^2 . The values differences are 23%, 0.2%, 27.4% and 23.2% for I_{sc} , V_{oc} , η and MPP, respectively.
- Power output improvement was 71% from a clear state average value of $\sim 0.014\text{ A}$ to 0.024 A at the highest light scattering achievable.
- The development level of the smart window prototype was enough to proceed with the outdoor testing.

Through the indoor characterisation of the smart window components, the device went under controlled environment testing, validating the concept and analysing several aspects of the prototype, thereby obtaining enough data to proceed with the next stage in this research, outdoor testing.

7.3 Outdoor characterisation of the smart window

Once the membrane and smart window prototype characterisation and testing were completed, the last part of this research was undertaken, which included the outdoor testing and development of an experimental board to cover the most important aspects in the smart window performance and its data collection through the testing. Under the three different angle inclinations the reference window and the smart window recorded similar trends but with different values. Being the smart window the one presenting lower values, however, when the phase change occurred in all the experiments the MPP and efficiency values got closer. Therefore, concluding that when the smart window is on clear state offers daylight and heat passive gains saving in indoor lighting and heating loads, whilst when the phase change is achieved offers solar control and helps to offset the cooling loads. Additionally, it is important to note that the PV cell of the smart window reported higher values than the reference window; this is related to the thermotropic membrane, which had proven in the previous chapters to have heat absorption, thus presenting lower efficiencies and lower MPP values. Complementary conclusions are listed in the following:

- In low irradiance levels Sw and Rw produced a similar amount of energy; hence the SW is capable of collect enough diffuse light under lower irradiance levels.
- At 30°, the power output difference of 48.6% was found in the average energy generation for the RW over the SW with maximum values of 0.062W and 0.038W, respectively.
- Aat 60° average power output difference of 46.4% with maximum values 0.062W for Rw and 0.043W for Sw.
- The 90° inclination test presented a power output difference of 55.4% with maximum values of 0.087W and 0.043W for Rw and Sw, respectively.
- Temperature is the main factor affecting the smart window's electrical performance since the membrane components are likely to retain heat, thus promoting overheating on the PV cells.

To conclude, the results from outdoor testing showed that although the electrical performance and power output of the smart window cannot be the same as the single PV cell, it can provide excellent daylight and heat control for a building. Future work should focus on membrane reflectance improvement, hence improving the power output of the smart window.

7.5 Further work

Initial recommendations for future work should start by increasing the accuracy of the experimental results. Some limitations in this research were linked to the quality of some lab components like light source, testing rig and PV cells with better efficiencies. The smart window scope can be expanded through the materials research searching for novel materials to be incorporated into it. The development of a original blend of polymer would be one way to improve the efficiency of the smart window, because in this way the polymer can be tailored to suite the smart window needs, and further modifications can be done to provide

solutions to different scenarios. Also, the research in gelling agents can provide better performance of the membrane and the device; therefore, further research should be done to expand this knowledge. Moreover, the thermotropic membrane should be tested on lower temperatures to determine when the temperature drops and if this change affects its performance when temperature is back in the smart window range. The addition of more PV cells, due to the smart window prototype, was developed only with one solar cell attached to one edge but is capable of accepting three more; therefore, its electrical performance will improve, although it will require a proper installation and handling of the prototype. Lastly, improving the sealant in the smart window prototype, will help the way the membrane works under high temperatures when under heat exposure water loss in the membrane can be avoided, although the isolation of the device should not obstruct the PV cell installation. Lastly with all these conclusions and recommendations for further work is concluded this thesis work.

Appendix A: Membrane manual

HPC & GGF membrane synthesis manual



The University of
Nottingham

UNITED KINGDOM • CHINA • MALAYSIA

This manual explains step by step how to produce smart window samples made of HPC and GGF membrane, please make sure that you are familiar with the tools and equipment used in the laboratory to avoid any risk, also be aware of the safety procedures needed to perform any experiment in the laboratory and wear the proper PPE to be allowed to remain working safety at the lab. Then, follow the following steps one by one without skipping any of them to assure that the final product will be reliable to perform any test in the near future.

1. Select the desired concentrations for the blend i.e., 6% HPC 1.5GGF, use the excel document to calculate the concentrations without any error. In the excel sheet fill the “%” cells corresponding to the percentage sought to produce a membrane with correct concentrations. Also fill the “ml.aq” cells corresponding to the amount of distilled water to be used and lastly double check the yellow cells where the final blend concentration is shown. See table 1 for details.

Table 1. Excel file to determine weight concentrations.

% GGF and % HPC				made on					
	%	ml aq.		%					
GGF	3	10	50	50 % dilution	% of % is	1.5	1.50 %		
HPC	12	10	50	50 % dilution	% of % is	6	6.00 %		
		20							

2. With concentrations selected proceed to fill each beaker (one for HPC and one for GGF) with distilled water according with the excel sheet blend. Figure 2 shows how the ml. of water are determined in a graduate cylinder.



Figure 2. Glass cylinder ready to be filled with distilled water.

3. Bring out the chemicals*(HPC & GGF) gather small containers to handle the chemical properly and set the digital scale to zero to get trustworthy measurements and weight the selected amount using the digital scale. Figure 3 shows the HPC, GGF boat cup and digital scale from left to right respectively.

* Any chemical use in the laboratory must be kept in a safe place to avoid any dangerous situation regardless is hazardous or not.



Figure 3. Membrane components, blending tools and scale.

4. Weight the selected amount of HPC & GGF carefully pouring some into a smaller container the doing it from the upper side of the scale as the Figure 4 shows.

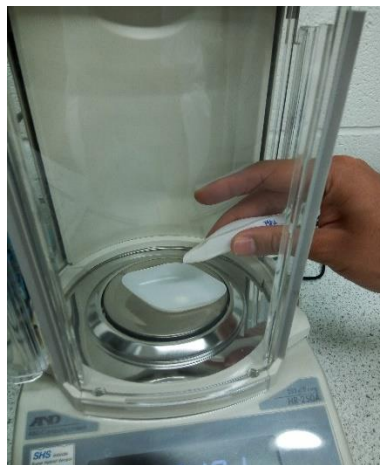


Figure 4. HPC being pour into the boat cup to determine weight.

4. With the HPC & GGF samples ready proceed to mark them to avoid any risk of confusion.



Figure 5 HPC and GGF samples weighed ready to be blended.

5. Using distilled water and the graduated cylinder fill the beakers corresponding to the amount of ml. selected in the excel sheet to produce the desired membrane as shown in Figure 6.



Figure 6. Graduated cylinder filled with distilled water.

6. Plug and turn on the SciQuip hotplate/stirrer, set the desire temperature to initiate the heating, put the magnetically charged stirrer into the beaker with distilled water and cover the top with conical flask, details of this procedure are shown in Figure 7.

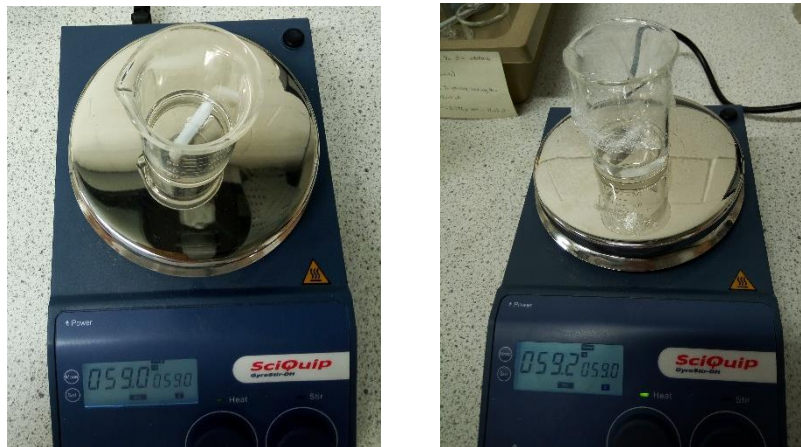


Figure 7. SciQuip hot plate with beaker and the magnetic stirrer.

7. Adjust the temperature to 60°, stir to 200 and wait for 3-5 minutes then add slowly the HPC uncovering the conical flask and covering again when finish. In addition, between each pouring wait until the material is dissolved to avoid any

further complications. Leave the sample stirring for 12 hours to get proper HPC sample hydration and dissolution.

For GGF set the temperature to 75°, stir to 200 and wait for 3-5 minutes then add slowly the GGF uncovering the conical flask and covering again when finish, is important to note that pouring HPC is easier than GFF, so be carefully trying to pour big GGF quantities .Also when is finished never remove the GGF beaker from the hot plate because, it will turn into solid gel and the following steps are made using the hot plate. Figure 8 shows how to pour the GGF/HPC inside the beaker carefully.

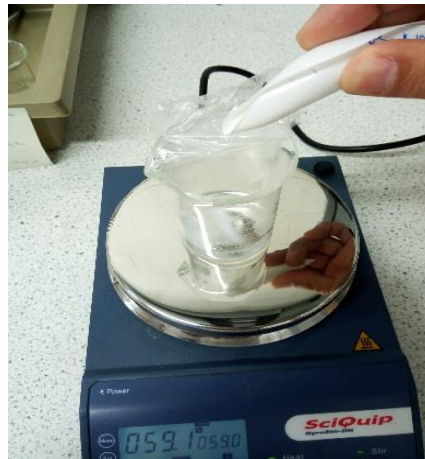


Figure 8. HPC being poured into the beaker while stirring.

-Colour changes can be experimented because of the high temperature, thus HPC can change to milky colour due to its characteristics. Also is recommendable to prepare first the HPC and when is finished leave it without heating for 5 min stirring at 100, then prepare GFF, all of this because the next step will be when GFF is ready.

8. With both samples ready (HPC & GGF) proceed to fill the graduated pipette with HPC and release it drop by drop carefully in the GGF beaker at 250 stirring and 75°. Figure 9 show the graduate pipette ready to be blended with the GGF.



Figure 9. The use of graduate pipettes for HPC and GGF blending.

9. When the HPC & GGf are well mixed set the stir on 200 and turn off the heating, leave it to rest 10-30 min and the proceed to next step.

10. Select the spacer thickness and the glass panes and cast the membrane liquid on it as the picture shows, then use the clips to secure the glass panes and leave it to rest for 2 hours before using it.

References

1. Xia, J., et al., *Comparison of building energy use data between the United States and China*. Energy and Buildings, 2014. **78**: p. 165-175.
2. Abdallah, M., K. El-Rayes, and C. Clevenger, *Minimizing Energy Consumption and Carbon Emissions of Aging Buildings*. Procedia Engineering, 2015. **118**: p. 886-893.
3. Ruparathna, R., K. Hewage, and R. Sadiq, *Improving the energy efficiency of the existing building stock: A critical review of commercial and institutional buildings*. Renewable and Sustainable Energy Reviews, 2016. **53**: p. 1032-1045.
4. Bai, L., et al., *A new approach to develop a climate classification for building energy efficiency addressing Chinese climate characteristics*. Energy, 2020. **195**: p. 116982.
5. Pérez-Lombard, L., J. Ortiz, and C. Pout, *A review on buildings energy consumption information*. Energy and Buildings, 2008. **40**(3): p. 394-398.
6. IEA, *Tracking Buildings*. 2019.
7. Deb, C., et al., *A review on time series forecasting techniques for building energy consumption*. Renewable and Sustainable Energy Reviews, 2017. **74**: p. 902-924.
8. Gholami, H., H.N. Røstvik, and D. Müller-Eie, *Holistic economic analysis of building integrated photovoltaics (BIPV) system: Case studies evaluation*. Energy and Buildings, 2019. **203**: p. 109461.
9. Zhang, X., et al., *Photovoltaic integrated shading devices (PVSDs): A review*. Solar Energy, 2018. **170**: p. 947-968.
10. Hammond, G.P., et al., *Whole systems appraisal of a UK Building Integrated Photovoltaic (BIPV) system: Energy, environmental, and economic evaluations*. Energy Policy, 2012. **40**: p. 219-230.
11. Cerón, I., E. Caamaño-Martín, and F.J. Neila, *'State-of-the-art' of building integrated photovoltaic products*. Renewable Energy, 2013. **58**: p. 127-133.
12. Gholami, H. and H.N. Røstvik, *Economic analysis of BIPV systems as a building envelope material for building skins in Europe*. Energy, 2020. **204**: p. 117931.
13. Vanhoutteghem, L., et al., *Impact of façade window design on energy, daylighting and thermal comfort in nearly zero-energy houses*. Energy and Buildings, 2015. **102**: p. 149-156.
14. Cuce, E., C.-H. Young, and S.B. Riffat, *Thermal performance investigation of heat insulation solar glass: A comparative experimental study*. Energy and Buildings, 2015. **86**: p. 595-600.
15. Cuce, E. and S.B. Riffat, *A state-of-the-art review on innovative glazing technologies*. Renewable and Sustainable Energy Reviews, 2015. **41**: p. 695-714.
16. Mangkuto, R.A., M. Rohmah, and A.D. Asri, *Design optimisation for window size, orientation, and wall reflectance with regard to various daylight metrics and lighting energy demand: A case study of buildings in the tropics*. Applied Energy, 2016. **164**: p. 211-219.
17. Gorgolis, G. and D. Karamanis, *Solar energy materials for glazing technologies*. Solar Energy Materials and Solar Cells, 2016. **144**: p. 559-578.
18. Ihara, T., A. Gustavsen, and B.P. Jelle, *Effect of facade components on energy efficiency in office buildings*. Applied Energy, 2015. **158**: p. 422-432.

19. Jelle, B.P., et al., *Fenestration of today and tomorrow: A state-of-the-art review and future research opportunities*. Solar Energy Materials and Solar Cells, 2012. **96**: p. 1-28.
20. Zhang, Y., et al., *Perovskite thermochromic smart window: Advanced optical properties and low transition temperature*. Applied Energy, 2019. **254**: p. 113690.
21. Tällberg, R., et al., *Comparison of the energy saving potential of adaptive and controllable smart windows: A state-of-the-art review and simulation studies of thermochromic, photochromic and electrochromic technologies*. Solar Energy Materials and Solar Cells, 2019. **200**: p. 109828.
22. Nitz, P. and H. Hartwig, *Solar control with thermotropic layers*. Solar Energy, 2005. **79**(6): p. 573-582.
23. Ikkurtti, H.P. and S. Saha, *A comprehensive techno-economic review of microinverters for Building Integrated Photovoltaics (BIPV)*. Renewable and Sustainable Energy Reviews, 2015. **47**: p. 997-1006.
24. Fossa, M., C. Ménézo, and E. Leonardi, *Experimental natural convection on vertical surfaces for building integrated photovoltaic (BIPV) applications*. Experimental Thermal and Fluid Science, 2008. **32**(4): p. 980-990.
25. Jelle, B.P. and C. Breivik, *State-of-the-art Building Integrated Photovoltaics*. Energy Procedia, 2012. **20**: p. 68-77.
26. Makrides, G., et al., *Potential of photovoltaic systems in countries with high solar irradiation*. Renewable and Sustainable Energy Reviews, 2010. **14**(2): p. 754-762.
27. Jean, J., et al., *Pathways for solar photovoltaics*. Energy & Environmental Science, 2015. **8**(4): p. 1200-1219.
28. (ITRPV), I.T.R.f.P., *International Technology Roadmap for Photovoltaic (ITRPV). 2013 Results*, 2014.
29. (ITRPV), I.T.R.f.P., *ITRPV Ninth Edition 2018 including maturity report 2018*.
30. Varghese, N., et al., *A calorimetric investigation of the assembly of gold nanorods to form necklaces*. Chemical Physics Letters, 2008. **450**(4-6): p. 340-344.
31. L. S. Mattos, e.a., *in Photovoltaic Specialists Conference (PVSC)*. 2012 38th IEEE, 2012 p. pp. 003187–003190.
32. Kayes BM, N.H., Twist R, Spruytte SG, Reinhardt F, Kizilyalli IC, Higashi GS. , *27.6% conversion efficiency, a new record for single-junction solar cells under 1 sun illumination*. . Proceedings of the 37th IEEE Photovoltaic Specialists Conference, 2011., 2011.
33. Dimroth, F., et al., *Wafer bonded four-junction GaInP/GaAs//GaInAsP/GaInAs concentrator solar cells with 44.7% efficiency*. Progress in Photovoltaics: Research and Applications, 2014. **22**(3): p. 277-282.
34. Lechner, P. and H. Schade, *Photovoltaic thin-film technology based on hydrogenated amorphous silicon*. Progress in Photovoltaics: Research and Applications, 2002. **10**(2): p. 85-97.
35. Parida, B., S. Iniyar, and R. Goic, *A review of solar photovoltaic technologies*. Renewable and Sustainable Energy Reviews, 2011. **15**(3): p. 1625-1636.
36. Chopra, K.L., P.D. Paulson, and V. Dutta, *Thin-film solar cells: an overview*. Progress in Photovoltaics: Research and Applications, 2004. **12**(2-3): p. 69-92.
37. Release, F.S.P., *First Solar builds the highest efficiency thin film PV cell on record*. 2014.

38. Lee, T.D. and A.U. Ebong, *A review of thin film solar cell technologies and challenges*. Renewable and Sustainable Energy Reviews, 2017. **70**: p. 1286-1297.
39. Jäger-Waldau, A., *Status of thin film solar cells in research, production and the market*. Solar Energy, 2004. **77**(6): p. 667-678.
40. Haegel, N.M., et al., *Terawatt-scale photovoltaics: Trajectories and challenges*. Science, 2017. **356**(6334): p. 141-143.
41. Green, M.A., et al., *Solar cell efficiency tables (version 49)*. Progress in Photovoltaics: Research and Applications, 2017. **25**(1): p. 3-13.
42. Polman, A., et al., *Photovoltaic materials: Present efficiencies and future challenges*. Science, 2016. **352**(6283).
43. Wang, W., et al., *Device Characteristics of CZTSSe Thin-Film Solar Cells with 12.6% Efficiency*. Advanced Energy Materials, 2014. **4**(7): p. 1301465.
44. laboratory, N.r.e., *Best research cell efficiency*. 2017.
45. Manser, J.S., J.A. Christians, and P.V. Kamat, *Intriguing Optoelectronic Properties of Metal Halide Perovskites*. Chemical Reviews, 2016. **116**(21): p. 12956-13008.
46. Hamers, L., *"Perovskites power up the solar industry"*. Sciencenews.org., , 2017.
47. Green, M.A., et al., *Solar cell efficiency tables (Version 45)*. Progress in Photovoltaics: Research and Applications, 2015. **23**(1): p. 1-9.
48. Krebs, F.C., *Fabrication and processing of polymer solar cells: A review of printing and coating techniques*. Solar Energy Materials and Solar Cells, 2009. **93**(4): p. 394-412.
49. Hoppe, H. and N.S. Sariciftci, *Organic solar cells: An overview*. Journal of Materials Research, 2011. **19**(7): p. 1924-1945.
50. Spanggaard, H. and F.C. Krebs, *A brief history of the development of organic and polymeric photovoltaics*. Solar Energy Materials and Solar Cells, 2004. **83**(2): p. 125-146.
51. Skandalos, N. and D. Karamanis, *PV glazing technologies*. Renewable and Sustainable Energy Reviews, 2015. **49**: p. 306-322.
52. Chang, H., et al., *Photoelectrode thin film of dye-sensitized solar cell fabricated by anodizing method and spin coating and electrochemical impedance properties of DSSC*. Applied Surface Science, 2013. **275**: p. 252-257.
53. Zheng, D., P. Zhao, and L. Zhu, *Non-conjugated and π -conjugated functional ligands on semiconductive quantum dots*. Composites Communications, 2018.
54. Leite Didoné, E. and A. Wagner, *Semi-transparent PV windows: A study for office buildings in Brazil*. Energy and Buildings, 2013. **67**: p. 136-142.
55. Kessler, J., et al., *Highly efficient Cu(In,Ga)Se₂ mini-modules*. Solar Energy Materials and Solar Cells, 2003. **75**(1-2): p. 35-46.
56. Ullal, H.S., K. Zwelbel, and B.V. Roedern. *Current status of polycrystalline thin-film PV technologies*. in *Photovoltaic Specialists Conference, 1997., Conference Record of the Twenty-Sixth IEEE*. 1997.
57. Khairnar, U.P., et al., *Optical properties of thermally evaporated cadmium telluride thin films*. Materials Chemistry and Physics, 2003. **80**(2): p. 421-427.
58. Kroon, J.M., et al., *Nanocrystalline dye-sensitized solar cells having maximum performance*. Progress in Photovoltaics: Research and Applications, 2007. **15**(1): p. 1-18.
59. Späth, M., et al., *Reproducible manufacturing of dye-sensitized solar cells on a semi-automated baseline*. Progress in Photovoltaics: Research and Applications, 2003. **11**(3): p. 207-220.

60. Kang, M.G., et al., *Manufacturing method for transparent electric windows using dye-sensitized TiO₂ solar cells*. *Solar Energy Materials and Solar Cells*, 2003. **75**(3–4): p. 475-479.
61. P.W. Wong, Y.S., M. Nonaka, M. Inoue, M. Mizuno, *Field study and modeling of semi-transparent PV in power, thermal and optical aspects*. *Journal of Asian Architecture and Building Engineering*. **4**: p. 549-556.
62. Hee, W.J., et al., *The role of window glazing on daylighting and energy saving in buildings*. *Renewable and Sustainable Energy Reviews*, 2015. **42**: p. 323-343.
63. Chen, F., et al., *Solar heat gain coefficient measurement of semi-transparent photovoltaic modules with indoor calorimetric hot box and solar simulator*. *Energy and Buildings*, 2012. **53**: p. 74-84.
64. Lee, J.W., J. Park, and H.-J. Jung, *A feasibility study on a building's window system based on dye-sensitized solar cells*. *Energy and Buildings*, 2014. **81**: p. 38-47.
65. Chae, Y.T., et al., *Building energy performance evaluation of building integrated photovoltaic (BIPV) window with semi-transparent solar cells*. *Applied Energy*, 2014. **129**: p. 217-227.
66. Wong, P.W., et al., *Semi-transparent PV: Thermal performance, power generation, daylight modelling and energy saving potential in a residential application*. *Renewable Energy*, 2008. **33**(5): p. 1024-1036.
67. Ng, P.K., N. Mithraratne, and H.W. Kua, *Energy analysis of semi-transparent BIPV in Singapore buildings*. *Energy and Buildings*, 2013. **66**: p. 274-281.
68. Freitas, S., et al., *Modelling solar potential in the urban environment: State-of-the-art review*. *Renewable and Sustainable Energy Reviews*, 2015. **41**: p. 915-931.
69. Hofierka, J. and M. Zlocha, *A New 3-D Solar Radiation Model for 3-D City Models*. *Transactions in GIS*, 2012. **16**(5): p. 681-690.
70. Angelis-Dimakis, A., et al., *Methods and tools to evaluate the availability of renewable energy sources*. *Renewable and Sustainable Energy Reviews*, 2011. **15**(2): p. 1182-1200.
71. Liu, B.Y.H. and R.C. Jordan, *The interrelationship and characteristic distribution of direct, diffuse and total solar radiation*. *Solar Energy*, 1960. **4**(3): p. 1-19.
72. Hay, J.E., *Calculation of monthly mean solar radiation for horizontal and inclined surfaces*. *Solar Energy*, 1979. **23**(4): p. 301-307.
73. Ivanova, S.M., *Estimation of background diffuse irradiance on orthogonal surfaces under partially obstructed anisotropic sky. Part I – Vertical surfaces*. *Solar Energy*, 2013. **95**: p. 376-391.
74. Magarreiro, C., M.C. Brito, and P.M.M. Soares, *Assessment of diffuse radiation models for cloudy atmospheric conditions in the Azores region*. *Solar Energy*, 2014. **108**: p. 538-547.
75. López, C.S.P. and M. Sangiorgi, *Comparison Assessment of BIPV Façade Semi-transparent Modules: Further Insights on Human Comfort Conditions*. *Energy Procedia*, 2014. **48**: p. 1419-1428.
76. Xu, S., et al., *Optimal PV cell coverage ratio for semi-transparent photovoltaics on office building façades in central China*. *Energy and Buildings*, 2014. **77**: p. 130-138.
77. Lu, L. and K.M. Law, *Overall energy performance of semi-transparent single-glazed photovoltaic (PV) window for a typical office in Hong Kong*. *Renewable Energy*, 2013. **49**: p. 250-254.

78. Song, J.-H., et al., *Power output analysis of transparent thin-film module in building integrated photovoltaic system (BIPV)*. Energy and Buildings, 2008. **40**(11): p. 2067-2075.
79. Kapsis, K. and A.K. Athienitis, *A study of the potential benefits of semi-transparent photovoltaics in commercial buildings*. Solar Energy, 2015. **115**: p. 120-132.
80. Yoon, S., et al., *Application of transparent dye-sensitized solar cells to building integrated photovoltaic systems*. Building and Environment, 2011. **46**(10): p. 1899-1904.
81. Li, D.H.W., T.N.T. Lam, and K.L. Cheung, *Energy and cost studies of semi-transparent photovoltaic skylight*. Energy Conversion and Management, 2009. **50**(8): p. 1981-1990.
82. Olivieri, L., et al., *Energy saving potential of semi-transparent photovoltaic elements for building integration*. Energy, 2014. **76**: p. 572-583.
83. Stamatakis, A., M. Mandalaki, and T. Tsoutsos, *Multi-criteria analysis for PV integrated in shading devices for Mediterranean region*. Energy and Buildings, 2016. **117**: p. 128-137.
84. Park, K.E., et al., *Analysis of thermal and electrical performance of semi-transparent photovoltaic (PV) module*. Energy, 2010. **35**(6): p. 2681-2687.
85. Li, D.H.W., et al., *Energy and cost analysis of semi-transparent photovoltaic in office buildings*. Applied Energy, 2009. **86**(5): p. 722-729.
86. Yoon, J.-H., J. Song, and S.-J. Lee, *Practical application of building integrated photovoltaic (BIPV) system using transparent amorphous silicon thin-film PV module*. Solar Energy, 2011. **85**(5): p. 723-733.
87. Delisle, V. and M. Kummert, *A novel approach to compare building-integrated photovoltaics/thermal air collectors to side-by-side PV modules and solar thermal collectors*. Solar Energy, 2014. **100**: p. 50-65.
88. Petter Jelle, B., C. Breivik, and H. Drolsum Røkenes, *Building integrated photovoltaic products: A state-of-the-art review and future research opportunities*. Solar Energy Materials and Solar Cells, 2012. **100**: p. 69-96.
89. Peng, C., Y. Huang, and Z. Wu, *Building-integrated photovoltaics (BIPV) in architectural design in China*. Energy and Buildings, 2011. **43**(12): p. 3592-3598.
90. Youssef, A.M.A., Z. Zhai, and R.M. Reffat, *Generating proper building envelopes for photovoltaics integration with shape grammar theory*. Energy and Buildings, 2018. **158**: p. 326-341.
91. Jayathissa, P., et al., *Optimising building net energy demand with dynamic BIPV shading*. Applied Energy, 2017. **202**(Supplement C): p. 726-735.
92. Kang, S., T. Hwang, and J.T. Kim, *Theoretical analysis of the blinds integrated photovoltaic modules*. Energy and Buildings, 2012. **46**(Supplement C): p. 86-91.
93. Radut, M. and O. Mihai. *Multifunctional Integrated photovoltaic window with advanced features of energy harvesting and indoor shading control: Hardware implementation*. in *Electronics, Computers and Artificial Intelligence (ECAI), 2015 7th International Conference on*. 2015.
94. Kang, S., T. Hwang, and J.T. Kim, *Theoretical analysis of the blinds integrated photovoltaic modules*. Energy and Buildings, 2012. **46**: p. 86-91.
95. Kim, J.-J., et al., *Optimization of Photovoltaic Integrated Shading Devices*. Indoor and Built Environment, 2010. **19**(1): p. 114-122.

96. Sun, L.L. and H.X. Yang, *Impacts of the shading-type building-integrated photovoltaic claddings on electricity generation and cooling load component through shaded windows*. Energy and Buildings, 2010. **42**(4): p. 455-460.
97. Yoo, S.-H. and E.-T. Lee, *Efficiency characteristic of building integrated photovoltaics as a shading device*. Building and Environment, 2002. **37**(6): p. 615-623.
98. Michael, J.J., I. S, and R. Goic, *Flat plate solar photovoltaic–thermal (PV/T) systems: A reference guide*. Renewable and Sustainable Energy Reviews, 2015. **51**: p. 62-88.
99. Sahota, L. and G.N. Tiwari, *Review on series connected photovoltaic thermal (PVT) systems: Analytical and experimental studies*. Solar Energy, 2017. **150**: p. 96-127.
100. da Silva, R.M. and J.L.M. Fernandes, *Hybrid photovoltaic/thermal (PV/T) solar systems simulation with Simulink/Matlab*. Solar Energy, 2010. **84**(12): p. 1985-1996.
101. Buker, M.S. and S.B. Riffat, *Building integrated solar thermal collectors – A review*. Renewable and Sustainable Energy Reviews, 2015. **51**: p. 327-346.
102. Lämmle, M., et al., *PVT collector technologies in solar thermal systems: A systematic assessment of electrical and thermal yields with the novel characteristic temperature approach*. Solar Energy, 2017. **155**: p. 867-879.
103. Tyagi, V.V., S.C. Kaushik, and S.K. Tyagi, *Advancement in solar photovoltaic/thermal (PV/T) hybrid collector technology*. Renewable and Sustainable Energy Reviews, 2012. **16**(3): p. 1383-1398.
104. Kalogirou, S.A., *Solar thermal collectors and applications*. Progress in Energy and Combustion Science, 2004. **30**(3): p. 231-295.
105. Cabrera, F.J., et al., *Use of parabolic trough solar collectors for solar refrigeration and air-conditioning applications*. Renewable and Sustainable Energy Reviews, 2013. **20**: p. 103-118.
106. Hansen, J., et al., *Market, modelling, testing and demonstration in the framework of IEA SHC Task 35 on PV/thermal solar systems*. 2018.
107. Wu, J., et al., *A review of thermal absorbers and their integration methods for the combined solar photovoltaic/thermal (PV/T) modules*. Renewable and Sustainable Energy Reviews.
108. Chow, T.T., *A review on photovoltaic/thermal hybrid solar technology*. Applied Energy, 2010. **87**(2): p. 365-379.
109. Davidsson, H., B. Perers, and B. Karlsson, *Performance of a multifunctional PV/T hybrid solar window*. Solar Energy, 2010. **84**(3): p. 365-372.
110. Davidsson, H., B. Perers, and B. Karlsson, *System analysis of a multifunctional PV/T hybrid solar window*. Solar Energy, 2012. **86**(3): p. 903-910.
111. Ulavi, T., T. Hebrink, and J.H. Davidson, *Analysis of a hybrid solar window for building integration*. Solar Energy, 2014. **105**: p. 290-302.
112. Sabry, M., et al., *Smart windows: Thermal modelling and evaluation*. Solar Energy, 2014. **103**: p. 200-209.
113. Lamnatou, C. and D. Chemisana, *Concentrating solar systems: Life Cycle Assessment (LCA) and environmental issues*. Renewable and Sustainable Energy Reviews, 2017. **78**: p. 916-932.
114. Algora, C. and I. Rey-Stolle, *Handbook of Concentrator Photovoltaic Technology*. 2016. 1-772.

115. Shanks, K., S. Senthilarasu, and T.K. Mallick, *Optics for concentrating photovoltaics: Trends, limits and opportunities for materials and design*. Renewable and Sustainable Energy Reviews, 2016. **60**: p. 394-407.
116. Horne, S., *10 - Concentrating photovoltaic (CPV) systems and applications*, in *Concentrating Solar Power Technology*. 2012, Woodhead Publishing. p. 323-361.
117. Sarmah, N., B.S. Richards, and T.K. Mallick, *Evaluation and optimization of the optical performance of low-concentrating dielectric compound parabolic concentrator using ray-tracing methods*. Applied Optics, 2011. **50**(19): p. 3303-3310.
118. Baig, H., et al., *Performance analysis of a dielectric based 3D building integrated concentrating photovoltaic system*. Solar Energy, 2014. **103**: p. 525-540.
119. Li, X., et al., *Comparative study on two novel intermediate temperature CPC solar collectors with the U-shape evacuated tubular absorber*. Solar Energy, 2013. **93**: p. 220-234.
120. Dreger, M., et al., *Development and investigation of a CPV module with Cassegrain mirror optics*. AIP Conference Proceedings, 2014. **1616**(1): p. 177-182.
121. Sharma, S., et al., *Performance enhancement of a Building-Integrated Concentrating Photovoltaic system using phase change material*. Solar Energy Materials and Solar Cells, 2016. **149**: p. 29-39.
122. Sellami, N., T.K. Mallick, and D.A. McNeil, *Optical characterisation of 3-D static solar concentrator*. Energy Conversion and Management, 2012. **64**: p. 579-586.
123. Tang, R. and X. Liu, *Optical performance and design optimization of V-trough concentrators for photovoltaic applications*. Solar Energy, 2011. **85**(9): p. 2154-2166.
124. Sellami, N. and T.K. Mallick, *Optical characterisation and optimisation of a static Window Integrated Concentrating Photovoltaic system*. Solar Energy, 2013. **91**: p. 273-282.
125. Singh, H., M. Sabry, and D.A.G. Redpath, *Experimental investigations into low concentrating line axis solar concentrators for CPV applications*. Solar Energy, 2016. **136**: p. 421-427.
126. Perez-Higueras, P. and E. Fernández, *High Concentrator Photovoltaics: Fundamentals, Engineering and Power Plants*. 2015.
127. Abu-Bakar, S.H., et al., *Performance analysis of a novel rotationally asymmetrical compound parabolic concentrator*. Applied Energy, 2015. **154**: p. 221-231.
128. Sarmah, N. and T.K. Mallick, *Design, fabrication and outdoor performance analysis of a low concentrating photovoltaic system*. Solar Energy, 2015. **112**: p. 361-372.
129. Bunthof, L.A.A., et al., *Impact of shading on a flat CPV system for façade integration*. Solar Energy, 2016. **140**: p. 162-170.
130. Fernández, E.F., et al., *A model based on artificial neuronal network for the prediction of the maximum power of a low concentration photovoltaic module for building integration*. Solar Energy, 2014. **100**: p. 148-158.
131. Baig, H., et al., *Enhancing performance of a linear dielectric based concentrating photovoltaic system using a reflective film along the edge*. Energy, 2014. **73**: p. 177-191.

132. Baig, H., E.F. Fernández, and T.K. Mallick, *Influence of spectrum and latitude on the annual optical performance of a dielectric based BICPV system*. Solar Energy, 2016. **124**: p. 268-277.
133. Abu-Bakar, S.H., et al., *Performance analysis of a solar window incorporating a novel rotationally asymmetrical concentrator*. Energy, 2016. **99**: p. 181-192.
134. Ramirez-Iniguez, R., et al., *Experimental evaluation of a solar window incorporating rotationally asymmetrical compound parabolic concentrators (RACPC)*. Energy Procedia, 2017. **130**: p. 102-107.
135. Mallick, T.K. and P.C. Eames, *Design and fabrication of low concentrating second generation PRIDE concentrator*. Solar Energy Materials and Solar Cells, 2007. **91**(7): p. 597-608.
136. Goetzberger, A. and W. Greube, *Solar energy conversion with fluorescent collectors*. Applied physics, 1977. **14**(2): p. 123-139.
137. Weber, W.H. and J. Lambe, *Luminescent greenhouse collector for solar radiation*. Applied Optics, 1976. **15**(10): p. 2299-2300.
138. van Sark, W.G.J.H.M., *Luminescent solar concentrators – A low cost photovoltaics alternative*. Renewable Energy, 2013. **49**: p. 207-210.
139. Chemisana, D., *Building Integrated Concentrating Photovoltaics: A review*. Renewable and Sustainable Energy Reviews, 2011. **15**(1): p. 603-611.
140. Goldschmidt, J.C., *1.27 - Luminescent Solar Concentrator A2 - Sayigh, Ali, in Comprehensive Renewable Energy*. 2012, Elsevier: Oxford. p. 587-601.
141. 2015, C.L.a.B.L., Journal of optics. **17** (025901).
142. Aste, N., et al., *Visual Performance of Yellow, Orange and Red LSCs Integrated in a Smart Window*. Energy Procedia, 2017. **105**(Supplement C): p. 967-972.
143. Reisfeld, R., *New developments in luminescence for solar energy utilization*. Optical Materials, 2010. **32**(9): p. 850-856.
144. Currie, M.J., et al., *High-Efficiency Organic Solar Concentrators for Photovoltaics*. Science, 2008. **321**(5886): p. 226-228.
145. Sark, W.G.J.H.M.v., et al., *Luminescent Solar Concentrators - A review of recent results*. Optics Express, 2008. **16**(26): p. 21773-21792.
146. Slooff, L., et al., *The luminescent concentrator illuminated*. Vol. 6197. 2006.
147. basf, <http://www.basf.de>.
148. Barnham, K., et al., *Quantum-dot concentrator and thermodynamic model for the global redshift*. Applied Physics Letters, 2000. **76**(9): p. 1197-1199.
149. Norton, B., et al., *Enhancing the performance of building integrated photovoltaics*. Solar Energy, 2011. **85**(8): p. 1629-1664.
150. Bera, D., L. Qian, and P.H. Holloway, *19 Semiconducting Quantum Dots for Bioimaging*. Drug Delivery Nanoparticles Formulation and Characterization, 2009. **191**: p. 349.
151. Dayneko, S., et al., *Application of CdSe/ZnS/CdS/ZnS Core-multishell Quantum Dots to Modern OLED Technology*. Materials Today: Proceedings, 2016. **3**(2): p. 211-215.
152. Dovzhenko, D., et al., *Porous Silicon Microcavity Modulates the Photoluminescence Spectra of Organic Polymers and Quantum Dots*. Materials Today: Proceedings, 2016. **3**(2): p. 485-490.
153. Linkov, P., et al., *High Quantum Yield CdSe/ZnS/CdS/ZnS Multishell Quantum Dots for Biosensing and Optoelectronic Applications*. Materials Today: Proceedings, 2016. **3**(2): p. 104-108.

154. Finetti, C., L. Plavisch, and M. Chiari, *Use of quantum dots as mass and fluorescence labels in microarray biosensing*. *Talanta*, 2016. **147**: p. 397-401.
155. Stanisavljevic, M., et al., *Quantum dots-fluorescence resonance energy transfer-based nanosensors and their application*. *Biosensors and Bioelectronics*, 2015. **74**: p. 562-574.
156. Sukhanova, A., et al., *Multiphoton Imaging of Tumor Biomarkers in situ Using Single-domain Antibodies Conjugated with Quantum Dots in a Set Orientation*. *Materials Today: Proceedings*, 2016. **3**(2): p. 523-526.
157. Tabish, T.A. and S. Zhang, *Graphene Quantum Dots: Syntheses, Properties and Biological Applications*, in *Reference Module in Materials Science and Materials Engineering*. 2016, Elsevier.
158. Tavakoli, M.M., *Surface Engineering of Pbs Colloidal Quantum Dots Using Atomic Passivation for Photovoltaic Applications*. *Procedia Engineering*, 2016. **139**: p. 117-122.
159. Volkov, Y., *Quantum dots in nanomedicine: recent trends, advances and unresolved issues*. *Biochemical and Biophysical Research Communications*, 2015. **468**(3): p. 419-427.
160. Jin, Z., et al., *Graphene, graphene quantum dots and their applications in optoelectronics*. *Current Opinion in Colloid & Interface Science*, 2015. **20**(5–6): p. 439-453.
161. Bonilla, J.C., et al., *Applications of quantum dots in Food Science and biology*. *Trends in Food Science & Technology*, 2016. **53**: p. 75-89.
162. Shen, L.-M. and J. Liu, *New development in carbon quantum dots technical applications*. *Talanta*, 2016. **156–157**: p. 245-256.
163. Bak, S., D. Kim, and H. Lee, *Graphene quantum dots and their possible energy applications: A review*. *Current Applied Physics*.
164. Shakir, I., et al., *Advances in Functional Materials (Conference 2015) Application of CdSe/ZnS/CdS/ZnS Core–multishell Quantum Dots to Modern OLED Technology*. *Materials Today: Proceedings*, 2016. **3**(2): p. 211-215.
165. Kamat, P.V., *Quantum Dot Solar Cells. The Next Big Thing in Photovoltaics*. *The Journal of Physical Chemistry Letters*, 2013. **4**(6): p. 908-918.
166. Bera, D., et al., *Quantum dots and their multimodal applications: a review*. *Materials*, 2010. **3**(4): p. 2260-2345.
167. Goldschmidt, J.C., et al., *Increasing the efficiency of fluorescent concentrator systems*. *Solar Energy Materials and Solar Cells*, 2009. **93**(2): p. 176-182.
168. Slooff, L.H., et al., *A luminescent solar concentrator with 7.1% power conversion efficiency*. *physica status solidi (RRL) – Rapid Research Letters*, 2008. **2**(6): p. 257-259.
169. Bomm, J., et al., *Fabrication and full characterization of state-of-the-art quantum dot luminescent solar concentrators*. *Solar Energy Materials and Solar Cells*, 2011. **95**(8): p. 2087-2094.
170. Gallagher, S.J., B. Norton, and P.C. Eames, *Quantum dot solar concentrators: Electrical conversion efficiencies and comparative concentrating factors of fabricated devices*. *Solar Energy*, 2007. **81**(6): p. 813-821.
171. Kerrouche, A., et al., *Luminescent solar concentrators: From experimental validation of 3D ray-tracing simulations to coloured stained-glass windows for BIPV*. *Solar Energy Materials and Solar Cells*, 2014. **122**: p. 99-106.

172. Fathi, M., M. Abderrezek, and F. Djahli, *Experimentations on luminescent glazing for solar electricity generation in buildings*. *Optik - International Journal for Light and Electron Optics*, 2017. **148**(Supplement C): p. 14-27.
173. Baetens, R., B.P. Jelle, and A. Gustavsen, *Properties, requirements and possibilities of smart windows for dynamic daylight and solar energy control in buildings: A state-of-the-art review*. *Solar Energy Materials and Solar Cells*, 2010. **94**(2): p. 87-105.
174. Di Carlo, G., et al., *β -Substituted ZnII porphyrins as dyes for DSSC: A possible approach to photovoltaic windows*. *Coordination Chemistry Reviews*, 2018. **358**: p. 153-177.
175. Seeboth, A., J. Schneider, and A.A. Patzak, *Materials for intelligent sun protecting glazing - Properties and Applications*. *Solar Energy Materials and Solar Cells*, 2000. **60**.
176. Schneider, J. and A. Seeboth, *Natural Thermotropic Materials For Solar Switching Glazing*. *Materialwissenschaft und Werkstofftechnik*, 2001. **32**: p. 231-237.
177. Thiel, J., G. Maurer, and J. Prausnitz, *Hydrogele: Verwendungsmöglichkeiten und thermodynamische Eigenschaften*. *Chemie Ingenieur Technik - CHEM-ING-TECH*, 1995. **67**: p. 1567-1583.
178. Flood, P., H. Page, and E.G. Reynaud, *Using hydrogels in microscopy: A tutorial*. *Micron*, 2016. **84**: p. 7-16.
179. Schroeder, U. and W. Oppermann, *Mechanical and stress-optical properties of strongly swollen hydrogels*. *Makromolekulare Chemie. Macromolecular Symposia*, 1993. **76**: p. 63-74.
180. Peppas, N., *Hydrogels: Specialty Plastics for Biomedical and Pharmaceutical Application*. Technomic Pub Co, 1990.
181. Schröder, U. and W. Oppermann. *Mechanical and stress-optical properties of strongly swollen hydrogels*. in *Makromolekulare Chemie. Macromolecular Symposia*. 1993. Wiley Online Library.
182. Jain, S., et al., *Cellulose derivatives as thermoresponsive polymer: an overview*. *Journal of Applied Pharmaceutical Science*, 2013. **3**(12): p. 139-144.
183. Calejo, M.T., et al. *Interactions between ethyl(hydroxyethyl) cellulose and lysine-based surfactants in aqueous media*. 2012.
184. Carlsson, A., G. Karlström, and B. Lindman. *Thermal gelation of nonionic cellulose ethers and ionic surfactants in water*. 1990.
185. Goldszal, A., S. Costeux, and M. Djabourov. *Phase separation of aqueous solutions of cellulose derivatives: influence of surfactants*. 1996.
186. Dürig, T. and K. Karan, *Chapter 9 - Binders in Wet Granulation*, in *Handbook of Pharmaceutical Wet Granulation*, A.S. Narang and S.I.F. Badawy, Editors. 2019, Academic Press. p. 317-349.
187. Schneider, J. and A. Seeboth, *Natural Thermotropic Materials For Solar Switching Glazing*. *Materialwissenschaft und Werkstofftechnik*, 2001. **32**(3): p. 231-237.
188. Jain, S., et al., *Cellulose derivatives as thermoresponsive polymer: An overview*. *Journal of Applied Pharmaceutical Science*, 2013. **3**: p. 139-144.
189. Deshmukh, K., et al., *3 - Biopolymer Composites With High Dielectric Performance: Interface Engineering*, in *Biopolymer Composites in Electronics*, K.K. Sadasivuni, et al., Editors. 2017, Elsevier. p. 27-128.
190. Lim, W.-S., et al., *Thermal characteristics of Hydroxypropyl Methyl Cellulose*. *Journal of Loss Prevention in the Process Industries*, 2009. **22**(2): p. 182-186.

191. Sarkar, N., *Thermal gelation properties of methyl and hydroxypropyl methylcellulose*. Journal of Applied Polymer Science, 1979. **24**(4): p. 1073-1087.
192. Lima, L.H., Y. Morales, and T. Cabral, *Poly-N-isopropylacrylamide (pNIPAM): a reversible bioadhesive for sclerotomy closure*. International journal of retina and vitreous, 2016. **2**: p. 23-23.
193. Topp, M.D.C., et al., *Thermosensitive Micelle-Forming Block Copolymers of Poly(ethylene glycol) and Poly(N-isopropylacrylamide)*. Macromolecules, 1997. **30**(26): p. 8518-8520.
194. Cao, M., et al., *Reversible Thermo-responsive Peptide–PNIPAM Hydrogels for Controlled Drug Delivery*. Biomacromolecules, 2019. **20**(9): p. 3601-3610.
195. Watanabe, H., *Intelligent window using a hydrogel layer for energy efficiency*. Solar Energy Materials and Solar Cells, 1998. **54**(1–4): p. 203-211.
196. Szilágyi, A., et al., *Thermotropic Polymer Gels: Smart Gel Glass*. Macromolecular Symposia, 2005. **227**(1): p. 357-366.
197. Zhou, Y., et al., *Temperature-responsive hydrogel with ultra-large solar modulation and high luminous transmission for "smart window" applications*. Journal of Materials Chemistry A, 2014. **2**(33): p. 13550-13555.
198. Wang, M., et al., *Binary Solvent Colloids of Thermosensitive Poly(N-isopropylacrylamide) Microgel for Smart Windows*. Industrial & Engineering Chemistry Research, 2014. **53**(48): p. 18462-18472.
199. Gyenes, T., et al., *Electrically adjustable thermotropic windows based on polymer gels*. Polymers for Advanced Technologies, 2003. **14**(11-12): p. 757-762.
200. Wu, Y., et al., *Smart solar concentrators for building integrated photovoltaic façades*. Solar Energy, 2016. **133**: p. 111-118.
201. Connelly, K., et al., *Design and development of a reflective membrane for a novel Building Integrated Concentrating Photovoltaic (BICPV) 'Smart Window' system*. Applied Energy, 2016. **182**: p. 331-339.
202. Allen, K., et al., *Smart windows—Dynamic control of building energy performance*. Energy and Buildings, 2017. **139**: p. 535-546.
203. Debije, M.G., *Solar Energy Collectors with Tunable Transmission*. Advanced Functional Materials, 2010. **20**(9): p. 1498-1502.
204. Wang, K., et al., *Integrated energy storage and electrochromic function in one flexible device: an energy storage smart window*. Energy & Environmental Science, 2012. **5**(8): p. 8384-8389.
205. Malara, F., et al., *Smart Windows for Building Integration: A New Architecture for Photovoltachromic Devices*. ACS Applied Materials & Interfaces, 2014. **6**(12): p. 9290-9297.
206. Kwon, H.-K., et al., *Optically Switchable Smart Windows with Integrated Photovoltaic Devices*. Advanced Energy Materials, 2015. **5**(3): p. 1401347-n/a.
207. Huang, L.-M., et al., *Photovoltaic electrochromic device for solar cell module and self-powered smart glass applications*. Solar Energy Materials and Solar Cells, 2012. **99**: p. 154-159.
208. Zhou, J., et al., *VO₂ thermochromic smart window for energy savings and generation*. Scientific Reports, 2013. **3**: p. 3029.
209. Guo, F., et al., *Printed Smart Photovoltaic Window Integrated with an Energy-Saving Thermochromic Layer*. Advanced Optical Materials, 2015. **3**(11): p. 1524-1529.

210. Martina, F., et al., *Large area self-powered semitransparent trifunctional device combining photovoltaic energy production, lighting and dynamic shading control*. Solar Energy Materials and Solar Cells, 2017. **160**: p. 435-443.
211. L. Ford, J., *Design and Evaluation of Hydroxypropyl Methylcellulose Matrix Tablets for Oral Controlled Release: A Historical Perspective*. Vol. 16. 2014. 17-51.
212. Ford, J.L., *Design and Evaluation of Hydroxypropyl Methylcellulose Matrix Tablets for Oral Controlled Release: A Historical Perspective*, in *Hydrophilic Matrix Tablets for Oral Controlled Release*, P. Timmins, S.R. Pygall, and C.D. Melia, Editors. 2014, Springer New York: New York, NY. p. 17-51.
213. Dimitrov, I., et al., *Thermosensitive water-soluble copolymers with doubly responsive reversibly interacting entities*. Progress in Polymer Science, 2007. **32**(11): p. 1275-1343.
214. Xia, X., et al., *Formation and Volume Phase Transition of Hydroxypropyl Cellulose Microgels in Salt Solution*. Macromolecules, 2003. **36**(10): p. 3695-3698.
215. Khuman, P., et al., *Viscosity-Temperature Behavior of Hydroxypropyl Cellulose Solution in Presence of an Electrolyte or a Surfactant: A Convenient Method to Determine the Cloud Point of Polymer Solutions*. Journal of Macromolecular Science, Part A, 2014. **51**(11): p. 924-930.
216. Feller, R.L.W., *Evaluation of cellulose ethers for conservation*. 1990.
217. Karlberg, M., K. Thuresson, and B. Lindman, *Hydrophobically modified ethyl(hydroxyethyl)cellulose as stabilizer and emulsifying agent in macroemulsions*. Colloids and Surfaces A: Physicochemical and Engineering Aspects, 2005. **262**(1): p. 158-167.
218. Nations, F.a.A.O.o.t.U., *Compendium of Food Additive Specifications. Addendum 5. (FAO Food and Nutrition Paper. 1997*(Joint FAO/WHO Expert Committee on Food Additives
- 49th session).
219. Höhne, G., W.F. Hemminger, and H.-J. Flammersheim, *Differential scanning calorimetry*. 2013: Springer Science & Business Media.
220. Haynie, D.T., *Biological thermodynamics*. 2001: Cambridge University Press.
221. Chiu, M.H. and E.J. Prenner, *Differential scanning calorimetry: An invaluable tool for a detailed thermodynamic characterization of macromolecules and their interactions*. Journal of pharmacy & bioallied sciences, 2011. **3**(1): p. 39-59.
222. Demetzos, C., *Differential Scanning Calorimetry (DSC): A Tool to Study the Thermal Behavior of Lipid Bilayers and Liposomal Stability*. Journal of Liposome Research, 2008. **18**(3): p. 159-173.
223. McElhaney, R.N., *The use of differential scanning calorimetry and differential thermal analysis in studies of model and biological membranes*. Chemistry and Physics of Lipids, 1982. **30**(2): p. 229-259.
224. *Interpretation of Infrared Spectra, A Practical Approach*, in *Encyclopedia of Analytical Chemistry*.
225. Titus, D., E. James Jebaseelan Samuel, and S.M. Roopan, *Chapter 12 - Nanoparticle characterization techniques*, in *Green Synthesis, Characterization and Applications of Nanoparticles*, A.K. Shukla and S. Iravani, Editors. 2019, Elsevier. p. 303-319.
226. EN, N., *410, Glass in building, Determination of luminous and solar characteristics of glazing*. 2011. AFNOR.

227. Eager, S., et al., *Environmentally friendly processes in the manufacture of Saturn solar cells*. 2002. 62-65.
228. Teijido, J., *Conception and design of illumination light pipes*. 2000.
229. Liu, X., et al., *Investigation of the Optical Performance of a Novel Planar Static PV Concentrator with Lambertian Rear Reflectors*. Vol. 7. 2017. 88.
230. Gibson, J.H., *UVB Radiation: Definition and Characteristics*. In *UV-B Monitoring and Research Program*. 2000.